Centro de Investigación y de Estudios Avanzados
del Instituto Politécnico Nacional

Cinvestav

Unidad Zacatenco

Programa de Nanociencias y Nanotecnología

Pureza de Fase y Calidad Cristalina de Epicapas de GaN Zincblenda

TESIS

Que presenta

Raúl Trejo Hernández

Para obtener el grado de

Doctor en Ciencias

En Nanociencias y Nanotecnología

Directores de la tesis: Dr. Máximo López López
Dra. Yenny Lucero Casallas Moreno

Ciudad de México Noviembre, 2023

Cinvestav

Center for Research and Advanced Studies
of the National Polytechnic Institute

Zacatenco Unit

Nanoscience and Nanotechnology Program

Phase Purity and Crystalline Quality of Zincblende GaN Epilayers

THESIS

Presented by

Raúl Trejo Hernández

To obtain the degree of

Doctor of Science

In Nanoscience and Nanotechnology

Thesis supervisors: Dr. Máximo López López
Dr. Yenny Lucero Casallas Moreno

Mexico City November, 2023

A mi querida madre, por su amor y apoyo incondicional durante todos estos años, por creer siempre en mí y por darme la fuerza para seguir adelante.

A la memoria de mi padre, quien me inspiró con su sabiduría y me enseñó el valor del trabajo duro y la perseverancia.

Acknowledgments

First and foremost, I wish to express my deepest gratitude to Dr. Máximo López López for accepting me into his research group, providing this fascinating thesis topic, and the means to undertake my doctoral studies. His guidance and support were most definitely invaluable. I am also immensely grateful to Dr. Yenny Lucero Casallas Moreno for co-supervising this work. Her insightful discussions, attention to detail, dedication, and constant motivational talks pushed me forward throughout these tough times.

Moreover, I would like to thank Dr. Daniel Bahena Uribe, Dr. Iouri Koudriavtsev, Dr. Julio Gregorio Mendoza Álvarez, and Dr. Jorge Adalberto Huerta Ruelas for agreeing to be part of my evaluation committee with all the responsibilities and time that this commitment requires. I would also like to thank Dr. Mario Alberto Zambrano Serrano, Dr. Marlene Camacho Reynoso, Dr. Briseida Guadalupe Pérez Hernández, and Dr. Marcos Macias Mier for participating in some of the growth experiments presented in this work.

I could not be more grateful to Dr. Salvador Gallardo Hernández for allowing me to use and training me on the X-ray diffractometer, which enabled most of the measurements presented in this work. Without his generosity in providing access and training on this instrument, this work could not have been finished in the allotted time. Not to mention his availability for helping fix what broke when it inevitably happened a couple of times in the XRD and MBE labs.

I would also like to appreciate the hard-working people helping me with other characterization techniques presented in this work: Dr. Ángel Guillén Cervantes for the SEM and EDX measurements, María Georgina Ramírez Cruz and Dr. Rogelio Jaime Fragoso Soriano for the AFM experiments, Eleazar Urbina Álvarez and Liliana Naranjo Naranjo for the EBSD, Dr. Iouri Koudriavtsev for the SIMS measurements, and Miguel Galván Arellano for Hall effect.

My past and present colleagues Ángel Leonardo Martínez López, Horacio Solís Cisneros, Rubén Martínez Revuelta, Jorge Iván Hernández Martínez, and Jesús Fernando Fabián Jocobi could not go without mention. Their support was definitely invaluable throughout these past years.

Finally, I thank CINVESTAV for providing the infrastructure to carry out this work, as well as the National Council of Humanities Science and Technology (CONAHCYT) in Mexico for the postgraduate scholarship that allowed me to sustain myself during the last four years.

Resumen

A través de un estudio detallado de figuras de polos obtenidas mediante difracción de rayos X y de electrones, este trabajo describe la pureza de fase y la calidad cristalina de epicapas de GaN en fase zincblenda (zb) crecidas por epitaxia de haces moleculares asistida por plasma usando diferentes condiciones. Se estudiaron los efectos de las primeras etapas del proceso epitaxial variando la temperatura de crecimiento de capas de nucleación de GaN-zb de 5 nm de espesor. El análisis aquí presentado reveló que una temperatura de nucleación de 665 °C resultó en crecimiento homoepitaxial posterior con hasta un 99.6 % de contenido de zincblenda—de lo cual un 99.7 % fue material sin maclar—, así como una excelente calidad cristalina y superficial. Adicionalmente a estas propiedades buscadas, también se logró un alto grado de orientación siguiendo la de los sustratos de GaAs. Temperaturas mayores causaron cantidades de defectos más altas, probablemente debido a la movilidad aumentada de los adátomos durante la nucleación, llevando a la formación de islas más grandes con densidad menor donde los defectos no alcanzaron las orillas para ser aniquilados.

Además, se estudiaron epicapas de GaN-zb dopadas con Mg crecidas bajo condiciones ricas en Ga y en N. El crecimiento rico en Ga permitió hasta un 99.9 % de zincblenda—con un 99.1 % sin maclar—, una calidad cristalina excelente y superficies lisas. En contraste, las películas ricas en N sufrieron un maclado severo e inclusiones de wurtzita, con solo un 27 % de zincblenda. Esto debido posiblemente a la una capa de mojado debido al exceso de metal en condiciones ricas en Ga, aumentando la movilidad atómica y reduciendo la cantidad de defectos. Mediante espectrometría de masas de iones secundarios y mediciones de efecto Hall, se encontraron entre 2 y 3 órdenes de magnitud más aceptores de Mg eléctricamente activos con condiciones ricas en Ga, resaltando el papel surfactante del exceso de Ga. Especialmente en las muestras ricas en N, el aumento de la temperatura de la celda de Mg resultó en una calidad general degradada de las películas, sugiriendo que los átomos de Mg actúan como centros de defectos.

Finalmente, el desarrollo de un script en Python para la simulación de figuras de polos ayudó en gran medida a llevar a cabo una descripción exhaustiva de la orientación cristalina de las epicapas de GaN zincblenda con respecto a los sustratos, ayudando a identificar señales provenientes de maclas, inclusiones de wurtzita, así como wurtzita crecida sobre maclas. Este trabajo determinó con éxito las condiciones óptimas para crecimiento de epicapas de GaN dopadas y no dopadas de alta calidad en fase zincblenda, allanando el camino para optoelectrónica monolítica de GaN-zb aprovechando la madurez de la tecnología actual de GaAs.

Abstract

Through detailed analyses of pole figures from x-ray and electron diffraction, this work describes the phase purity and crystalline quality of zincblende (zb) GaN epilayers grown by plasma-assisted molecular beam epitaxy using various conditions. The effects of the very first stages of the epitaxial process were studied through varying the growth temperature of 5 nm thick zincblende GaN nucleation layers. The analysis of this work revealed that a nucleation temperature of 665°C resulted in subsequent homoepitaxial growth with up to 99.6 % of zincblende content, from which 99.7 % was untwinned material, as well as excellent crystalline and surface quality. Additionally to these sought-for properties, a high degree of orientation following that of the GaAs substrates was also achieved. Higher temperatures caused more defects likely due to enhanced adatom mobility during nucleation leading to bigger, lower density islands where defects could not glide out to the edges and annihilate.

Moreover, Mg-doped zb-GaN epilayers grown under Ga-rich and N-rich conditions were also studied. Ga-rich growth enabled up to 99.9 % zb purity with 99.1 % untwinning, superb crystalline quality, and smooth surfaces. In contrast, N-rich films suffered severe twinning and wurtzite inclusions, with as low as 27 % zincblende content. This was likely due to the Ga wetting layer formed by the excess metal under Ga-rich conditions, improving adatom mobility and reducing defects. Secondary ion mass spectrometry and Hall effect measurements revealed between 2 to 3 orders of magnitude more electrically active Mg acceptors for Ga-rich films, highlighting the surfactant role of excess Ga. Especially in N-rich samples, upping the Mg cell temperature resulted in degraded overall quality of the films, suggesting that Mg atoms act as defect-generation centers.

Finally, developing a Python script for pole figure simulation greatly aided carrying out a thorough description of crystalline orientation of the zincblende GaN epilayers with respect to the substrates, helping the identification of signals coming from twins, wurtzite inclusions, and the latter growing on the former. This work successfully determined the optimal conditions for high quality doped and undoped GaN epilayers in the zincblende phase, paving the way for monolithic zb-GaN optoelectronics leveraging the maturity of current GaAs technology.

Contents

Part I Introduction

Part II Literature Review

Part III Simulations

Part IV Experimental Section

List of Figures

List of Tables

List of Acronyms

2DEG	two-dimensional electron gas
AFM	atomic force microscopy
E-HEMT	enhancement mode HEMT
EBSD	electron backscatter diffraction
FCC	face-centered cubic
FM	Frank-van der Merwe
FWHM	full-width at half-maximum
GaN	gallium nitride
HEMT	high-electron-mobility transistor
IPF	inverse PF
MBE	molecular beam epitaxy
ODF	orientation density function
PAMBE	plasma-assisted MBE
PF	pole figure
QCSE	quantum confined Stark effect
QW	quantum well
RF	radio-frequency
RHEED	reflection high-energy electron diffraction
RMS	root mean square
SEM	scanning electron microscopy
SK	Stranski-Krastanov
UHV	ultra-high vacuum
VW	Volmer-Weber
XRD	x-ray diffraction

Part I: Introduction

Chapter 1: Introduction

1.1 Motivation

Being at the heart of many optoelectronic devices, semiconductors are one of the most important kind of materials as of today. Among them, an important group of semiconductors that has gained traction the last decades is the III-nitride (also III-N) group of semiconductors. More specifically, this group is comprised by one or more atoms of the group IIIA, or group 13 according to the International Union of Pure and Applied Chemistry [1], as cations and a N atom (group VA or 15) as anion. Gallium nitride (GaN), as a representative of the binaries (with AlN and InN), the ternaries (AlGaN, GaInN, and AlInN), along with the quaternary (AlGaInN) of the III-N group, has found its way into applications such as high-power amplifier [2], detectors [3], and illumination [4, 5], which ultimately led Isamu Akasaki, Hiroshi Amano, and Shuji Nakamura to win the Nobel Prize in Physics in 2014 [6].

GaN is most commonly grown and used along the c direction of the hexagonal wurtzite phase. Along c, however, this phase tends to produce strong polarization fields across heterostructures which are the active core of many optoelectronic devices. Hence, radiative recombination rates are reduced and current-density dependent wavelength emission are produced [7, 8]. Moreover, polarization in hexagonal nitrides produce normally-on transistors [9]. In order to avoid polarization, such as to attain higher efficiency emission or normally-off transistors, complicated structures or growing on semipolar/non-polar directions are some of the means currently used [10–14].

A promising approach to solve these problems altogether is using the cubic zincblende phase of GaN, which, thanks to its symmetry, does not have a meaningful polarization field along the common cubic growth direction [15]. Moreover, the zincblende phase has smaller bandgap [16], thus facilitating shorter wavelength emission with low In contents in $\mathrm{In}_x\mathrm{Ga}_{(1-x)}\mathrm{N}$ alloys. Finally, zincblende GaN has a higher optical gain [17] and is easier to cleave.

Unfortunately, zincblende nitrides are metastable outside a narrow range of growth conditions and tend to suffer from phase transitions toward the more-stable wurtzite phase [18–22]. This results in poor-quality GaN rich in wurtzite inclusions, thereby degrading device performance; hence, it is of extreme importance to understand and prevent this process as much as possible.

This problematic is exacerbated by the fact that there are not native substrates for zincblende nitrides. Therefore, foreign substrate such as MgO [23–25], 3C-SiC [26–28], and GaAs [19, 29–31] are commonly employed in their growth via molecular beam epitaxy (MBE), with their associated problems due to lattice mismatch. From these, 3C SiC has shown the best results due to the negligible lattice mismatch to GaN. However, GaAs may enjoy other advantages, such as lower price and already widespread utilization. Alas, the huge lattice mismatch between GaN and GaAs poses challenges for defect reduction; therefore, it needs more attention in research, which currently focuses mainly on 3C SiC.

Yet another challenge hindering zincblende utilization, and nitrides in general, is *p*-type doping. For many years, achieving *p*-type doping in nitrides was a significant challenge. Managing to do it was actually the reason as to why the Nobel prize mentioned at the beginning of this text was awarded. With that, Mg is currently the quintessential dopant for achieving *p*-type nitrides for wurtzite [32–34]; nevertheless, although there is somewhat extensive research of *p*-type doping with Mg in zincblende [35–38], there has not been a clear description of its effects on crystalline purity and quality of the obtained material.

1.2 Objectives of the work

With all that in mind, the main objective of this work was:

- To find the optimal conditions to obtain high crystalline purity and quality of undoped and *p*-type, Mg doped zincblende GaN epilayers grown on GaAs (001) substrates by MBE.

Among the parameters that may be studied to better understand and help solve the aforementioned problematics, for both doped and undoped GaN, growth temperature and the Ga/N stoichiometric ratio, closely related, are two of the most influential on the material properties. For that reason, the present work's particular objectives were:

- To study the effects of growth temperature during the first stages, e.g., < 5 nm, of the growth on the phase purity and crystalline quality of epitaxially grown zincblende GaN on GaAs (001) substrates.

- To study the effect of Ga/N ratio and Mg cell temperature on phase purity and crystalline quality of the *p*-type doped zincblende GaN epilayers.

1.3 Summary

The work carried out to those ends is hereby reported. For convenient navigation, the report is structured into 4 parts. **Part I** comprises the current **Chapter 1**, presenting motivation, objectives, and a summary.

Part II reviews relevant background theory. **Chapter 2** describes properties of nitride semiconductors, including crystalline structure, bandgaps, and polarization. Applications in electronics and optics comparing wurtzite and zincblende phases are also discussed. **Chapter 3** details MBE conditions for wurtzite and zincblende GaN. **Chapter 4** explains x-ray diffraction geometry, types of measurements, giving pole figure analysis—the primary technique used here—for orientation and phase content calculation.

Then, **Part III** describes pole figure simulation methodology in **Chapter 5**, covering key geometric considerations and calculations, such as orthogonalization and rotations. For clarity, two examples are given for wurtzite and one of its twins.

Finally, **Part IV** presents experimental results. **Chapter 6** investigates the effects of initial growth stages on crystal purity and quality of epitaxial zincblende GaN grown on GaAs (001) by MBE. On the other hand, **Chapter 7** examines purity and quality of Mg-doped samples with different Ga/N ratios and various Mg cell temperatures used during the MBE growth. To close, **Chapter 8** summarizes key findings and conclusions for both experimental chapters.

Part II: Literature Review

Chapter 2: Nitride Semiconductors: Properties and Applications

2.1 General properties

Gallium nitride (GaN), as well as the other nitrides, can be found in three different crystalline structures, namely *wurtzite* (space group P6_3mc), *zincblende* (space group F$\bar{4}$3m), and *rocksalt* (space group Fm$\bar{3}m$) [39]. First, the wurtzite structure has a hexagonal unit cell consisting of two group-III metals and two nitrogen atoms. Each kind of atom form a hexagonal close-packed sub-lattice (one for the group-III metal and one for N atoms) separated along the c axis by 5/8 of the cell height from each other.

On the other hand, the zincblende structure has a cubic unit cell, consisting of four metallic and four N atoms arranged in two cubic close-packed, or face-centered cubic (FCC), sub-lattices (one for the anions and one for the cations) displaced 1/4 of the body diagonal from one another.

Finally, the rocksalt consists of, yet again, one FCC sub-lattice for each kind of atom; however, in this case, the separation between the two is 1/2 along the sides of the unit cell. **Fig. 2.1** shows the unit cells of wurtzite, zincblende, and rocksalt nitrides and **Table 2.1** shows their lattice parameters.

Table 2.1. Lattice parameters of wurtzite and zincblende nitrides. Note that for the former, $a = b$ and $\alpha = \beta$, while, for the latter, $a = b = c$ and $\alpha = \beta = \gamma$.

	Wurtzite [40]			Zincblende [41–43]			Rocksalt [43, 44]		
	GaN	AlN	InN	GaN	AlN	InN	GaN	AlN	InN
Space group	P6_3mc			F$\bar{4}$3m			Fm$\bar{3}m$		
a/Å	3.190	3.110	3.533	4.503	4.372	4.960	4.230	4.070	4.630
c/Å	5.189	4.980	5.692						
α/deg	90			90			90		
γ/deg	120								

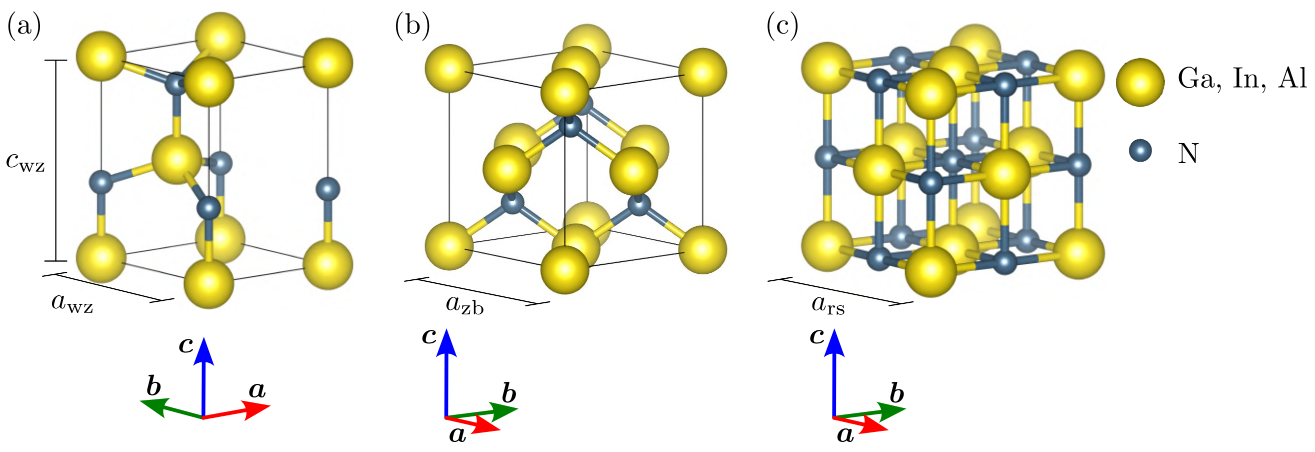

Fig. 2.1. Unit cells of (a) wurtzite, (b) zincblende, and (c) rocksalt GaN. Drawn using *VESTA3* [45] with data from [40] for wurtzite and [43] for zincblende and rocksalt. The crystal basis vectors are shown for each structure.

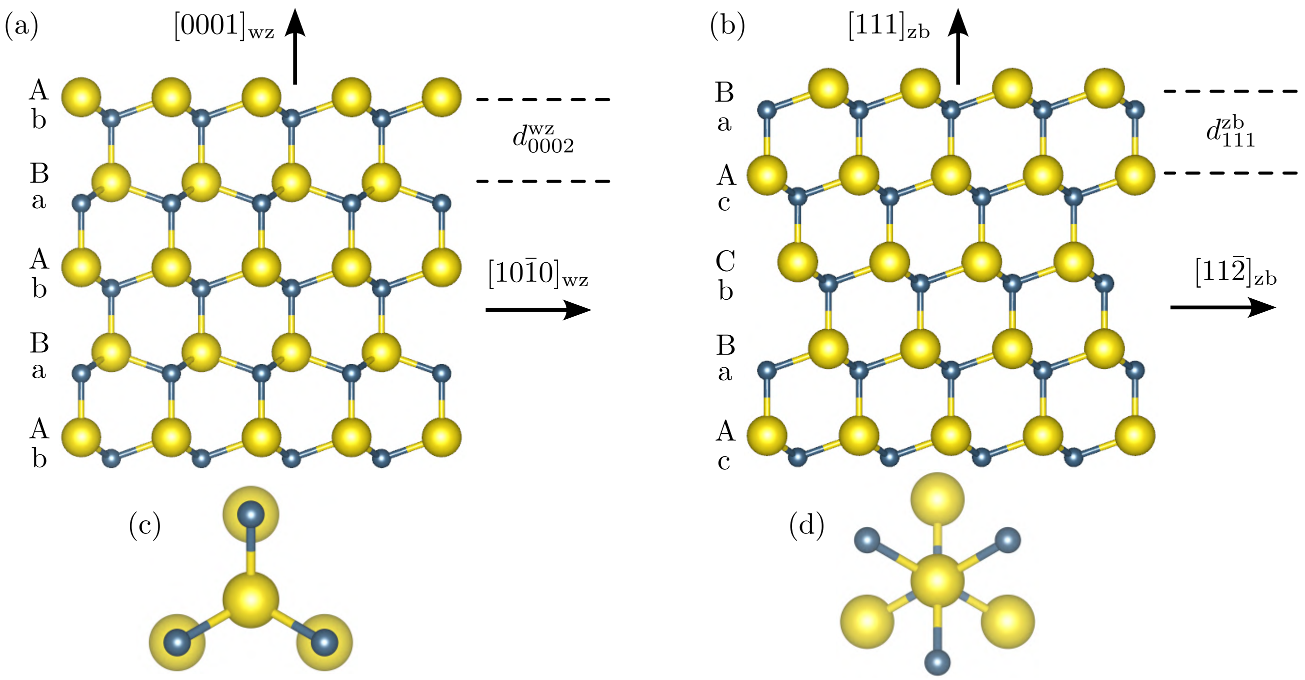

Fig. 2.2. Stacking sequence of (a) wurtzite and (b) zincblende in views along $[10\bar{1}0]_{\mathrm{wz}}$ and $[11\bar{2}]_{\mathrm{zb}}$ so that the close packed directions lie vertically along the $[0001]_{\mathrm{wz}}$ and $[111]_{\mathrm{zb}}$ directions, respectively. Views from below show (c) the aBb**A** stacking for wurtzite and (d) the aBb**C** for zincblende.

Due to the high pressures required for producing the rocksalt phase [43], nitrides in the said phase cannot be grown by molecular beam epitaxy; therefore, from this point on, the discussion is centered around the other two phases. The crystal structures of wurtzite and zincblende nitrides are remarkably alike. Both structures consist of close packed lattices, in which the group-III cations are tetrahedrally coordinated by four N anions and vice versa. The main difference between the two polytypes is the stacking sequence of the close-packed planes.

Whereas, in wurtzite nitrides, the $(0002)_{\mathrm{wz}}$ planes have an ...AaBbAaBbAaBb... stacking, zincblende $(111)_{\mathrm{wz}}$ planes exhibit an ...AaBbCcAaBbCc... stacking sequence. Aa, Bb, and Cc denote metal-N bilayers, as schematically shown in **Fig. 2.2**, where the close-packed planes are perpendicular to the vertical direction in both cases for an easier comparison.

Even in the schematic representation, the space between the close-packed planes seems very similar for both structures. For more precision, however, the interplanar distances can be calculated via **Eq. (4.11)**, for the wurtzite polytype, and **Eq. (4.12)** for zincblende nitrides. Using the lattice parameters given in **Table 2.1** results in a d_{0002}^{wz} of 2.594 Å and a d_{111}^{zb} of 2.599 Å, which are nearly identical. Moreover, the views from below in **Fig. 2.2** show that the two stacking sequences differ only by a rotating through 60° around the $[0001]_{\mathrm{wz}}/[111]_{\mathrm{zb}}$, making the two structures remarkably similar to one another.

Table 2.2. Bandgap, lattice parameters, and bowing factors for some semiconductor alloys.

Material		E_g/eV	a/Å	Alloy	b_{E_g}	b_a
Wz nitrides [46]	GaN	3.470	3.190	AlGaN	1.775	0.006
	AlN	6.300	3.110	InGaN	1.775	0.140
	InN	0.770	3.533	AlInN	3.678	0.040
Zb nitrides [46]	GaN	3.270	4.503	AlGaN	0.391	-0.007
	AlN	6.250	4.372	InGaN	1.164	-0.011
	InN	0.620	4.960	AlInN	1.464	-0.015
Arsenides [47]	GaAs	1.519	5.653	AlGaAs	0.055	0
	AlAs	3.099	5.665	InGaAs	0.477	0
	InAs	0.417	6.058	AlInAs	0.700	0
Phosphides [47]	GaP	2.886	5.450	AlGaP	0	0
	AlP	3.630	5.467	InGaP	0.650	0
	InP	1.423	5.869	AlInP	-0.480	0
Antimonides [47]	GaSb	0.812	6.095	AlGaSb	-0.044	0
	AlSb	2.386	6.135	InGaSb	0.415	0
	InSb	0.235	6.479	AlInSb	0.430	0
Tellurides [48]	CdTe	1.560	6.480	-	-	-
	ZnTe	2.310	6.103	-	-	-
Selenides [48]	CdSe	1.910	6.220	-	-	-
	ZnSe	5.740	2.830	-	-	-
Si [49]		1.560	5.431	-	-	-
Ge [49]		0.665	5.655	-	-	-

This results in very similar optoelectronic properties. More specifically, the bandgaps of both polymorphs exhibit a wide coverage of the spectrum, ranging from 0.77 eV for InN up to 6.3 eV for AlN, passing through 3.47 eV for GaN (**Table 2.2**), all in wurtzite phase. Similarly, the range in the zincblende phase goes from 0.62 eV for InN, to 3.27 eV for GaN, and up to 6.25 eV for AlN (**Table 2.2**).

A complete description of the bandgaps, and the lattice parameters, for the three $A_xB_{(1-x)}N$ ternaries can be carried out with Vegard's law

$$P_{A_xB_{(1-x)}N} = xP_{AN} + (1-x)P_{BN} - x(1-x)b_{A_xB_{(1-x)}N}, \tag{2.1}$$

where $P_{A_xB_{(1-x)}N}$ is the bandgap, or lattice parameter, of the alloy, P_{AN} and P_{BN} the same for the AN and BN binaries entailing the $A_xB_{(1-x)}N$ alloy, with bowing parameter $b_{A_xB_{(1-x)}N}$ and a composition of A and B can be Ga, Al, or In.

Fig. 2.3 shows a plot of the bandgaps of these three materials for both polytypes, along with the ternaries in between them as a function of composition and lattice parameter a calculated using **Eq. (2.1)** with data from **Table 2.2**. Arsenides, phoshides, antimonides, tellurides, Si and Ge are added for comparison.

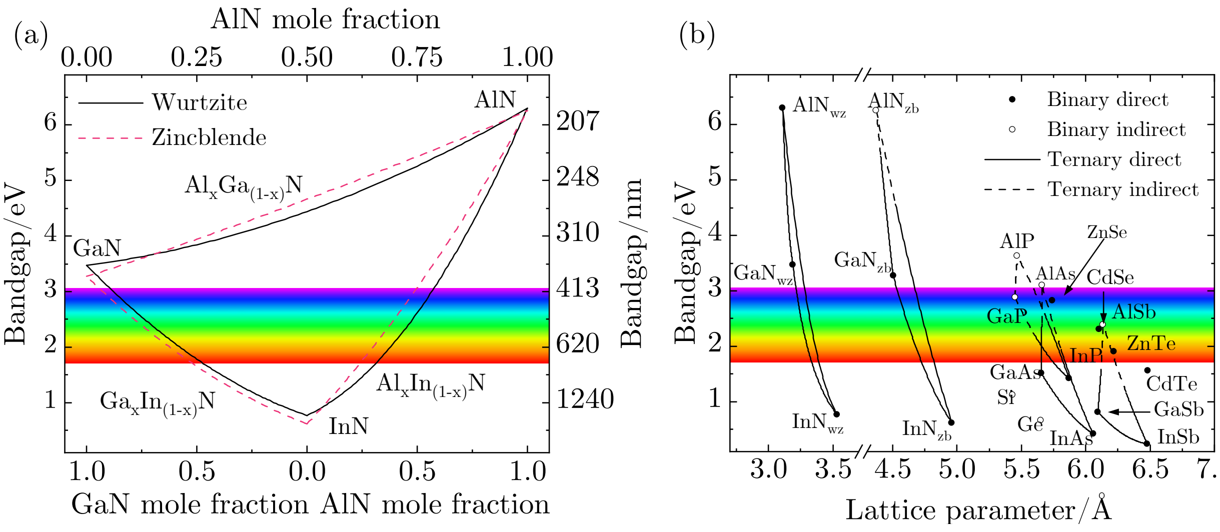

Fig. 2.3. (a) bandgaps of GaN, AlN, InN and their ternaries for wurtzite and zincblende and a comparison (b) with different materials. Calculated with **Eq. (2.1)**.

Fig. 2.3 illustrates one of the greatest advantages of nitrides over other semiconductors. The wide range of bandgaps they cover, from infrared through the whole visible spectrum and up to the ultraviolet, is partly what translates into the wide range of applications in which they are used. Moreover, the bandgaps of nitrides are direct for most of that outstandingly wide range.

For wurtzite nitrides, the whole system exhibits direct bandgaps, contrary to arsenides, phosphides, and antimonides, where the Al binaries, and ternaries containing certain amounts of it, display indirect bandgaps. Unfortunately, nitrides in the zincblende phase also suffer from this problem, having AlN and ternaries with high contents of Al with indirect bandgaps.

Additionally, the figure also points out one of the main disadvantages of nitrides. While the rest of the material systems exhibit lattice constants that area close to each other, nitrides are farther away towards smaller lattice parameters. This makes it more difficult to integrate them with existing technologies based on the other semiconductor groups due to the large lattice mismatch. Finally, other general properties of nitrides are shown in **Table 2.3**.

Table 2.3. General properties of nitride semiconductors. Data taken from [39] unless stated otherwise.

Properties	Wurtzite		
	GaN	AlN	InN
Breakdown field in MV/cm	3.5 [50] 5 [52]	4[51] 5.84 [53]	- -
Electron affinity in eV	3.9 [54]	1.44 [54]	5.5 [54]
Dielectric constants	$\parallel c$ 10.4 $\perp c$ 9.5	$\parallel c$ 9.32 $\perp c$ 7.76	$\parallel c$ 13.1 $\perp c$ 14.4
Effective electron mass	$m_e^{\parallel} = 0.2m_0$ $m_e^{\perp} = 0.2m_0$	$m_e^{\parallel} = 0.35m_0$ [55] $m_e^{\perp} = 0.25m_0$	$m_e^{\parallel} = 0.138m_0$ [55] $m_e^{\perp} = 0.141m_0$ [55]
Effective hole mass	$m_{hh}^{\parallel} = 1.1m_0$ $m_{hh}^{\perp} = 1.6m_0$ $m_{lh}^{\parallel} = 1.1m_0$ $m_{lh}^{\perp} = 0.15m_0$	$m_{hh}^{\parallel} = 3.13m_0$ [56] $m_{hh}^{\perp} = 10.42m_0$ [57] $m_{lh}^{\parallel} = 4.41m_0$ [55] $m_{lh}^{\perp} = 0.35m_0$ [55]	$m_{hh}^{\parallel} = 2.493m_0$ [55] $m_{hh}^{\perp} = 2.661m_0$ [55] $m_{lh}^{\parallel} = 2.493m_0$ [55] $m_{lh}^{\parallel} = 0.196m_0$ [55]
	Zincblende		
	GaN	AlN	InN
Breakdown field in MV/cm	$\sim$5 [58]		-
Electron affinity in eV	3.4 [54]	2.08 [54]	5.2 [54]
Dielectric constants	9.7 [58]	9.56	8.4
Effective electron mass	$m_e^{\parallel} = 0.13m_0$[55]	$m_e^{\parallel} = 0.23m_0$	$m_e^{\parallel} = 0.13m_0$ [55]
Effective hole mass	$m_{hh}^{[001]} = 0.8m_0$ [59] $m_{lh}^{[001]} = 0.21m_0$	$m_{hh}^{[001]} = 1.02m_0$ [55] $m_{lh}^{[001]} = 0.37m_0$ [55]	$m_{hh}^{[001]} = 1.18m_0$ [55] $m_{lh}^{[001]} = 0.21m_0$ [55]

2.2 Polarization properties

Spontaneous and piezoelectric polarization are two properties that the nitride semiconductors exhibit due to the symmetry of their unit cells. These two kinds of polarization are strong enough that can significantly affect device performance in both negative and positive ways. Therefore, it is of significant importance to understand such effects.

Consider the ball and stick representation of the nitrides' tetrahedra with the staking planes displayed horizontally, i.e., wurtzite's [0001] or zincblende's [111] directions pointing upwards, in **Fig. 2.4**.

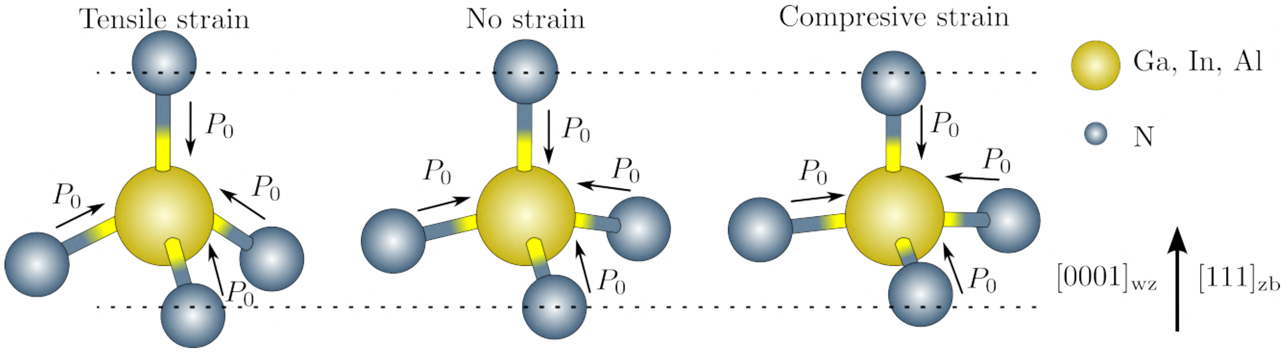

Fig. 2.4. Nitride tetrahedra showing compressive strain, no strain, and tensile strain along the $[0001]_{\text{wz}}||[111]_{\text{zb}}$ axes. Adapted from [60].

The differences in electronegativity between the centered metallic cation and the N atoms at the corners causes electrons to be close to the corners of the tetrahedrons. This brings about a polarization P_0 towards the metallic atoms in the center, where the vertical components of the triple bounds on the bottom cancel out the polarization due to the vertical bond when the tetrahedron is ideal.

However, this does not hold when, for example, there is tensile or compressive strain along the plane formed by the three N atoms below in the figure. In such a case, there is a net polarization resulting from the vertical Ga-N bond and the vertical components of the other three bonds. With tensile strain, there is a resulting polarization pointing upwards, whereas compressive strain causes a polarization pointing downwards.

This causes is the so called piezoelectric effect and generates a polarization $\boldsymbol{P}^{\text{pz}}$ in the bulk material whose components are defined by [60]

$$P_i^{\text{pz}} = \sum_{j,k} e_{ijk}\varepsilon_{jk}, \tag{2.2}$$

where e_{ijk} are the piezoelectric coefficients, components of the third-rank piezoelectric tensor $\boldsymbol{e}$ and ε_{jk} the components of the second-rank strain tensor $\boldsymbol{\varepsilon}$. **Eq. (2.2)** stands for 3 equations, each with 9 terms on the right-hand side for a total of 27 piezoelectric coefficients.

Using Voigt notation, however, e_{ijk} can be reduced to e_{ij} and ε_{jk} to ε_j [61], so that **Eq. (2.2)** can be rewritten as

$$P_i^{\mathrm{pz}} = e_{ij}\varepsilon_j, \tag{2.3}$$

which in matrix form is

$$\begin{bmatrix} P_x \\ P_y \\ P_z \end{bmatrix}_{\mathrm{wz}}^{\mathrm{pz}} = \begin{bmatrix} 0 & 0 & 0 & 0 & e_{15} & 0 \\ 0 & 0 & 0 & e_{15} & 0 & 0 \\ e_{31} & e_{31} & e_{33} & 0 & 0 & 0 \end{bmatrix} \begin{bmatrix} \varepsilon_{xx} \\ \varepsilon_{yy} \\ \varepsilon_{zz} \\ \varepsilon_{yz} \\ \varepsilon_{xz} \\ \varepsilon_{xy} \end{bmatrix}, \tag{2.4a}$$

$$\begin{bmatrix} P_x \\ P_y \\ P_z \end{bmatrix}_{\mathrm{zb}}^{\mathrm{pz}} = \begin{bmatrix} 0 & 0 & 0 & e_{14} & 0 & 0 \\ 0 & 0 & 0 & 0 & e_{14} & 0 \\ 0 & 0 & 0 & 0 & 0 & e_{14} \end{bmatrix} \begin{bmatrix} \varepsilon_{xx} \\ \varepsilon_{yy} \\ \varepsilon_{zz} \\ \varepsilon_{yz} \\ \varepsilon_{xz} \\ \varepsilon_{xy} \end{bmatrix}, \tag{2.4b}$$

for wurtzite and zincblende, using their respective point group symmetry to simplify the reduced piezoelectric tensor [61], leaving three distinct coefficients for the former and one for the later. Moreover, ε_{xx}, ε_{yy}, ε_{zz} are tensile or compressive strain components along the x, y, and z axes, respectively, and ε_{yz}, ε_{xz}, and ε_{xy} are the shear strain components.

It is important to notice that, in wurtzite geometry, the x axis points to the normal to the so-called *m-plane* $(1\bar{1}00)$, the y axis to the normal to the *a-plane* $(11\bar{2}0)$, and the z axis to the *c-plane* (0001) [39]. As for zincblende, $x||[100]$, $y||[010]$ and $z||[001]$.

By solving the matrix multiplication in **Eq. (2.4)**, one gets

$$\begin{bmatrix} P_x \\ P_y \\ P_z \end{bmatrix}_{\mathrm{wz}}^{\mathrm{pz}} = \begin{bmatrix} e_{15}\varepsilon_{xz} \\ e_{15}\varepsilon_{yz} \\ e_{31}(\varepsilon_{xx} + \varepsilon_{yy}) + e_{33}\varepsilon_{zz} \end{bmatrix}, \tag{2.5a}$$

$$\begin{bmatrix} P_x \\ P_y \\ P_z \end{bmatrix}^{\mathrm{pz}}_{\mathrm{zb}} = \begin{bmatrix} e_{14}\varepsilon_{yz} \\ e_{14}\varepsilon_{xz} \\ e_{14}\varepsilon_{xy} \end{bmatrix}. \tag{2.5b}$$

In epitaxially grown nitrides, such as the subject of this work, shear strain can be considered non existent. Thus, in zincblende, due to **Eq. (2.5b)**, polarization along all directions is 0. The same goes for wurtzite along the $[1\bar{1}00]m$ and $[11\bar{2}0]a$ directions according to **Eq. (2.5a)**. The only term left is then polarization along the z axis in wurtzite

$$P_z^{\mathrm{pz}} = e_{31}(\varepsilon_{xx} + \varepsilon_{yy}) + e_{33}\varepsilon_{zz}. \tag{2.6}$$

With the help of the generalized form of Hooke's law [62]

$$\sigma_{ij} = \sum_{kl} C_{ijkl}\varepsilon_{kl}, \tag{2.7}$$

where σ_{ij} are the components of the second-rank stress tensor $\boldsymbol{\sigma}$ and C_{ijkl} the components of the fourth-rank elastic tensor $\boldsymbol{C}$ and represents the elastic stiffness constants of the crystal.

Although there are a total of 81 stiffness coefficients, they can be reduced due to symmetry of the crystal class to 36 so that, with Voigt notation, Hooke's law can be rewritten in a simplified form as follows

$$\sigma_i = \sum_j C_{ij}\varepsilon_j, \tag{2.8}$$

where σ_{ij} was reduced to σ_i in the same manner. In matrix notation, for wurtzite, **Eq. (2.8)** can be rewritten as [15]

$$\begin{bmatrix} \sigma_{xx} \\ \sigma_{yy} \\ \sigma_{zz} \\ \sigma_{yz} \\ \sigma_{xz} \\ \sigma_{xy} \end{bmatrix} = \begin{bmatrix} C_{11} & C_{12} & C_{13} & 0 & 0 & 0 \\ C_{12} & C_{11} & C_{13} & 0 & 0 & 0 \\ C_{13} & C_{13} & C_{33} & 0 & 0 & 0 \\ 0 & 0 & 0 & C_{44} & 0 & 0 \\ 0 & 0 & 0 & 0 & C_{44} & 0 \\ 0 & 0 & 0 & 0 & 0 & \frac{C_{11}-C_{12}}{2} \end{bmatrix} \begin{bmatrix} \varepsilon_{xx} \\ \varepsilon_{yy} \\ \varepsilon_{zz} \\ \varepsilon_{yz} \\ \varepsilon_{xz} \\ \varepsilon_{xy} \end{bmatrix}. \tag{2.9}$$

If the crystal is stressed in the (0001) plane, and allowed to expand or compress in the [0001] direction, i.e., if the growth direction is along the c axis, then σ_{xx} and σ_{yy} are the only non-zero components of $\boldsymbol{\sigma}$ and **Eq. (2.9)** has only three nonvanishing terms

$$\begin{bmatrix} \sigma_{xx} \\ \sigma_{yy} \\ 0 \end{bmatrix} = \begin{bmatrix} C_{11} & C_{12} & C_{13} \\ C_{12} & C_{11} & C_{13} \\ C_{13} & C_{13} & C_{33} \end{bmatrix} \begin{bmatrix} \varepsilon_{xx} \\ \varepsilon_{yy} \\ \varepsilon_{zz} \end{bmatrix}. \tag{2.10}$$

With biaxial strain, which is the case for epitaxial films [60], $\varepsilon_{xx} = \varepsilon_{yy}$ leads to

$$\begin{bmatrix} \sigma_{xx} \\ \sigma_{yy} \\ 0 \end{bmatrix} = \begin{bmatrix} (C_{11} + C_{12})\varepsilon_{xx} + C_{13}\varepsilon_{zz} \\ (C_{11} + C_{12})\varepsilon_{xx} + C_{13}\varepsilon_{zz} \\ 2C_{13}\varepsilon_{xx} + C_{33}\varepsilon_{zz} \end{bmatrix}, \tag{2.11}$$

whose third equation describes the Poisson effect

$$\varepsilon_{zz} = -\frac{2C_{13}}{C_{33}}\varepsilon_{xx}. \tag{2.12}$$

Combining **Eq. (2.12)** and **Eq. (2.6)** yields

$$P_z^{\mathrm{pz}} = 2\varepsilon_{xx}\left(e_{31} - e_{33}\frac{C_{13}}{C_{33}}\right), \tag{2.13}$$

which describes the piezoelectric polarization in terms of four material constants and ε_{xx}, which, in turn, represents the ratio of change of the in-plane lattice constant.

For pseudomorphic epitaxial films, that can be described by

$$\varepsilon_{xx} = \frac{a_{\mathrm{s}} - a_{\mathrm{r}}}{a_{\mathrm{r}}}, \tag{2.14}$$

where a_{s} and a_{r} are the strained lattice constant of the epitaxial film and its relaxed value.

Piezoelectric polarization is sometimes also treated in terms of the piezoelectric moduli d_{ijk}, whose reduced form with Voigt notation is d_{ij}, as follows [62]

$$P_i^{\mathrm{pz}} = \sum_j d_{ij}\sigma_j. \tag{2.15}$$

Due to crystal class symmetry, d_{ij} has the exact same shape as e_{ij}, and, with the help of **Eq. (2.8)**, they can be related as [60]

$$e_{ij} = \sum_k d_{ik}C_{kj}. \tag{2.16}$$

Writing **Eq. (2.15)** in matrix form

$$\begin{bmatrix} P_x \\ P_y \\ P_z \end{bmatrix}^{\mathrm{pz}} = \begin{bmatrix} 0 & 0 & 0 & 0 & d_{15} & 0 \\ 0 & 0 & 0 & d_{15} & 0 & 0 \\ d_{31} & d_{31} & d_{33} & 0 & 0 & 0 \end{bmatrix} \begin{bmatrix} \sigma_{xx} \\ \sigma_{yy} \\ \sigma_{zz} \\ \sigma_{yz} \\ \sigma_{xz} \\ \sigma_{xy} \end{bmatrix} \tag{2.17}$$

and using the same considerations as before for epitaxially growth on the wurtzite c-plane ($\sigma_{zz} = \sigma_{yz} = \sigma_{xz} = \sigma_{xy} = 0$), it is clear that only one component of $\boldsymbol{P}^{\mathrm{pz}}$ is left

$$P_z^{\mathrm{pz}} = 2d_{31}\sigma_{xx}. \tag{2.18}$$

Then, from **Eq. (2.8)**

$$\sigma_{xx} = (C_{11} + C_{12})\varepsilon_{xx} + C_{13}\varepsilon_{zz}. \tag{2.19}$$

Finally, with the aid of **Eq. (2.12)**, **Eq. (2.19)** can be rewritten as

$$\sigma_{xx} = \varepsilon_{xx}\left(C_{11} + C_{12} - 2\frac{C_{13}^2}{C_{33}}\right), \tag{2.20}$$

to, similarly to **Eq. (2.13)**, finally obtain the polarization component left in terms of five material constants and ε_{xx}

$$P_z^{\mathrm{pz}} = 2d_{31}\varepsilon_{xx}\left(C_{11} + C_{12} - 2\frac{C_{13}^2}{C_{33}}\right). \tag{2.21}$$

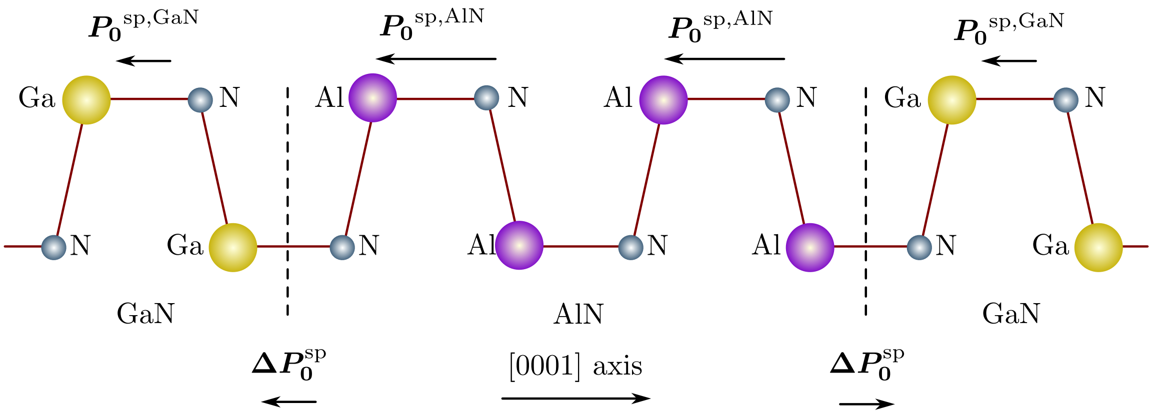

Fig. 2.5. GaN/AlN/GaN interfaces showing the directions of the spontaneous polarization and the difference formed at the interfaces. Adapted from [60].

As for spontaneous polarization, consider the schematic representation of the GaN/AlN/-GaN double interface along the c axis of wurtzite in **Fig. 2.5**. Due to the greater electronegativity difference of AlN compared to that of GaN's, the polarization in AlN is consequently greater. In the bulk of either material there is not any net polarization; however, at the interface between two nitrides, there is a net difference between the two values of polarization, and therefore, this results in accumulation of charges across the interface.

The total polarization is then

$$P_T = P_z^{\mathrm{pz}} + P_0^{\mathrm{sp}}, \tag{2.22}$$

where P_z^{pz} is the piezoelectric polarization described by **Eq. (2.13)** or **Eq. (2.21)** and P_0^{sp} is the difference of spontaneous polarization across a junction. Values of P_0^{sp}, e_{ij}, and C_{ij} are shown in **Table 2.4**.

Table 2.4. Spontaneous polarization P_0^{sp} (C/m^2), piezoelectric e_{ij} (C/m^2), and elastic C_{ij} (GPa) coefficients for wurtzite nitrides.

	P_0^{sp}	e_{31}	e_{33}	e_{15}	C_{11}	C_{12}	C_{13}	C_{33}	C_{44}	Reference
GaN	-0.034[a]	0.17	0.29	0.10	359.4	129.2	92.0	389.9	98.0	[63]
		-0.14	1.15	-0.22	359.7	129.9[b]	104.6	391.8	99.6	[64]
AlN	-0.090[a]	-0.58	1.55	-0.48	345.0	125.0	120.0	395.0	118.0	[65]
		-0.58	1.39	-0.29	410.0	140.0	100.0	390.0	120.0	[66]
		-0.60	1.34	-0.32	402.5	135.6	101.0	387.6	122.9	[67]
InN	-0.042[a]	-0.41[a]	0.81[a]		227.0	114.0	94.0	242.0	48.0	[68]
							70.0[a]	205.0[a]		

[a] Reference [69]

[b] Value not given in reference. Calculated trough the relationship $C_{66} = \frac{C_{11}-C_{12}}{2}$

2.3 Applications of nitride semiconductors

There are two important areas in which nitride-based optoelectronic devices are used. Both of those are heavily affected by the so called *built-in* electric fields due to the polarization effects across junctions discussed in the previous section.

2.3.1 Power electronics applications

Due to the high breakdown voltage of nitrides (**Table 2.3**), compared to the typically used Si (0.3 MV/cm [49]) or GaAs (0.4 MV/cm [70]), they are used as a base for the high-electron-mobility transistor (HEMT), often sought for high-power electronics. For this kind of application, research is mainly focused on enhancing the piezoelectric response so that the amount of electrons in the channel increases [71–73].

A HEMT is a field-effect transistor that works using a heterojunction between two materials with different bandgaps [74]. Due to band bending at the junction, a quantum well (QW) is created, where electrons are confined vertically but free to move horizontally. This is known as a two-dimensional electron gas (2DEG) and serves as the transistor's channel in a HEMT (**Fig. 2.6**).

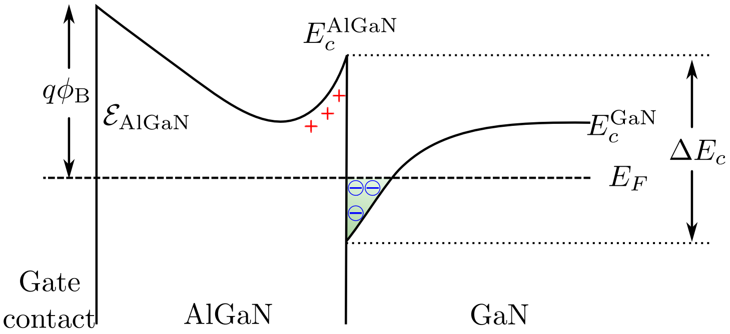

Fig. 2.6. Band structure at an AlGaN/GaN junction. Adapted from [75].

In a nitride-based HEMT, typically a pseudomorphic AlGaN *barrier* layer is used on top of a fully relaxed GaN buffer layer, as shown in **Fig. 2.7** along with polarization, both spontaneous and piezoelectric. The positive charges $+\sigma = \Delta P$ at the interface from the AlGaN side attract electrons on the GaN side, and confine them in the 2DEG.

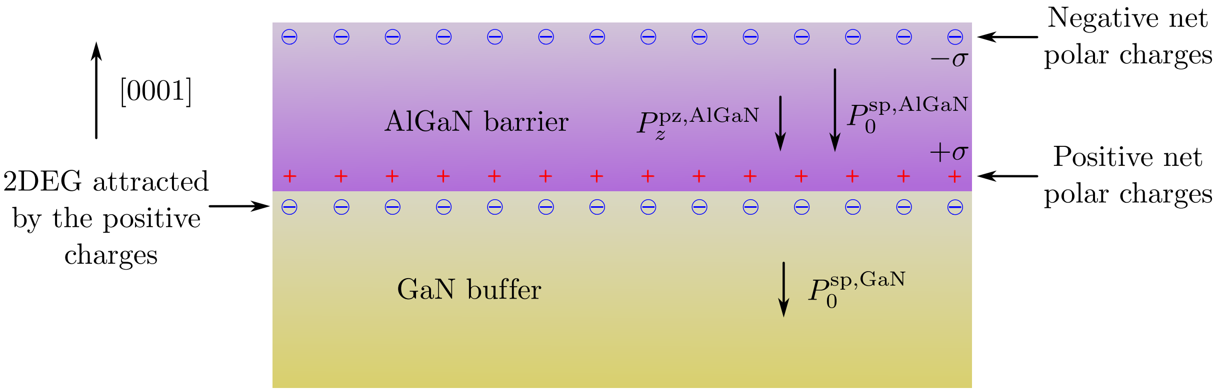

Fig. 2.7. Strained AlGaN on a relaxed GaN buffer showing the directions of polarization. Adapted from [75].

The amount of electrons in the 2DEG is approximately the same as the positive charge carriers at the interface [75], which can be estimated by

$$\Delta P = P_z^{\mathrm{pz,AlGaN}} + P_0^{\mathrm{sp,AlGaN}} - P_0^{\mathrm{sp,GaN}}. \tag{2.23}$$

Using Vegard's law to estimate the spontaneous polarization as follows

$$\Delta P(x) = -0.090x - 0.034(1-x) - 0.019x(1-x). \tag{2.24}$$

where x is the molar fraction of Al in $\mathrm{Al}_x\mathrm{Ga}_{(1-x)}\mathrm{N}$ and 0.019 is its bowing parameter for spontaneous polarization [60]. Using, for instance, an Al content of 30 %, results in $P_0^{\mathrm{AlGaN}} = -0.05479$. With the help of **Eq. (2.1)** to calculate a (and thus ε_{xx} with **Eq. (2.14)**), e_{31}, e_{33}, C_{13}, and C_{33} yields $P_z = -0.00948$ C/m^2 (**Eq. (2.13)**) for the AlGaN alloy. With that value combined with spontaneous polarization, the total polarization across the junction is $\Delta P = -0.02229$ C/m^2, which, in turn, yields an electron concentration of about $1.39\times10^{13} cm^{-2}$ (dividing ΔP by the elementary charge q). Experimental values in that range have already been reported in the literature [76–78], along with a more precise estimation of the carrier density n_s at the 2DEG by Ambacher et al. [76]

$$n_s = \frac{\Delta P}{q} - \left(\frac{\epsilon_0\epsilon}{tq^2}\right)(q\phi_B + E_F - \Delta E_c), \tag{2.25}$$

ϵ_0 is the vacuum permittivity, ϵ and t the dielectric constant and thickness, respectively, of AlGaN, ϕ_B the height barrier of the gate contact, E_f the Fermi level, and ΔE_c the offset of conduction band at the junction. A plot of **Eq. (2.25)** as function of Al content in AlGaN is shown in **Fig. 2.8** for three different AlGaN values of thickness.

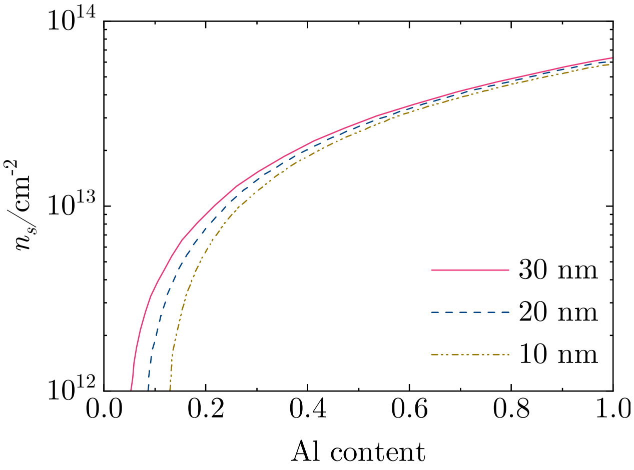

Fig. 2.8. Sheet carrier density at the 2DEG formed at an AlGaN/GaN junction with different Al contents. Plotted with data from [76].

As seen from **Eq. (2.25)**, there are different means to increase n_s other than increasing the polarization difference across the junction. For instance, the thickness of the barrier can be increased. Yet, care must be taken because, if t reaches and crosses the critical thickness, the ternary layer may relax, causing crystallographic defects and reducing P_z^{pz}. Additionally, ΔE_c can be increased by using higher Al contents.

Since the electrons at the channel are induced by polarization, there is no need for doping at the GaN layer. Therefore, the lack of positively charged donors reduces electron scattering, with which mobilities up to 2000 $\mathrm{cm}^2/\mathrm{Vs}$ are achieved at room temperature [79].

A finalized representation of a HEMT is shown in **Fig. 2.9**, showing the all its main components. First, a substrate, typically sapphire, SiC or Si, on top of which a thin nucleation layer is grown to improve quality. Then, a GaN buffer layer, where the channel is located below the junction with the AlGaN barrier. Finally, gate, drain, and source to connect the device and a pasivation layer to protect it are deposited.

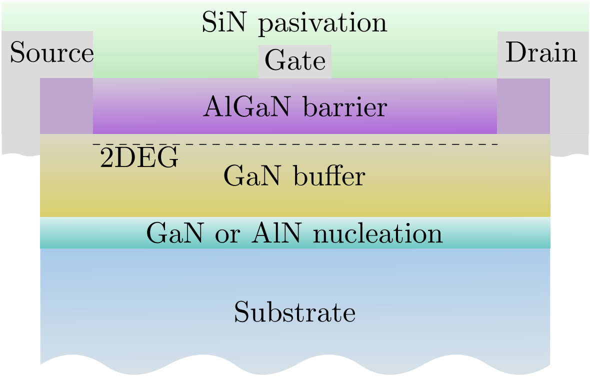

Fig. 2.9. HEMT structure showing the basic components. Adapted from [80].

2.3.2 Zincblende nitrides in power electronics

It has been discussed that the 2DEG forms naturally at the AlGaN/GaN junction without the need of an applied bias [9]. This behavior describes a *normally-on* HEMT, which work nicely in low-voltage applications. Nevertheless, when higher voltages are required for power switching, *normally-off* (no conduction at 0 bias) devices are preferred due to higher safety [13]. A normally-off HEMT is also referred to as enhancement mode HEMT (E-HEMT) [10].

Different approaches have been made in order to produce nitride E-HEMT: using a recessed-Gate [10], F-ion implantation [12], and inserting a p-type GaN layer above the barrier [13]. All three approaches seek to deplete the 2DEG so that there is no current flowing between drain and source unless a positive gate bias is applied. In the first approach, the thin AlGaN resulting from recessing the gate do not provide enough carriers to the buffer and the 2DEG is not even formed.

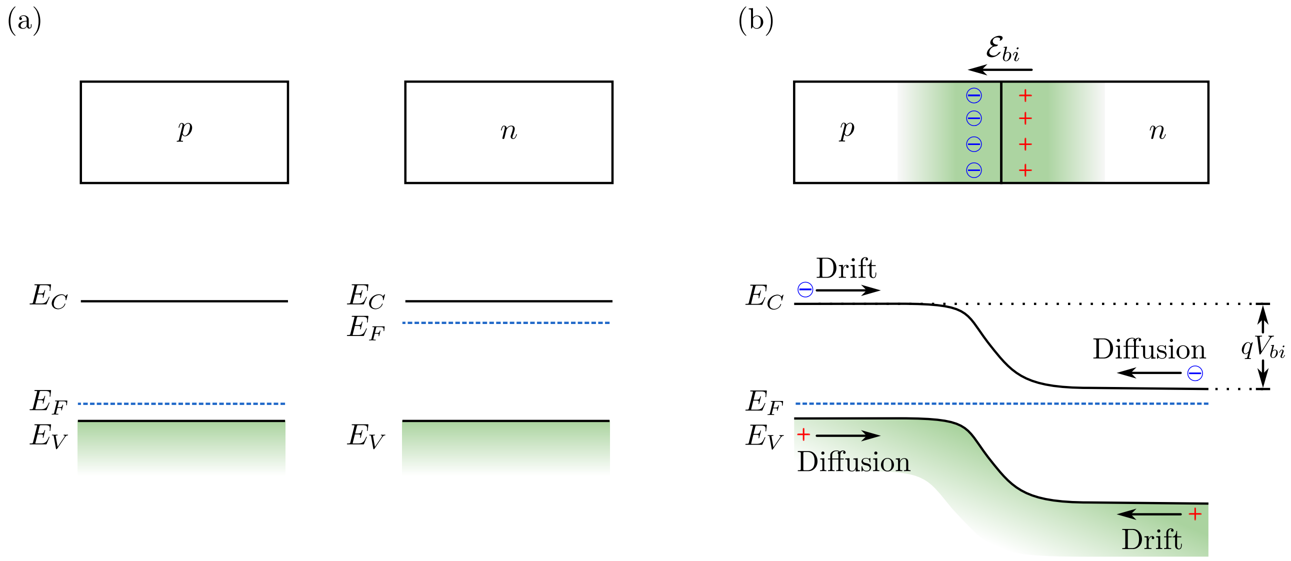

Fig. 2.10. *p*-*n* junction before and after metallurgical contact. Adapted from [81].

Furthermore, in the ion implantation approach, the potential created by the negatively charged F ions implanted below the gate leads the electronic bands (see **Fig. 2.6**) to move upward, preventing also the formation of the 2DEG. Finall, much like in the band diagram shown in **Fig. 2.10**, the p-GaN insertion approach causes a lift the energy bands, yielding the same result as F ion implantation.

These methods for preventing the formation of a 2DEG at 0 gate bias, nonetheless, require a fine control of etching, implantation, doping, and growth. Recalling that **Eq. (2.5)b** indicates that zincblende nitrides are naturally polarization-free, using this phase instead of wurtzite is a sound proposition to produce reliable E-HEMT [9]. In this case, there is no need for complicated procedures such as etching or ion implantation, since the absence of built-in electric fields avoids the formation of a 2DEG.

2.3.3 Light emitters

As mentioned before, the bandgaps of the nitride semiconductor system span a wide range from approximately 0.7 to 6.2 eV, covering the infrared region, the entire visible, and part of the ultraviolet spectrum (see **Fig. 2.3**). Therefore, they offer a great option as light emitters for various applications. While the active region of modern light emitters is a quantum well, their working principle is similar to that of traditional semiconductor devices.

Traditional semiconductor light emitters operate based on a light-emitting diode formed by a *p*-*n* junction, which is achieved when a *p*- and an *n*-type materials are brought into metallurgical contact. At the junction, electrons from the *n*-type side and holes from the *p*-type side diffuse towards the junction, where they recombine. This ongoing process leads to the accumulation of positive charge due to uncompensated, immobile donors in the n-type region. Conversely, negatively charged acceptors are left in the p-type side with no holes to neutralize their charge [81].

This creates a so-called *depletion* region devoid of free carriers and a built-in electric field $\mathcal{E}_{bi}$ (with corresponding potential difference V_{bi}) across the junction, inducing a drift current that opposes diffusion until there is no net current. The band diagrams of this region is shown before contact in **Fig. 2.10(a)** and after contact **Fig. 2.10(b)**, where a qV_{bi} barrier at the junction is established at the junction, with q the elementary charge.

Under equilibrium, i.e., no injected carriers, the Fermi E_F level across the junction remains constant, and the electron n and hole p concentrations at a temperature T are given by [81]

$$n = n_i \exp(\frac{E_F - E_i}{kT}) \tag{2.26a}$$

$$p = n_i \exp(\frac{E_i - E_F}{kT}), \tag{2.26b}$$

where n_i is the intrinsic carrier concentration, E_i is the intrinsic Fermi level, and k is the Boltzmann constant. Moreover, the product

$$pn = n_i^2 \tag{2.27}$$

holds.

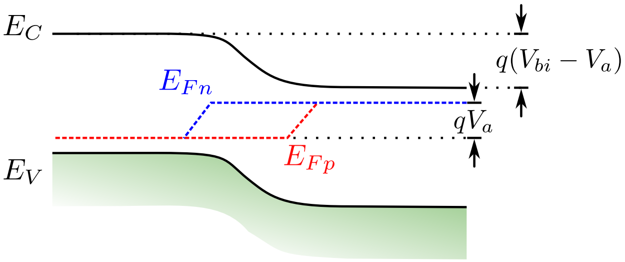

Fig. 2.11. Biased p-n-junction. Adapted from [81].

When, an external forward bias V_a is applied, the equilibrium breaks due to the injected charge carriers, leading to the band diagram in **Fig. 2.11**. In such a case, the external electric field decreases the barrier height by qV_a and splits the Fermi level to account for the excess charge carriers on both sides of the junction, leaving a quasi-Fermi level E_{Fn} for electrons on the n-type side and a quasi-Fermi level E_{Fp} for holes on the p-type side, where

$$E_{Fn} - E_{Fp} = qV_a \tag{2.28}$$

Taking these two new quasi-Fermi levels into account, the new charge carrier concentration is

$$n = n_i \exp(\frac{E_{Fn} - E_i}{kT}) \tag{2.29a}$$

$$p = n_i \exp(\frac{E_i - E_{Fn}}{kT}), \tag{2.29b}$$

with their product

$$pn = n_i^2 \exp(\frac{E_{Fn} - E_{Fp}}{kT}). \tag{2.30}$$

With $V_a > 0$, it follows from **Eq. (2.28)** and **Eq. (2.30)** that the product $pn > n_i^2$ increases exponentially with applied bias. Thus, the depletion region, devoid of charge carriers under equilibrium, now finds itself flooded with excess electrons and holes that can recombine radiatively, generating a photon with energy $h\nu = E_g + kT$, where h is Plank's constant. For practical reasons, kT is usually ignored so that

$$h\nu = E_g. \tag{2.31}$$

Although radiative recombination recombination may occur inside the p- or n-type materials alone, the amount of holes in the n-type, or free electrons on the p-type, material is extremely low that the amount of times recombination happens is not enough for it to make a properly functional device. At the junction, however, both charge carriers are found in enough quantities, as depicted in **Fig. 2.12(a)**.

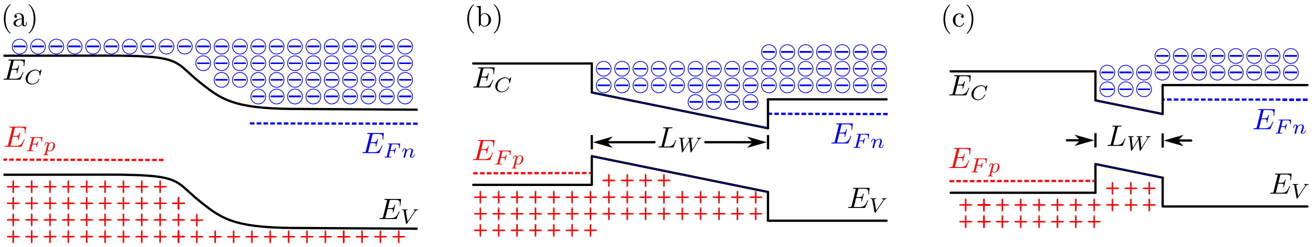

Fig. 2.12. Profile of a p-n-junction. Adapted from [82].

Since the amount of light being emitted by a solid-state device depends on the amount of times radiative recombination takes place, and this, in turn, depends on the amount of carriers at the active region of the device, it is imperative to increase carrier concentration to increase efficiency [82]. In the first place, a double heterostructure can be used, in which an undoped material, e.g., GaN (InN), is sandwiched in between an n-type and a p-type layer of a larger-bandgap material, e.g., AlN (GaN). This creates an electronic band structure as shown in **Fig. 2.12(b)** that traps electrons and holes inside the samller-bandgap material, increasing considerably radiative efficiency.

Moreover, if the thickness of the central layer, L_W is reduced to the order of the de Broglie wavelength, a quantum well as depicted in **Fig. 2.12(c)** is formed. The potential barriers confine carriers to two-dimensional movement, producing sharper carrier densities and increasing even more the efficiency of the device. Using a thin layer, additionally, allows for the use of higher bandgap differences (through the use of different compositions) since reaching the critical thickness is avoided. **Fig. 2.13** show the representation of GaN/InGaN/GaN and AlGaN/-GaN/AlGaN QW structures. Finally, due to the confinement, the allowed states within the well are pushed to higher energies above (below) the edge of the conduction (valence) band, so that higher-energy emission can be attained. **Eq. (2.31)** then becomes [83]

$$h\nu = E_g + e_1^- + h_1^+, \tag{2.32}$$

where e_1^- and h_1^+ are the first allowed energy states for electrons and holes in the conduction and valence bands, respectively.

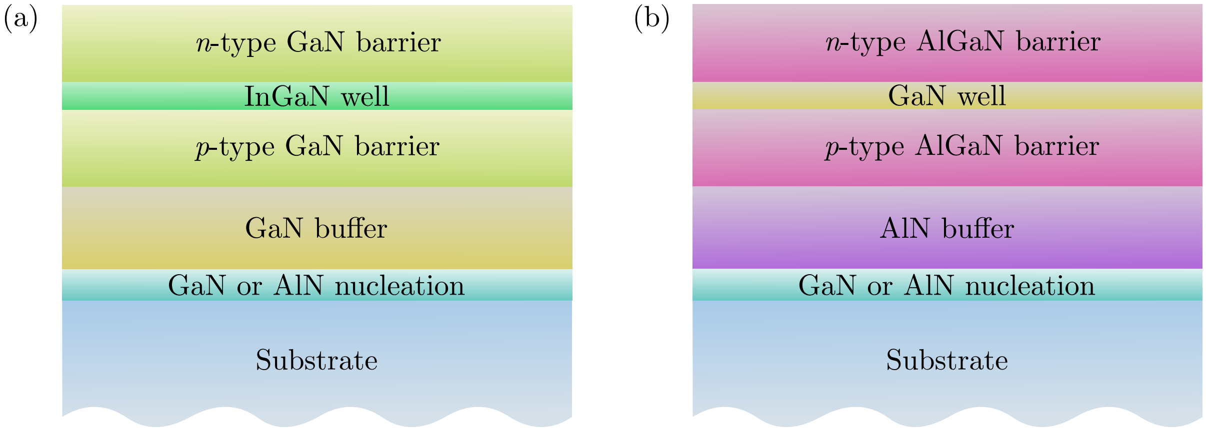

Fig. 2.13. Quantum well structure used for light emitters using the (a) GaN/InGaN and (b) AlGaN/GaN systems. Adapted from [84, 85].

2.3.4 Zincblende nitrides in light emitters

The results of polarization effects are more notorious in light emitters than they are in power electronics. The strong electric fields generated at AlGaN/GaN and GaN/InGaN junctions bend the electronic bands even before applying a bias. For example, these electric fields can have magnitudes of a few MV/cm for a QW with well width of 10 nm and composition up to 30 % In in a GaN/InGaN/GaN structure.

There are two main consequences of band bending due to electric fields. First, the emission

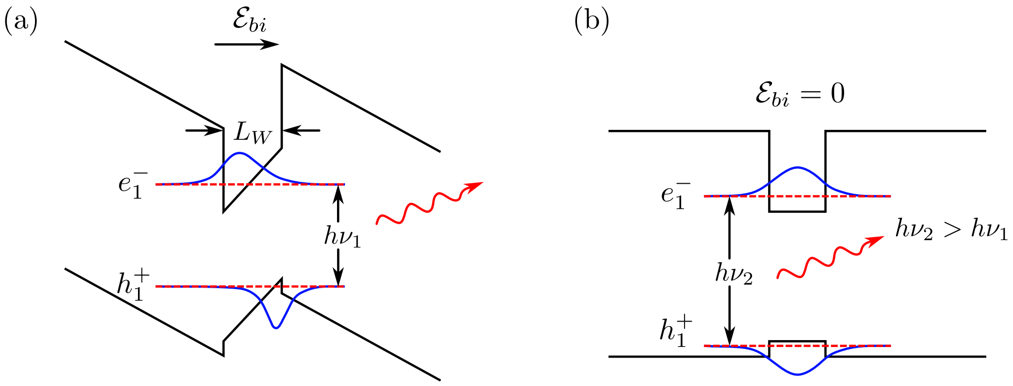

Fig. 2.14. Band structure of a QW (a) with and (b) without polarization. Adapted from [86].

undergoes a red shift due to the reduction of the transition energy between the first electron and the first hole levels. This phenomenon is referred to as quantum confined Stark effect (QCSE) and is somewhat screened when forward bias is applied, leading to a blue shift [82]. **Fig. 2.14** shows a schematic representation of the band bending due to the built-in electric field $\mathcal{E}_{bi}$ and the caused red shift ($h\nu_2 > h\nu_1$) of the emission due to the transition between the first allowed states in the conduction e_1^- and valence h_1^+ bands QW.

The emission energy considering the QCSE writes [87]

$$h\nu = E_{g,\text{well}} + e_1^- + h_1^+ - q\mathcal{E}_{bi}L_W, \tag{2.33}$$

where the term $q\mathcal{E}_{bi}L_W$ accounts for the red shift. For a thin well ($L_W < 2$ nm) the effect is relatively weak; however, for thicker wells, the emission energy $h\nu$ is potentially smaller than the bandgap of the bulk material that constitutes the well [82].

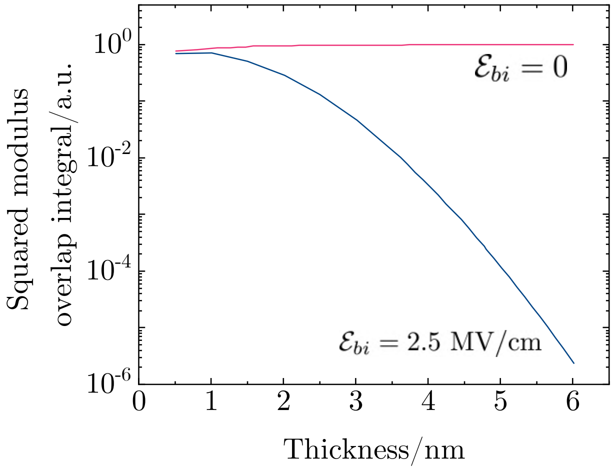

Fig. 2.15. Evolution of the squared modulus of the overlap integral with well thickness with and without built-in electric field for an InGaN/GaN QW with 17 % In content. Data from [87].

Furthermore, because the radiative recombination rate R_r depends on the overlap of the envelopes of the electron and hole wavefunctions f_e and f_h [87]

$$R_r \propto \left| \int f_e(z) f_h(z) dz \right|^2 , \tag{2.34}$$

when electrons and holes are pushed onto opposite sides of the well by the band structure bending, non-radiative recombination processes gain the upper-hand and light emission efficiency drastically decreases.

Although the effects of polarization can mitigated to a certain degree, complicated solutions such as limiting well thickness (**Fig. 2.15**), growing on semipolar $(11\bar{2}2)$ or nonpolar $(11\bar{2}0)/(10\bar{1}0)$ planes [14], or producing polarization-matched AlInGaN/GaN structures [11]. Once again, the zincblende phase offers a naturally polarization-free—see **Eq. (2.5b)**—alternative, where common (001) growth directions can be utilized for simple heterojunction device fabrication, as the shown in previous sections.

Chapter 3: State-of-the-Art Epitaxy of Nitride Semiconductors

The growth of nitrides for their use in optoelectronic devices is commonly carried out by epitaxial (from the Greek $\varepsilon\pi\iota$: epi, upon, attached to; and $\tau\alpha\xi\iota\sigma$: taxis, arrangement, order [88]) techniques such molecular beam epitaxy (MBE) or metalorganic vapour phase epitaxy. In that sense, epitaxial growth denotes the crystallization of atoms, or molecules, resulting in a new phase (epilayer) whose orientation and crystalline structure is reliant on the substrate on which it is being grown.

The epitaxial growth process is influenced by numerous factors, including the substrate type, temperature, adhesion energy, and flux rates of the nitrogen and metal sources. Depending on these factors, four main growth modes have been identified in epitaxial growth, namely Frank-van der Merwe (FM), step flow, Stranski-Krastanov (SK), and Volmer-Weber (VW).

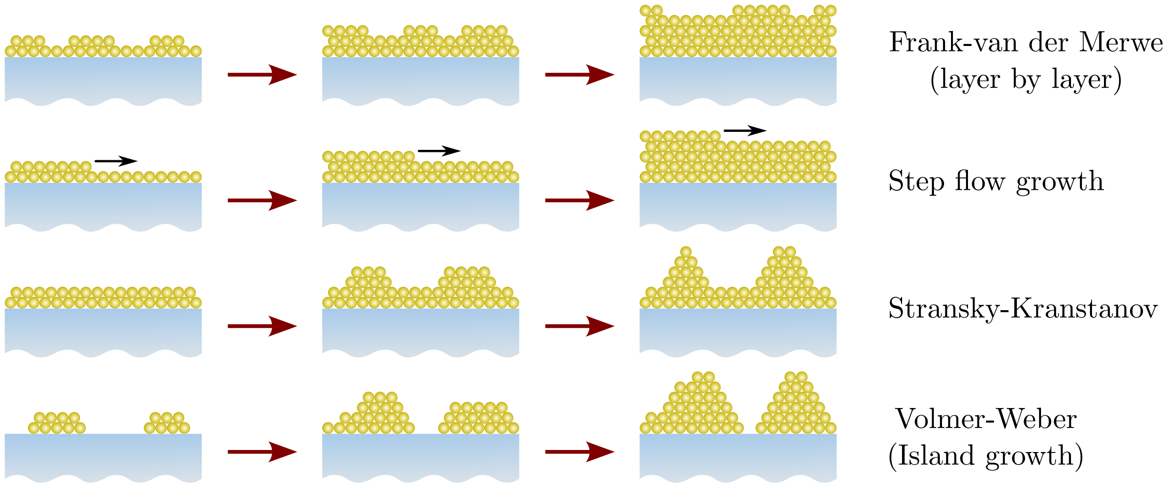

Fig. 3.1. Growth modes in epitaxy. Adapted from [89].

First, in the FM mode, the adatoms (atoms of the growing crystal) start nucleating at various points over the substrate surface forming monolayer-thick islands. If adatom mobility is sufficiently large, they are allowed to reach the edges of such nucleation points, making these islands grow until they meet each other and coalesce. This results continuous layer-by-layer growth. On a surface that is not a perfect facet, a related growth mode can be described. Due to the misorientation from perfect atomic planes, ledges, or steps, naturally occur. In the so-called step-flow mode, atoms arriving at the growth front diffuse to the energetically-favored steps, producing a very smooth surface. In both cases, the interactions adatom-substrate is stronger than those of adatom-adatom [89].

Conversely, the VW mode takes place when the atoms of the growing film are strongly bound to each other, therefore not completely wetting the substrate's surface, leading to the formation of 3D islands [90]. These islands can coalesce to form a continuous layer, but their 3D nature can result in strain and defects within the film. Finally, the SK mode can be considered as a combination of the FM and VW growth modes. During the first stages, the incoming atoms distribute uniformly on the surface, generating a layer-by-layer growth. If the lattice mismatch between epilayer and substrate is large enough, stress accumulates as the film grows, until a critical point is reached and lattice relaxation occurs. At this point, there is a transition to island growth [91]. A schematic representation of the three modes during different stages of the growth is shown in **Fig. 3.1**.

Using any of the three modes can have significant implications for the properties and applications of the resulting epitaxial crystals. For instance, the SK mode can be used to produce quantum dots [92, 93], whereas, the FM mode is preferred for high-quality thin films that are suitable for the fabrication of quantum wells [94]. The VW mode, on the other hand, may be desired to produce nanowires [95].

3.1 Molecular beam epitaxy generalities

As mentioned above, one of the two main techniques to achieve epitaxial growth of nitride semiconductors is MBE, a versatile growth technique used to produce a variety of materials entailing semiconductors, metals, and insulators [96]. There are a few reasons as to why MBE stands out as a method for growing advanced epitaxial structures. To illustrate, MBE provides a fine control over thickness, composition, and doping, allowing for high-quality, ultra-sharp interfaces needed for low-dimensional structures [97].

There are a few fundamental factors allow MBE to produce such high quality materials, namely the ultra-high vacuum (UHV) chambers, high-quality effusion cells, precise shutter control it uses. Moreover, characterization techniques such as reflection high-energy electron diffraction (RHEED) can be easily integrated to control the growth process in-situ.

First, the UHV conditions are required to prevent the contamination of the produced semiconductor films. Theoretical estimations indicate that a typical background pressure of 10^{-10} Torr within an MBE system yields an incorporation of about 5×10^{17} cm^{-3} foreign atoms. Yet, the impurity levels observed in epitaxial layers grown under these conditions are significantly lower than these predictions [98]. Moreover, the UHV environment ensures that the mass transport from the sources maintains its beam nature, meaning there is no scattering between the source species with residual gas molecules [99].

3.1.1 Growth setup

In order to accomplish such conditions, a standard MBE setup comprises three stainless steel chambers employing various combinations of turbomolecular, diffusion, cryogenic, and ion pumps. The incorporation of Ti sublimation pumps is also often utilized. All that pumping is supplemented with an efficient baking out system [100] as well as a cryo-shroud cooled with liquid nitrogen in the main chamber [99], resulting in the UHV environment needed.

The first chamber, referred to as load lock, acts as an interface between the UHV conditions within the MBE setup and the ambient conditions outside. Through it, fresh substrates are introduced and grown structures extracted. Usually, the primary degassing of the substrates is also carried out there. Right after the load lock, a buffer chamber is used before the main chamber in order to keep the latter as clean as possible. This second chamber is sometimes called analysis chamber as it can accommodate surface characterization techniques, such as x-ray photoelectron spectroscopy or Auger electron spectroscopy.

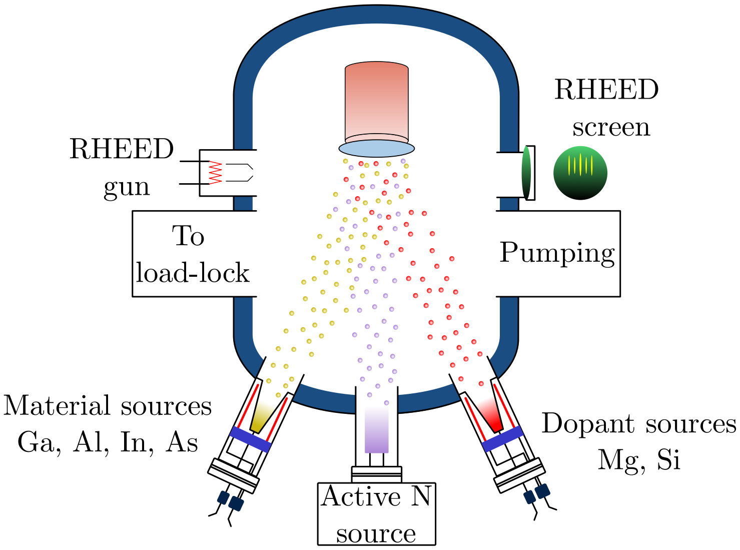

Fig. 3.2. MBE schematic representation. Adapted from [101].

The main chamber, also growth chamber, contains all the material sources, along with their shutters, observation ports, in-situ characterization techniques, and the substrate holder with a heater. Here, the sources are heated to produce atomic, or molecular, beams that are directed towards the substrate. The beams then condense on the substrate to form crystalline layers, resulting in the growth of a new material or structure.

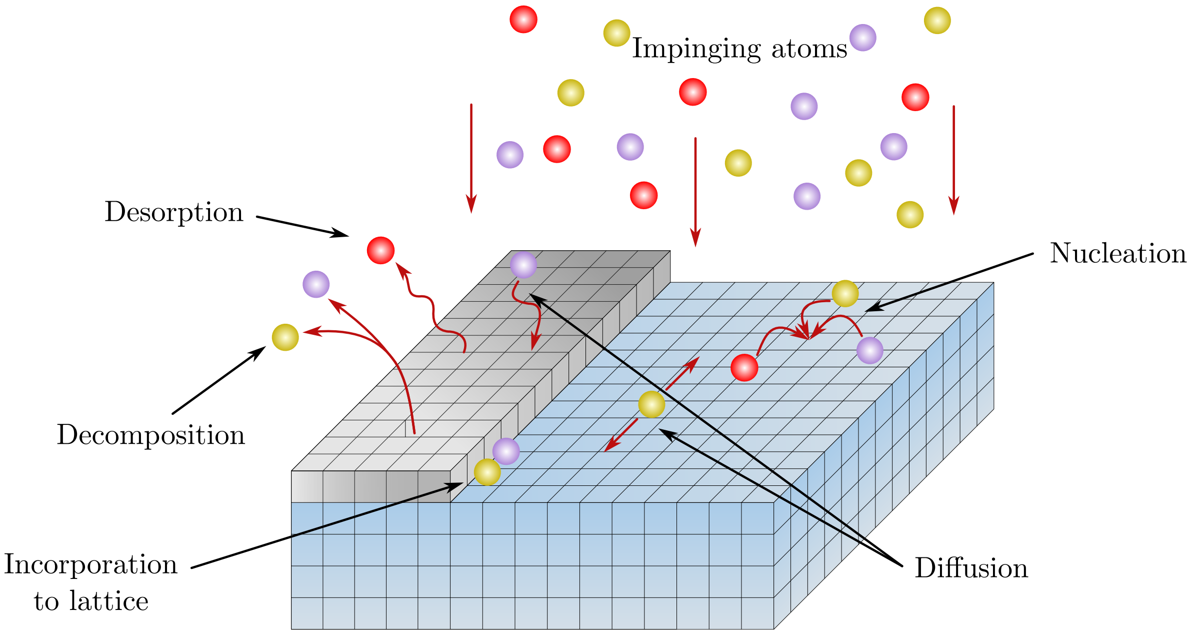

Fig. 3.3. Surfaces mechanisms happening in MBE. Adapted from [102].

Effusion cells are the responsible for providing the atomic/molecular beams. For condensed sources, e.g., Ga, Al, In, and As, a modified Knudsen cell (larger openings than the ideal), consisting of a crucible surrounded by an electrical oven, is used to heat up the source material and vaporize it in order to produce the beam. Depending on the specifics of other needed materials, different types of cells may be used. For example, the evaporation of refractory materials or metal oxides require unconventionally high temperatures. In such cases, an electron beam focused on the material surface is often used for the production of the beam [100].

Upon impinging on the heated substrate surface, materials from the sources can undergo different processes. Most importantly, they can chemically react to incorporate into the growing crystal, adsorb back to the growth chamber, or segregate before reacting or desorbing [103]. Moreover, if temperature is sufficiently high, bonds may break crystal and atoms can leave the crystal lattice. Such mechanisms are depicted schematically in **Fig. 3.3**.

3.1.2 In-situ characterization by RHEED

As mentioned earlier, one of the advantages of growing films under UHV conditions in MBE is its compatibility with various characterization techniques, including RHEED, enabling a certain level of real-time control over film growth. In a RHEED setup, electrons from an electron-gun diffract from the sample surface at grazing angles (1 to 3° [103]), producing a diffraction pattern on a phosphor screen in front. For a more detailed description on diffraction geometry, the reader is referred to **Section 4.1**.

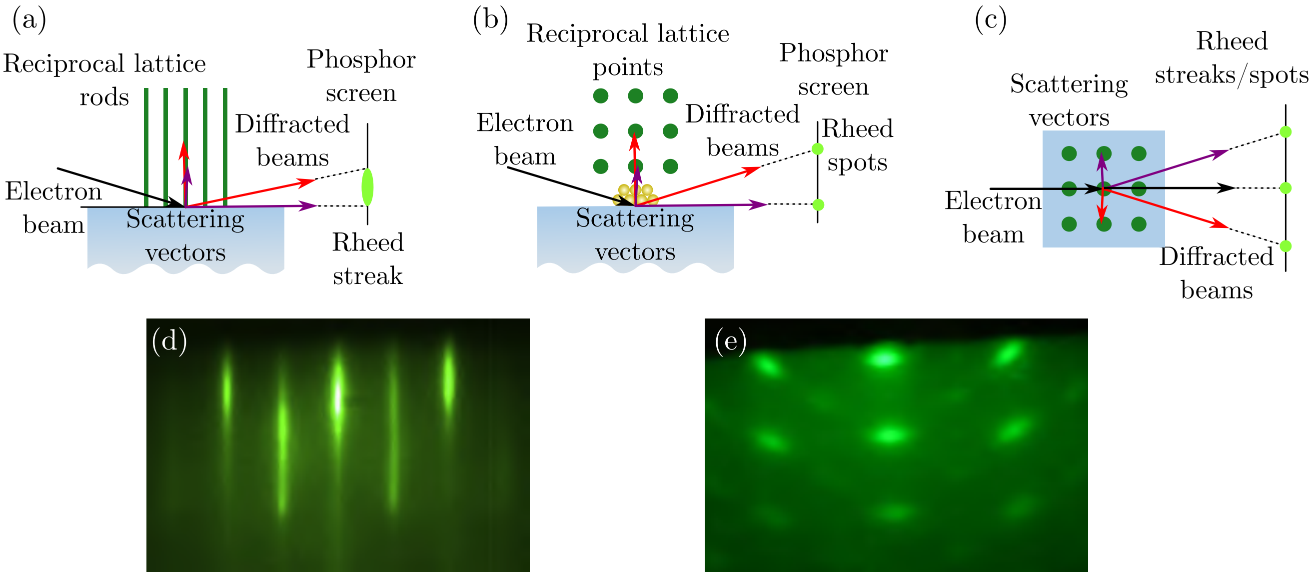

Fig. 3.4. RHEED geometry (a) for a flat surface with reciprocal rods [103] and (b) a rough surface with reciprocal points [104]. A top view is shown in (c) [103]. Experimental patterns from (d) a flat [103] and (e) rough [105] surfaces reprinted with permission of Elsevier.

Because of the grazing angle, RHEED is a highly surface-sensitive technique, allowing for the direct observation of the growth mode as the process takes place. For example, in the case of layer-by-layer growth, the resulting flat surface gives rise to rods perpendicular to the surface in reciprocal space, as only a few atomic layers participate in diffraction. However, due to the spread in electron energy, atomic vibrations, and the relatively large size of the scattering vector compared to the interplanar distance, the resulting diffraction pattern manifests as a collection of vertically elongated *streaks*. Conversely, during island growth mode, RHEED electrons undergo transmission, resulting in a distinctive *spotty* pattern that is characteristic of atomic-scale roughening [104]. **Fig. 3.4** illustrates the RHEED geometry from side and top views, showcasing a measured streaky and spotty pattern.

Moreover, the presence of dangling bonds on the surface of a material leads atoms to rearrange, or *reconstruct*, in order to reduce the surface energy [106]. This process generates a new mesh different from the bulk that depends on various factors such as crystalline orientation, temperature and flux of incoming atoms to the surface [103]. The new mesh, in turn, generates its own reciprocal space and is, consequently, observed in a RHEED pattern. Identifying a specific reconstruction (e.g. GaAs (hkl) $(n_R \times m_R)$ where hkl indicates the surface orientation with a reconstructed primitive cell n_R and m_R times larger than the bulk along x and y, respectively [106]), allows for the description of certain properties of the growing film. For instance, the

(2×4) reconstruction in GaAs suggests high-quality, layer-by-layer growth [107], whereas the (3×3) reconstruction in AlN indicates N-polarity [108].

Finally, the evolution of the electron beam intensity as a function of time from various diffraction features is routinely used to measure growth rate, alloy composition, migration rates, and growth kinetics [103]. This is mainly because RHEED intensity is heavily dependent on the growth stage. Illustratively, a few steps can be observed during the growth of each monolayer. Initially, as the new film begins to crystallize, multiple nucleation centers appear, which act as scattering points. Thus, RHEED intensity decreases during the first half of the monolayer, which corresponds to the point of maximum disorder and, therefore, minimum intensity. As the islands coalesce, scattering gradually decreases and the long-range order rises. As a result, RHEED intensity progressively surges until it reaches its initial value, completing one cycle of 1 monolayer equivalent to one RHEED oscillation.

3.2 Growth of nitrides by MBE

3.2.1 Plasma-assisted MBE

For the growth of nitride semiconductors, the supply of N is rather complex because of the chemical stability of N_2 molecules derived from the highly-energetic triple bond between the N atoms. This renders the use of N_2 as a gas source unfeasible; instead, nitrogen can be supplied in the form of NH_3 (ammonia) or N plasma. In the case of the former, the usually-high temperatures used to growth AlGaN (∼750–800 °C) provides sufficient energy to break the NH_3 molecule, releasing H and allowing the N atoms to react with the adsorbed metals on the substrate surface. For lower the lower temperatures (∼600 °C) required for InGaN, however, it is sometimes not enough to do this process efficiently, so that increasing NH_3 flow becomes imperative [99].

Alternatively, a radio-frequency (RF) plasma source can used to crack the inactive N_2 into active species, entailing atomic and molecular ground and excited states (N, N^*, and ${N_2}^*$) as well as ionic (N^+ and ${N_2}^+$) and other short-lived species [102, 109]. Because of their high energy, ions and electrons generated in the plasma are prone to damaging the growing films; therefore, current RF sources include ion deflectors to deflect these charged species away from the substrate [99]. When a RF plasma source is employed, the technique is referred to as plasma-assisted MBE (PAMBE).

3.2.2 PAMBE growth of nitrides

The growth of nitride semiconductors is influenced by two crucial parameters: stoichiometry, which refers to the metal/N ratio, and substrate temperature. These parameters determine the growth regime, which can be categorized into three main regimes: N-rich, Ga-rich, and Ga-droplets. The structural, morphological, and optoelectronic properties of the resulting crystals are highly sensitive to the specific growth regime, and extensive discussions have taken place regarding this relationship for both wurtzite and zincblende nitrides.

Although the growth kinetics of these relations are not completely understood, there is a general consensus that reason for the profound effects of these two growth parameters on film properties are due to the changes in Ga adatom mobility, since mobility of active N species is already hindered by its high activation energy (four times that of Ga) [102]. Consider the changing growth conditions described by the vertical arrow in **Fig. 3.5(a)**, where the three growth regimes are depicted as function of substrate temperature and Ga flux for wurtzite GaN. On the lower end, the small Ga flux leads to N-rich conditions (Ga/N < 1). In this environment, the large amount of highly reactive N species on the growth front causes incoming Ga atoms to react before having time to reach an energetically favorable position, favoring the nucleation of stacking faults and islands [102]. Consequently, 3D growth takes place, producing crystals with a surface characterized by a high density of pits, as shown in **Fig. 3.5(b)**.

As Ga flux increases and the conditions are changed to only slight N-rich conditions (dependent on temperature), this effect diminishes. Moreover, further up into the intermediate regime, the reduction of readily available N active species allows Ga adatoms to be highly mobile and diffuse to more energetically favored positions. This results in 2D growth taking place with the subsequent planarization of the surface (**Fig. 3.5(c)**) and reduction of stacking faults and point defects [102]. Nevertheless, if Ga flux is still not sufficiently high, there is still the appearance of pits, albeit with lower density than under N-rich conditions.

Additionally, the formation of a Ga wetting layer has been widely described [110–112]. Generally, the highest crystalline qualities and flatters surfaces have been obtained with Ga coverage up to 2.5 monolayers. However, if the excess Ga is not thermally desorbed back from the surface, e.g. when the Ga flux is too high, Ga accumulates to produce metallic droplets on the surface, which is detrimental to the film quality [112–114]. **Fig. 3.5(d)** and **Fig. 3.5(f)** show a side and top view of a surface obtained from a GaN film grown by PAMBE under Ga-droplet regime, where a surface with Ga droplets and no pits is observed.

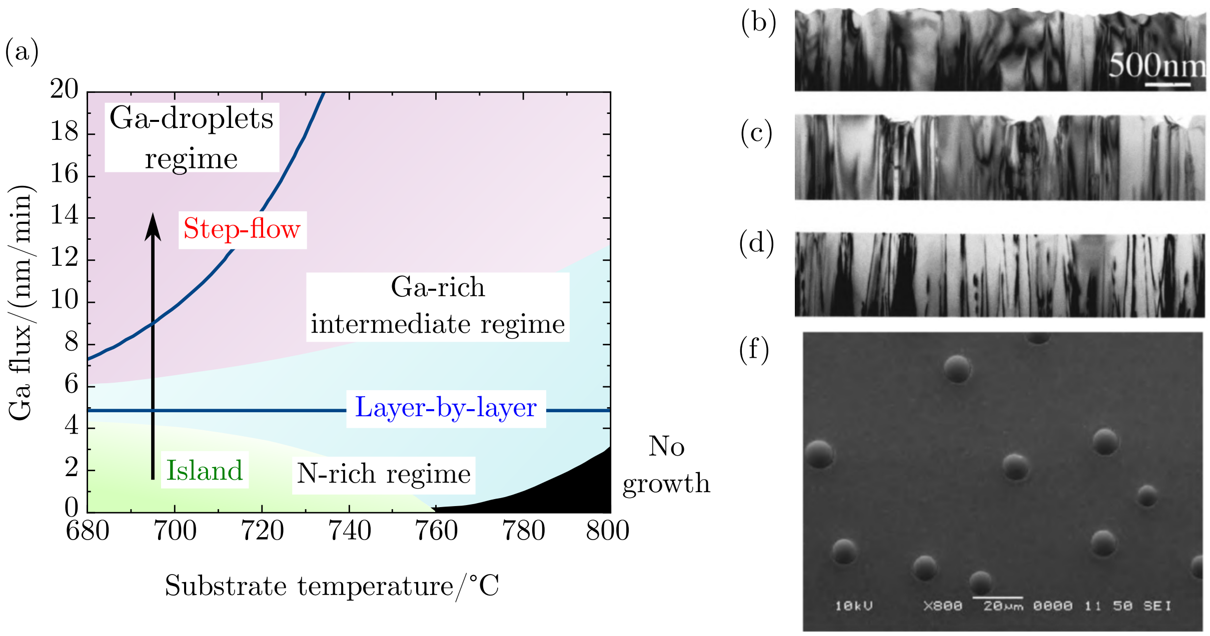

Fig. 3.5. (a) stoichiometric regimes for the growth of wurtzite GaN by PAMBE [110]. Colors indicate different growth modes found in the three regimes, which are separated by blue curves. Cross section SEM micrographs of GaN grown in (b) N-rich, (c) intermediate, and (d) Ga-droplets regimes. SEM from the surface of a GaN film grown in the Ga-droplets regime. (b)-(d) reprinted from [111] with permission from AIP Publishing. (f) reprinted from [102] with permission from John Wiley and Sons.

3.2.3 PAMBE growth of zincblende nitrides

It can then be argued that the best wurtizte thin films, in terms of crystalline structure and morphology, are grown under metal-rich regime near the onset of droplet formation. Although a detailed diagram such as the shown in **Fig. 3.5(a)** has not been reported for the zincblende polytypes, it is a widespread agreement that the metal-rich conditions yield the best results for this phase as well [26, 28, 115–117].

At and below standard pressure conditions, the zincblende polymorph is a metastable phase due to its slightly higher internal energy compared to the wurtzite structure [18, 22]. Hence, one of the main problems hindering the development of zincblende devices is the high amounts of wurtzite inclusions and derived lower crystalline quality due to phase transitions toward the more stable phase.

As discussed in the previous section, N-rich condition heavily limit Ga mobility, leading to nucleation centers in energetically unfavorable positions, causing, among other defects, stacking faults. Recalling from **Fig. 2.2** that the main difference between the two structures is their stacking sequence, it is clear that the stoichiometry during growth plays a very important role. In that sense, N-rich conditions generally induce the normal zincblende ABCABCABCABC stacking sequence to change to wurtzite's ABCAB***A***BABA or twined zincblende's ABCAB***A***CBACB, where the stacking faults are indicated in italicized, bold letters.

Moreover, this problem is exacerbated by the lack of native substrates available for the zincblende phase. A wide range of results have been reported for the growth of zincblende nitrides mainly on GaAs [29–31], 3C-SiC [26–28, 115], MgO [24, 25, 116]. Because of the lattice mismatch (**Table 3.1**), the nitride epilayer strains and takes the parameters of these substrates [118]. When a *critical thickness* is reached, the accumulated stress is enough so that the strained atoms start relaxing to their natural lattice parameters (as schematically shown in **Fig. 3.6**), leading to the so called *misfit* dislocations.

Table 3.1. Lattice parameters of common substrates used for the growth of zinclbende nitrides and their mismatch calculated with **Eq. (2.14)** with a_s and a_r the lattice parameters of the substrate and relaxed epilayer, respectively. Lattice parameters for nitrides are taken from **Table 2.1**.

Substrate	Space group	a/Å	Lattice mismatch/% GaN	AlN	InN
GaAs [47]	F$\bar{4}$3m	5.653	25.54	29.30	13.97
3C-SiC [119]	F$\bar{4}$3m	4.350	-3.40	-0.50	-12.30
MgO [23]	Fm$\bar{3}m$	4.251	-5.60	-2.77	-14.29

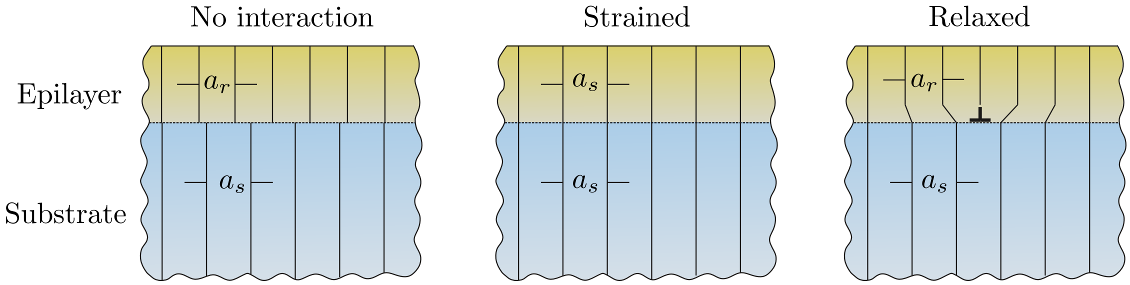

Fig. 3.6. Dislocations generated due to relaxation of strained films. Adapted from [118].

In order to alleviate this problem, it is a common practice to first prepare a nucleation layer with different parameters than the main growth. Aimed to mitigate relaxation effects, a nucleation layer can have a significant influence on the subsequent growth. For instance, Yang et al. [19] showed that, during the first stages of GaN growth on GaAs (001), it is preferable to have several small nucleation centers instead of a few big ones achieved by a small Ga/N ratio. According to them, the dislocations from one nucleation center annihilate with the dislocations from another. Once few monolayers have been established, the growth takes place with the usual parameters. In addition to that, Casallas-Moreno et al. [31] argued that maintaining an

As_4 overpressure during the first few monolayers aids in the control of relaxation, preventing wurtzite inclusions that would otherwise propagate. They also showed that different polarities yield different amounts of defects, with the Ga-polar directions [111] and $[\bar{1}\bar{1}1]$ being more prone to defects than their N-polar $[\bar{1}11]$ and $[1\bar{1}1]$ counterparts.

Moreover, similar results have been demonstrated for MgO and 3C-SiC. For example, Kakuda et al. [24] reported an increased phase purity of zincblende AlN on MgO (001) by using a low-temperature GaN nucleation layer. Conversely, Zscherp et al. [28] demonstrated improved roughness of zincblende GaN films on 3C-SiC (001) with the addition of a thin AlN nucleation layer to gradually reduce lattice mismatch.

Chapter 4: Diffraction from Nitride Semiconductors

4.1 X-ray diffraction

4.1.1 General description

Ever since their discovery by Wilhelm Conrad Röntgen in 1895 [120], which awarded him the very first Nobel prize in physics in 1901 [121], x-rays have been widely used in different areas of science. In materials sciences, x-ray diffraction (XRD) is a common technique to assess the crystalline structure of materials [122]. It involves probing the crystal with light whose wavelength is close to the crystal's lattice spacing [123], i.e., by x-ray generated by bombarding a metal with electrons in an evacuated tube. In a simplified way, the electric field of the x-ray primary beam impinging on the crystal exerts forces in the electrons of the crystal. Such forces accelerate the affected electrons and, following classical electromagnetic theory, they act as new radial sources of light whose wavelength is the same as the primary beam and is called *scattered radiation*. Although experimental results demonstrate that some of the scattered radiation has larger wavelength, this approach is sufficient to explain the most XRD techniques [124].

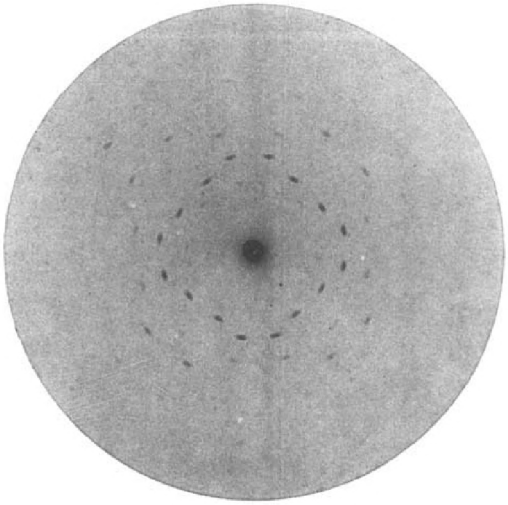

Fig. 4.1. Diffraction pattern found by W. Friedrich, P. Knipping, and M. Laue [125] from cubic ZnS. Reprinted with permission from John Wiley and Sons.

Since electrons from multiple atoms in the irradiated crystal are acting as sources of scattered radiation, a *diffraction pattern* is produced due to the interference between the the different sources. Such effect was first observed by Walter Friedrich, Paul Knipping, and Max von Laue in 1912; **Fig. 4.1** shows one of the first XRD patterns ever recorded from a face-centered cubic ZnS crystal [125]. This observation, and subsequent description by Laue [126], rendered him the Nobel prize in physics in 1914 [127].

4.1.2 Bragg's law

A year later, in 1915, William Lawrence Bragg, proposed the, nowadays famous, mathematical model describing the geometry of diffraction by crystals [128], which ultimately led him to win the physics Nobel prize that year along with his father, William Henry Bragg [129]. Consider the model in **Fig. 4.2**, representing three sets of planes with interplanar distance d_{hkl}. Four incoming x-ray beams are also represented impinging on two atoms in the first plane and an atom on each of the two remaining planes. Additionally, the first two planes form a rectangular grid, while atoms on the third plane are offset in the horizontal direction, to represent the most simple case and a general one.

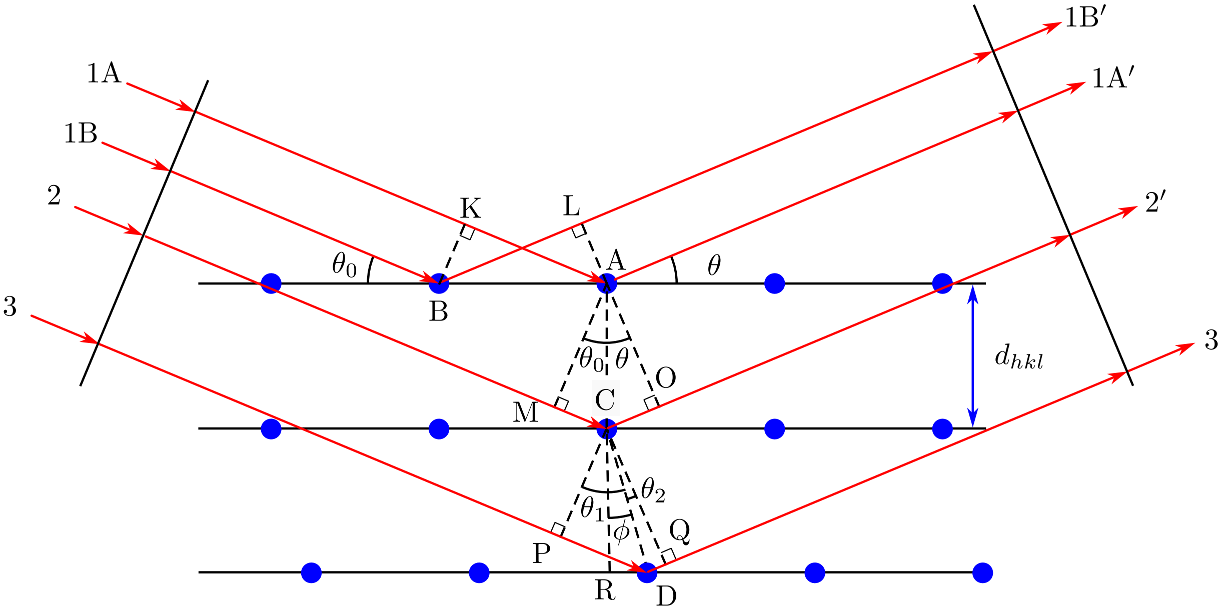

Fig. 4.2. Geometry of Bragg's law. Adapted from [130, 131].

Beams 1A and 1B, striking with angle θ_0 on lattice points A and B and scattered in every direction, produce constructive interference only at angles θ where the path difference AK − BL is an integer multiple of incident beam's wavelength A′. In Bragg's description, the 0th-order diffraction is considered, for which the incoming and diffracted beams' paths are equal. This leaves [130]

$$\mathrm{AK} - \mathrm{BL} = \mathrm{AB}\cos\theta_0 - \mathrm{AB}\cos\theta = 0, \tag{4.1}$$

from which it follows that

$$\theta_0 = \theta. \tag{4.2}$$

In other words, constructive interference occurs at specular angles, with incidence angle equalling diffracted angle. For this reason, in crystallographic jargon, XRD signals area usually called *reflections*. Note that care must be taken, for the effect taking place is diffraction instead of reflection.

Now consider the path difference between incoming beams 1A and 2, inciding on lattice positions A and C. Once more, in order for constructive interference to occur, the path difference CM + CO must equals an integer multiple of the beam's wavelength.

$$\mathrm{CM} + \mathrm{CO} = n\lambda. \tag{4.3}$$

Considering specular diffraction, from **Eq. (4.2)**, CM=CO= $d_{hkl}\sin\theta$, were d_{hkl} is the interplanar distance for planes with Miller indices hkl, the following equation, known as Bragg's law, is finally derived

$$2d_{hkl}\sin\theta = n\lambda. \tag{4.4}$$

Finally, consider the last case, where atoms do not form a rectangular grid. The path differences between incident beams 2 and 3 on lattice points C and D is DP + DQ so that constructive interference occurs when [131]

$$\mathrm{DP} + \mathrm{DQ} = \mathrm{CD}(\sin\theta_1 + \sin\theta_2) = n\lambda. \tag{4.5}$$

With $\theta_1 = \theta + \phi$ the angle between CP and CD, $\theta_2 = \theta - \phi$ the angle between CD and CQ (considering again **Eq. (4.2)**), ϕ the angle between CR and CD, all three as shown in **Fig. 4.2**. Using the identity $\sin(A + B) = \sin A\cos B + \cos A\sin B$

$$\mathrm{DP} + \mathrm{DQ} = \mathrm{CD}(\sin\theta\cos\phi + \cos\theta\sin\phi + \sin\theta\cos\phi - \cos\theta\sin\phi) = 2\mathrm{CD}(\sin\theta\cos\phi). \tag{4.6}$$

With $\mathrm{CD}\cos\phi = d_{hkl}$, this once more yields

$$\mathrm{DP} + \mathrm{DQ} = 2d_{hkl}\sin\theta = n\lambda \tag{4.7}$$

for constructive interference. This means that Bragg's law fulfills irrespective of the atomic positions within a plane as long as the interplanar distance and diffraction angle are appropriate.

In some cases, it is convenient to incorporate the order of diffraction n into the interplanar distance such that $d_{hkl}/n = d_{nh,nk,nl}$, where nh, nk, and nl are the so-called Laue indices (or reflection indices) and often written just hkl without the factor n [132]. With that, the final form of Bragg's law is then

$$2d_{hkl}\sin\theta = \lambda. \tag{4.8}$$

Although deceptively simple, Bragg's law is one of the most important equations in crystallography. It allows for the interpretation of most x-ray diffractograms, especially when in vector form.

Vector form of Bragg's law

Bragg's law in **Eq. (4.8)** describes the geometric condition for constructive interference to occur in terms of the interplanar distance and the diffraction angle. It can also be expressed using vector notation. Let $\boldsymbol{s_0}$ and $\boldsymbol{s}$ be unit vectors along the directions of the incident and diffracted beams, as depicted in **Fig. 4.3**. Due to the incident and diffracted angles being the same, the vector $(\boldsymbol{s} - \boldsymbol{s_0})$ is normal to the diffracting planes, and therefore, parallel to $\boldsymbol{H_{hkl}}$ (see **Eq. (A.2)** in **Appendix A**).

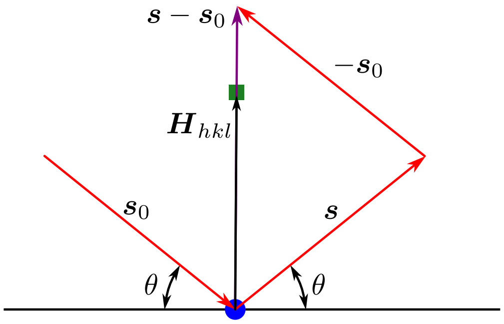

Fig. 4.3. Geometry of diffraction in vector notation. Adapted from [128].

With the moduli of both vectors ($|\boldsymbol{s} - \boldsymbol{s}_0| = 2\sin\theta$ and $|\boldsymbol{H_{hkl}}| = 1/d_{hkl}$) and **Eq. (4.8)**, the ratio between the two vectors is

$$\frac{|\boldsymbol{s} - \boldsymbol{s}_0|}{|\boldsymbol{H_{hkl}}|} = 2d_{hkl}\sin\theta = \lambda. \tag{4.9}$$

Defining $\boldsymbol{k} = \boldsymbol{s}/\lambda$ and $\boldsymbol{k_0} = \boldsymbol{s_0}/\lambda$ while rearranging yields

$$\boldsymbol{Q} = \boldsymbol{k} - \boldsymbol{k_0} = \boldsymbol{H_{hkl}}, \tag{4.10}$$

which is Bragg's law written in vector notation, where $\boldsymbol{Q}$ is the so-called *scattering vector*. **Eq. (4.10)** illustrates diffraction in the context of the reciprocal lattice. It conveys that constructive interference, and therefore an XRD signal, occurs if $\boldsymbol{Q}$ coincides with a reciprocal space point, which is defined by $\boldsymbol{H_{hkl}}$.

4.1.3 X-ray diffraction geometry

In order to probe the reciprocal space, an x-ray source, detector, and sample are rotated about different angles. A typical diffractometer is shown schematically in **Fig. 4.4**. The sample is placed so that its surface coincides with the center of the so-called *diffractometer circle*. Typical x-ray sources employed in XRD are Cr, Fe, Co, Cu, and Mo with wavelengths as shown in **Table 4.1**. As for beam conditioning, different optics can be used. On the incident side, for high-resolution XRD used in epitaxial films, a parabolic bent multilayer mirror is first used to produce a nearly parallel beam (divergence of about 0.003° [123]). Then, a monochromator is used to eliminate $K\beta$ and $K\alpha_2$. Typically 2- or 4-bounce Si or Ge crystals are employed for this purpose. With an open detector, this is called a *double-axis* diffractometer. If a crystal analyser is further added on the receiving side, the system is called a *triple-axis* diffractometer.

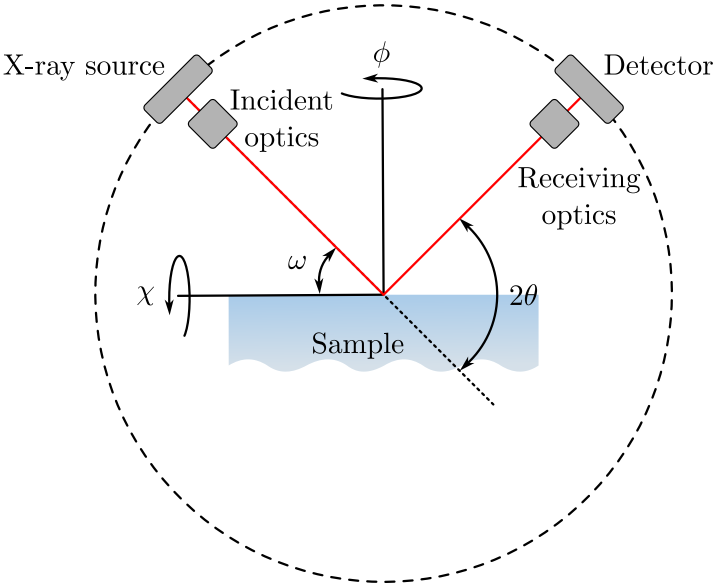

Fig. 4.4. X-ray diffractometer axes.

Table 4.1. Commonly employed X-ray sources and their emission in nm. Data from [133].

	$K\alpha_1$	$K\alpha_2$	$K\beta$
Cr	2.289700	2.293606	2.084870
Fe	1.936042	1.939980	1.756610
Co	1.788965	1.792850	1 .620790
Cu	1.540562	1.544390	1.392218
Mo	0.709300	0.713590	0.632288

4.2 Scan types

In the most general case, the variable controlling the length of $\boldsymbol{Q}$ is the angle between the diffracted beam and the projection of the incident beam 2θ, while its direction is given by the angle between the incident beam and the sample's surface ω.

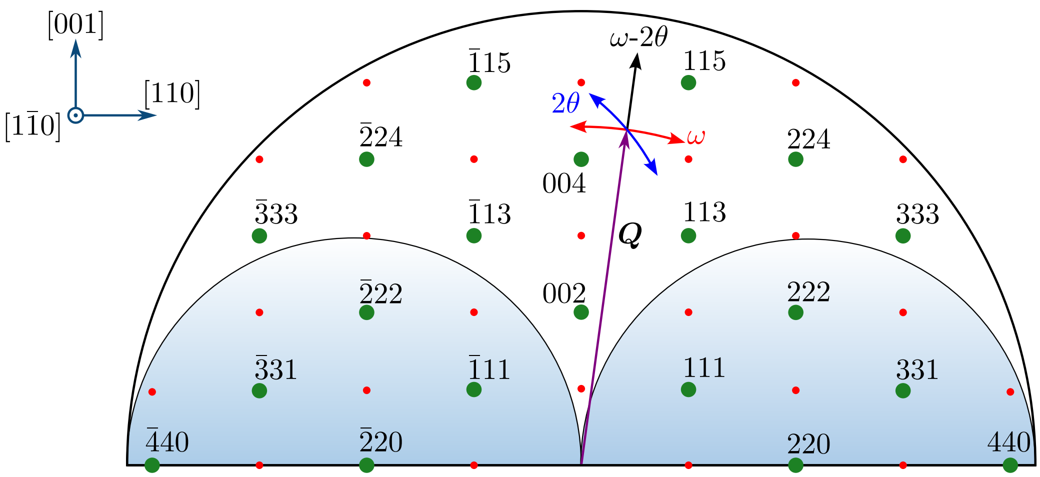

Fig. 4.5. Zincblende-GaN reciprocal space map available in XRD using Cu as an X-ray source. The shaded areas shows the part of space that is inaccessible in reflection mode. Red dots indicate forbidden reflections due to the structure factor of GaN—**Eq. (4.15)**.

The most common measurements used for the III-N epitaxial films are based on probing the reciprocal space by scanning either ω and 2θ in a coupled manner (ω-2θ scan), only ω (ω scan), and combination of both (reciprocal space maps). **Fig. 4.5** shows how the two types of scan (as well as the so called 2θ scan, not common for epitaxial thin films) affect the length and direction of the scattering vector $\boldsymbol{Q}$.

Moreover, χ sets the inclination of the sample with respect to the direction normal to the page, and ϕ the rotation around the vertical direction. By fixing ω and 2θ and couple scanning χ and ϕ, a pole figure is produced.

4.2.1 Coupled ω-2θ scan

Also known as radial scan, an ω-2θ entails rotating the incident beam and detector simultaneously at the same speed, effectively changing one ω step for every two steps in 2θ. With this, the changing length of $\boldsymbol{Q}$ scans radially the reciprocal space as shown in **Fig. 4.6**. A coupled scan reveals the presence of grains of a given phase, their orientation and lattice spacing [134]. More specifically, with the help of **Eq. (4.8)**, the interplanar distance can be calculated from any reciprocal-lattice point measured with an X-ray diffractometer if a signal appears at a given θ.

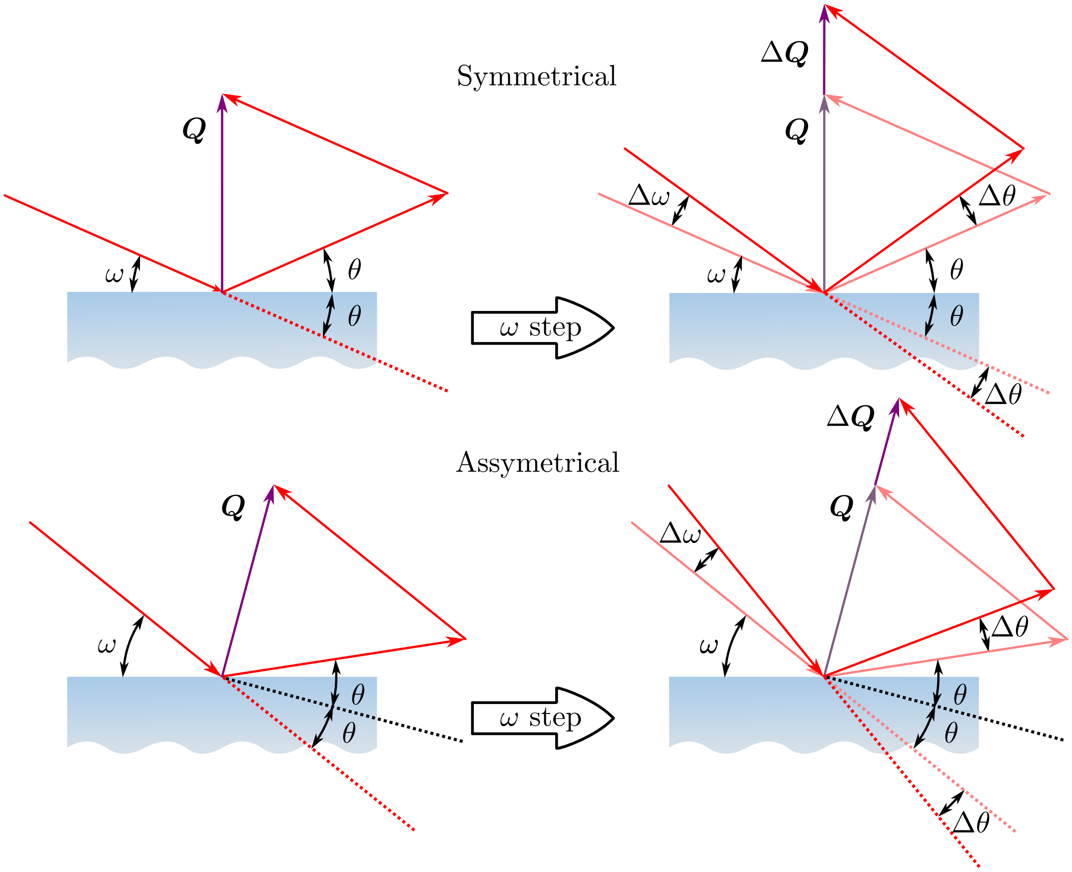

Fig. 4.6. ω-2θ scan geometry showing symmetrical and asymmetrical scans before and after an ω step.

Furthermore, the lattice parameters can be calculated from the interplanar distance, provided that the indices of the measured reflection are known. For example, for wurtzite ($\alpha = \beta = 90$, $\gamma = 120$, and $a = b$ from **Table 2.1**), it follows from **Eq. (A.15)** that $a^* = 2/(\sqrt{3}a)$ and $c^* = 1/c$. Similarly, from **Eq. (A.16)**, $\alpha^* = \beta^* = 90$ and $\gamma^* = 60$. Then, with **Eq. (A.4)**, the relation between lattice parameters and the interplanar distance measured by XRD is finally derived as

$$\frac{1}{d_{hkl}^{\mathrm{wz}}} = \sqrt{\frac{4}{3}\left(\frac{h^2+k^2+hk}{a^2}\right)+\frac{l^2}{c^2}}. \tag{4.11}$$

Similarly, for zincblende ($\alpha = \beta = \gamma = 90$, and $a = b = c$), the reciprocal lattice vectors' magnitudes $a^* = b^* = c^*$ and angles $\alpha^* = \beta^* = \gamma = 90$ can be obtained, so that

$$\frac{1}{d_{hkl}^{\mathrm{zb}}} = \sqrt{\frac{h^2+k^2+l^2}{a^2}}. \tag{4.12}$$

Moreover, changes in lattice spacings can be identified by θ shifts and be associated with composition gradients or strain [134]. If the film quality is sufficiently high, the so-called *thickness fringes* allow for the quantification of the epilayer's thickness.

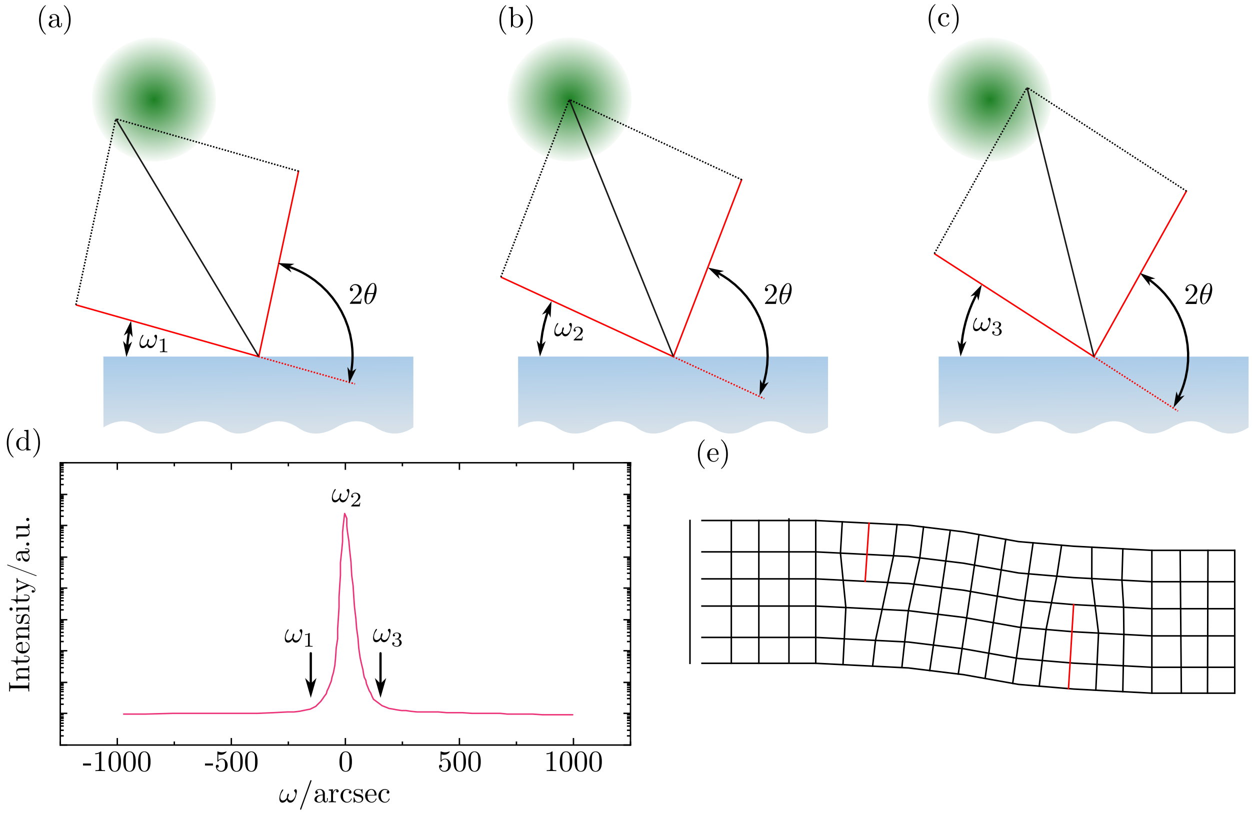

Fig. 4.7. (a)-(c) ω scan at three different positions in reciprocal space, generating a (d) rocking curve. Missing planes and dislocations causing broadening, due to tilting the crystal, of reciprocal points are also shown in (e).

4.2.2 Rocking curve (ω scan)

In an ω scan, 2θ is fixed at a given value for a specific *hkl* reflection. Then, ω is *rocked* about the corresponding reciprocal point, as shown in **Fig. 4.7(a)-(c)**, producing the peak in **Fig. 4.7(d)**. A rocking curve is used as a measurement of crystalline quality of a material. Because of defects, such as dislocations, planes are distorted or missing (see **Fig. 4.7(e)**); therefore, intensity is reduced and reciprocal points broaden. A typically reported value is the full-width at half-maximum (FWHM)) as a figure-of-merit of crystalline quality, with smaller FWHM values meaning higher crystalline quality [134], i.e., lower amount of dislocations. Since the FWHM also depends on film thickness t, a direct comparison is not possible between two films with different thicknesses. To account for that, it can be considered that [135]

$$\mathrm{FWHM} \propto t^{1/3}. \tag{4.13}$$

4.2.3 Pole figures

As mentioned earlier, a pole figure (PF) is a χ-ϕ coupled scan. More specifically, in an XRD PF measurement, 2θ is fixed for a specific *hkl* reflection of interest as in an ω scan. Then, χ is increased in a stepwise fashion from 0 up to 90°, carrying out a ϕ scan from 0 to 360° at every χ step [136]. **Fig. 4.8(a)** shows the geometry of a PF measurement, displaying the movement of both χ and ϕ. Note that these angles are sometimes referred to as $\alpha = 90 - \chi$ and β, respectively. In other words, the scattering vector's direction and magnitude is fixed with respect to the sample while it is being tilted and rotated. Effectively, this maps the top semi-spherical shell in reciprocal space. The angles χ and ϕ can also be thought of as the tilt and rotation needed for a certain plain to be brought into diffraction conditions, i.e., parallel to the surface with respect to the diffractometer. The results of a PF are usually displayed in stereographic or polar projections and entail information on the texture of regions of a macroscopic sample.

Orientation of a sample is given by the so-called *ideal orientation* in Miller indices $(hkl)[uvw]$, with respect to an external Cartesian coordinate system (also known as specimen axes), where (hkl) describes the plane parallel to the surface, i.e., normal to the z axis, and $[uvw]$ the direction pointing to the x axis. For example, the ideal orientation of the crystal shown **Fig. 4.8(b)** is (011)[100]. A resulting PF measurement of the 111 reflections of Nb (011) is shown in **Fig. 4.8(c)**. The signals in the PF indicate to which directions the 111 planes are aligned.

Moreover, instead of tilting and rotating the sample, the X-ray source and detector con be rotated by scanning ω, 2θ, ϕ, and $2\theta\chi$ in a diffractometer with the in-plane $2\theta\chi$ axis. This allows for the sample to stay horizontal during the whole measurement, preventing risks of it falling

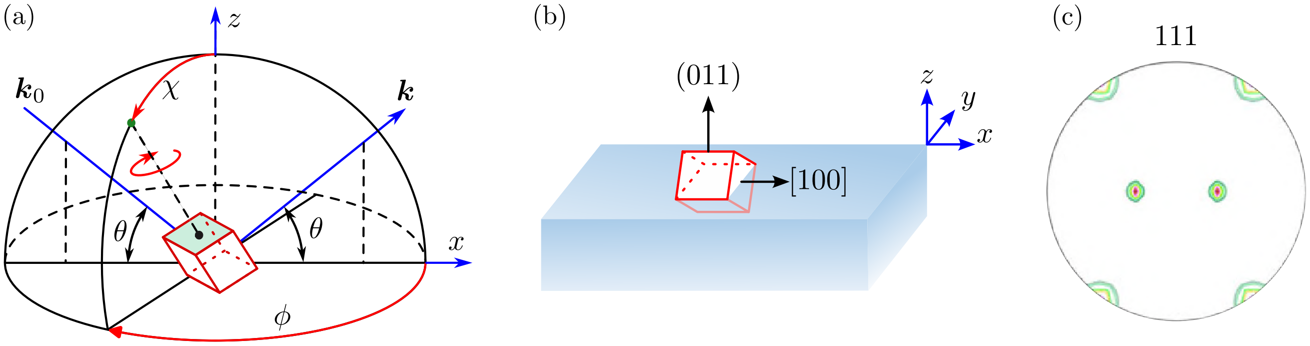

Fig. 4.8. (a) diagram of the geometry used in XRD PF measurements showing the incident $\boldsymbol{k}_0$ and diffracted $\boldsymbol{k}$ vectors. Adapted from [135]. (b) orientation of a crystal within a macroscopic sample. Adapted from [137]. (c) PF measurement of the 111 reflections of Nb (011). Reprinted from [138] with permission of Taylor & Francis.

down from the sample plate [139]. A schematic representation of the in-plane geometry is shown in **Fig. 4.9**.

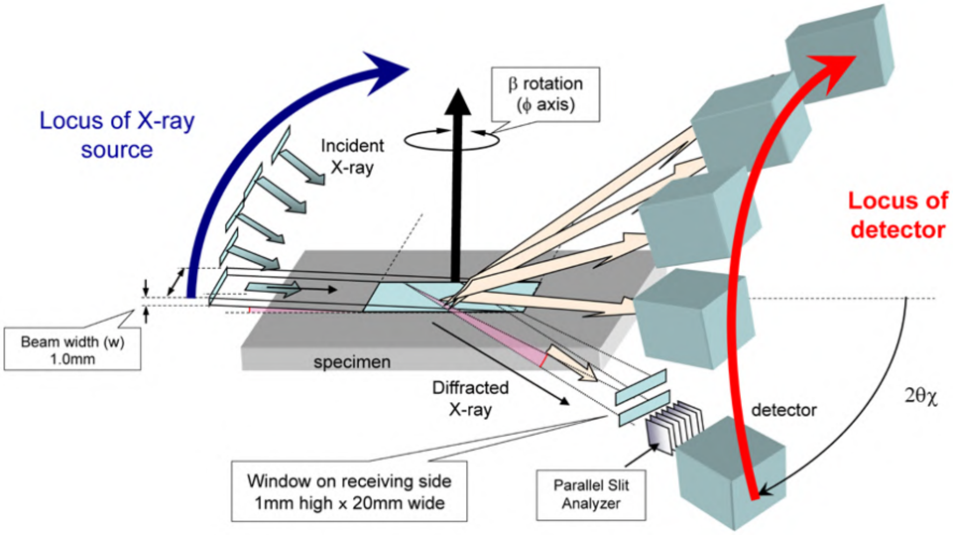

Fig. 4.9. Rigaku's in-plane geometry for the measurement of XRD PF. Reprinted from [139] with permission.

4.3 Phase quantification by XRD

Not only does XRD allow for phase identification, but it also offers the possibility of quantification. For a reflection (hkl), the intensity of a phase i is described by [140]

$$I^i_{hkl} = K_{\mathrm{D}}|F_{hkl}|^2 LPpe^{-2M}\frac{V^i}{v^i}\frac{1}{2\mu}, \tag{4.14}$$

where K_D is constant that includes all factors that are independent on the analyzed phase and reflection (i.e. the intensity of the incident X-ray beam and its wavelength, the diffractometer circle's radius, the illuminated area, and the charge and mass of the electron), p the multiplicity factor, e^{2M} the Debye-Weller temperature factor, μ the absorption coefficient, V^i and v^i the volume fraction and unit cell volume of the phase i. Moreover, the structure factor [131]

$$F_{hkl} = \sum_{n=1}^{n=N} f_n e^{2\pi j(hx_n + ky_n + lz_n)} \tag{4.15}$$

describes the ratio between the amplitude scattered by the atoms in the unit cell and the amplitude scattered by a single electron, where f_n is the atomic form factor of the n-th atom in the unit cell with coordinates (x_n, y_n, z_n) and j is the imaginary unit ($j^2 = -1$). Finally, the Lorentz-polarization factor is given by

$$LP = \frac{1 + \cos^2 2\theta}{\sin 2\theta}\psi, \tag{4.16}$$

where 2θ is the diffraction angle; $\psi = \sin^{-1}\theta$ for powders and constant for single crystals [141].

Now, letting

$$R^i_{hkl} = \frac{|F_{hkl}|^2 LPp}{v^i} \tag{4.17}$$

and

$$T^i = \frac{e^{2M}}{2\mu}, \tag{4.18}$$

the intensity ratio between a reflection from wurtzite and one from zincblende is

$$\frac{I^{\mathrm{zb}}_{hkl}}{I^{\mathrm{wz}}_{hkl}} = \frac{R^{\mathrm{zb}}_{hkl} T^{\mathrm{zb}}}{R^{\mathrm{wz}}_{hkl} T^{\mathrm{wz}}} \frac{V^{\mathrm{zb}}}{V^{\mathrm{wz}}}, \tag{4.19}$$

where the ratio $R^{\mathrm{zb}}_{hkl}/R^{\mathrm{wz}}_{hkl}$ eliminates ψ from **Eq. (4.16)**.

Furthermore, by assuming that the temperature and absorption coefficients are equal in both phases [135, 142] and solving for the volume ratio, **Eq. (4.19)** can be simplified to

$$\frac{V^{\mathrm{zb}}}{V^{\mathrm{wz}}} = \frac{I^{\mathrm{zb}}_{hkl} R^{\mathrm{wz}}_{hkl}}{I^{\mathrm{wz}}_{hkl} R^{\mathrm{zb}}_{hkl}}. \tag{4.20}$$

Since R^i_{hkl} can be calculated by means of **Eq. (4.17)**, it is only necessary to measure the intensity of different reflections from both phases in order to calculate the volume ratio. This is, however, normally used for randomly oriented samples; due to its nature, epitaxial GaN does not belong to this kind of materials. Additionally, the wurtzite/zincblende GaN system exhibits yet another difficulty. As mentioned in **Section 2.1**, the crystalline structure of these two materials is outstandingly similar; hence, some of their XRD reflections are indistinguishable from one another in a common ω-2θ scan. This is greatly illustrated in **Fig. 4.10**, where most of the zincblende reflections overlap with some of wurtzite's. For example, the 0002_{wz} and 111_{zb} or $11\bar{1}0_{\mathrm{wz}}$ and 220_{zb} pairs of reflections.

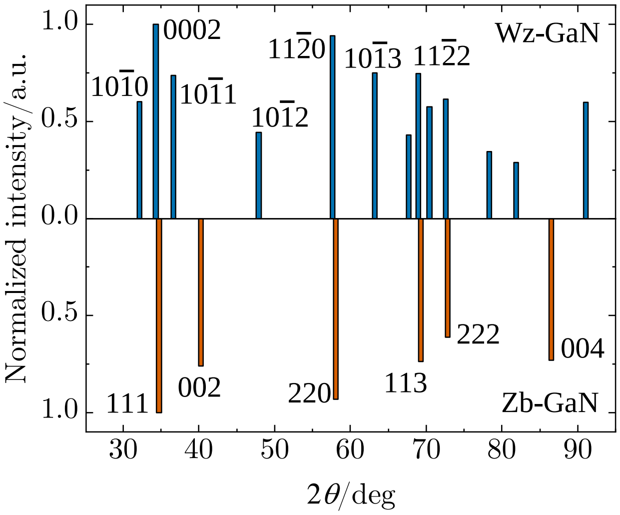

Fig. 4.10. *VESTA3* [45] XRD simulation from wurtzite and zincblende GaN simulated using the structural data from [40] and [43], respectively, using $K\alpha_1$ from **Table 4.1**.

4.3.1 Pole figure in phase quantification

In a highly-textured, epitaxial film, a possible solution is to obtain the intensity through a PF experiment. First, the orientation problem is circumvented since not only the out-of-plane direction is measured, as in an ω-2θ scan, but rather the whole space above the sample is mapped. Moreover, if the symmetry of two overlapping reflections is different, a PF measurement can distinguish between the two. Various combinations have been reported for measuring the phase ratio. For example, for predominantly $(111)_{\mathrm{zb}}$ and $(0001)_{\mathrm{wz}}$ oriented films, the 002_{zb} and $10\bar{1}2_{\mathrm{wz}}$ reflections have been proposed [143]. For $(001)_{\mathrm{zb}}$ GaN, however, some of the 002_{zb} poles come from the in-plane oriented 001_{zb} facets, causing weak intensities with superimposed surface scattering effects [135]. For these orientations, the 113_{zb} and $10\bar{1}3_{\mathrm{wz}}$ reflections have been widely reported [135, 144–146] due to their wide separation in reciprocal space and different symmetry.

With that, the intensity corrected for orientation is just [147]

$$I^{i}_{hkl} = \int_{\chi=0}^{\pi} \int_{\phi=0}^{2\pi} I(\chi,\phi) d\chi d\phi, \tag{4.21}$$

where $I(\chi,\phi)$ is the intensity measured in a PF at different (χ,ϕ) points.

To obtain the volumetric percentage of, for instance, zincblende, one can simply calculate

$$C^{\mathrm{zb}} = \frac{V^{\mathrm{zb}}}{V^{\mathrm{wz}} + V^{\mathrm{zb}}} = \frac{V^{\mathrm{zb}}/V^{\mathrm{wz}}}{1 + V^{\mathrm{zb}}/V^{\mathrm{wz}}}. \tag{4.22}$$

where the volume ratio can be calculated with the help of **Eq. (4.20)**.

Part III: Simulations

Chapter 5: Pole Figure Simulation

5.1 Geometrical considerations

5.1.1 Pole figure angles

Recall from **Section 4.2** that a pole figure (PF) maps a semi-spherical shell in reciprocal space, where the radius is defined by the length of the scattering vector (proportional to $1/d_{hkl}$). Considering that the reciprocal space maps the orientation of the different crystalline families of planes (see **Appendix A**), it is possible to calculate the χ and ϕ angles at which certain reflections appear in a PF if the orientation of a crystal is known.

Let $\boldsymbol{Z}$ be the vector normal to the sample representing the plane $(h_z k_z l_z)$ and $\boldsymbol{X}$ a vector lying on the plane defined by $\boldsymbol{Z}$ whose direction is normal to $(h_x k_x l_x)$ plane. With $\boldsymbol{H}$ representing a plane of interest with indices (hkl), the angle between $\boldsymbol{Z}$ and $\boldsymbol{H}$ directly gives the polar angle χ (see **Fig. 4.8(a)** in **Chapter 4**) and is obtained through

$$\cos\chi = \frac{\boldsymbol{H}\cdot\boldsymbol{Z}}{HZ}. \tag{5.1}$$

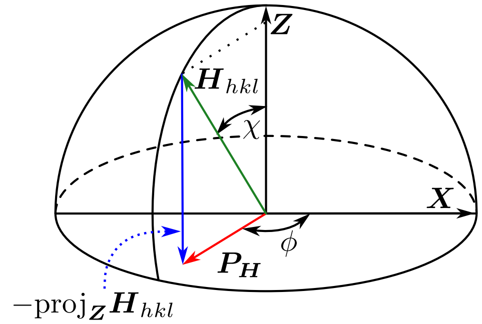

Fig. 5.1. Geometry for calculating ϕ.

To obtain ϕ, however, the geometry in **Fig. 5.1** needs to be discussed first. Let $\boldsymbol{P_H}$ be the projection of $\boldsymbol{H}$ onto the plane defined by $\boldsymbol{Z}$, then ϕ is the angle between $\boldsymbol{P_H}$ and $\boldsymbol{X}$. From the figure, it is clear that $\boldsymbol{P_H}$ can be obtained by subtracting the projection of $\boldsymbol{H}$ onto $\boldsymbol{Z}$ from $\boldsymbol{H}$ so that

$$\boldsymbol{P_H} = \boldsymbol{H} - \mathrm{proj}_{\boldsymbol{Z}}\boldsymbol{H}, \tag{5.2}$$

which can be expanded to

$$\boldsymbol{P_H} = \boldsymbol{H} - (\boldsymbol{H} \cdot \hat{\boldsymbol{Z}})\hat{\boldsymbol{Z}}, \tag{5.3}$$

with $\hat{\boldsymbol{Z}} = \boldsymbol{Z}/Z$. Having calculated $\boldsymbol{P_H}$, ϕ can be finally computed with

$$\cos\phi = \frac{\boldsymbol{P_H} \cdot \boldsymbol{X}}{P_H X}. \tag{5.4}$$

5.1.2 Rotation with quaternions

Before computing χ and ϕ with the help of **Eq. (5.1)** and **Eq. (5.4)**, it may be desired to apply a rotation about certain axes, for example, if the PF of a twin is to be simulated. To that end, quaternions are a great tool that simplifies the process. A quaternion may be defined as 4-tuple of real numbers so that [148]

$$\mathrm{u} = (u_0, u_1, u_2, u_3), \tag{5.5}$$

where u_0, u_1, u_2, and u_3, are real, scalar numbers. Take into account the notation utilized in this context to differentiate between a vector $\boldsymbol{u}$ (written in bold italics), its norm $|\boldsymbol{u}| = u$ (written in italics), and a quaternion u (written in roman). Quaternions can, too, be regarded as the sum of scalar u_0 and a 3-dimensional vector $\boldsymbol{u} = u_1\hat{\boldsymbol{x}} + u_2\hat{\boldsymbol{y}} + u_3\hat{\boldsymbol{z}}$ such that

$$\mathrm{u} = u_0 + \boldsymbol{u}. \tag{5.6}$$

Of special interest in quaternion algebra is the rotation operator $L_{\mathrm{u}}(\boldsymbol{v})$. Let u be a unit quaternion (i.e., $|\mathrm{u}| = 1$), then

$$u_0^2 + |\boldsymbol{u}|^2 = 1, \tag{5.7}$$

which, using the identity $\cos^2\Omega + \sin^2\Omega = 1$, must fulfill

$$\begin{aligned} u_0 &= \cos\Omega, \\ |\boldsymbol{u}| &= \sin\Omega, \end{aligned} \tag{5.8}$$

for some angle Ω. Then, taking

$$\hat{\boldsymbol{u}} = \frac{\boldsymbol{u}}{|\boldsymbol{u}|} = \frac{\boldsymbol{u}}{\sin\Omega}, \tag{5.9}$$

the unit quaternion u can be rewritten in terms of Ω and $\hat{\boldsymbol{u}}$

$$\mathrm{u} = \cos\Omega + \hat{\boldsymbol{u}}\sin\Omega. \tag{5.10}$$

The rotation operator $L_{\mathrm{u}}(\boldsymbol{v})$ then acts on a vector $\boldsymbol{v}$ as follows

$$L_{\mathrm{u}}(\boldsymbol{v}) = \mathrm{u}\mathrm{v}\mathrm{u}^* = \mathrm{v}_r, \tag{5.11}$$

where the quaternion $\mathrm{v} = 0 + \boldsymbol{v}$ and the conjugate of u

$$\mathrm{u}^* = \cos\Omega - \hat{\boldsymbol{u}}\sin\Omega \tag{5.12}$$

are being used. Applying $L_{\mathrm{u}}(\boldsymbol{v})$ returns a quaternion v_r whose component $\boldsymbol{v_r}$ is a vector rotated about $\hat{\boldsymbol{u}}$ through 2Ω, fulfilling $|\boldsymbol{v_r}| = |\boldsymbol{v}|$ [148], as shown in **Fig. 5.2**

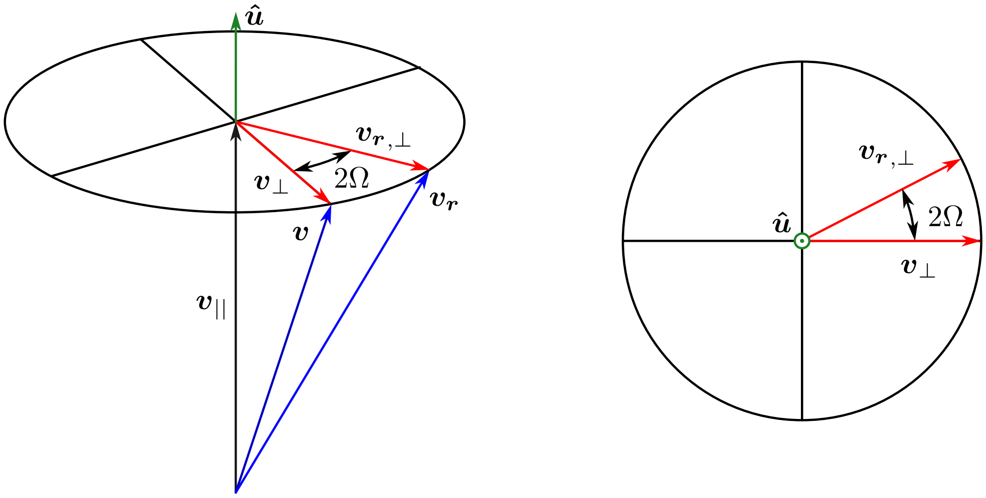

Fig. 5.2. Trimetric and top views from vector rotation geometry using quaternions. Adapted from [148].

Lastly, the last step necessary is to define the quaternion multiplication used in **Eq. (5.11)**. Let u and v be arbitrary quaternions, the product uv is

$$\mathrm{w} = \mathrm{u}\mathrm{v} = u_0 v_0 - \boldsymbol{u}\cdot\boldsymbol{v} + u_0\boldsymbol{v} + v_0\boldsymbol{u} + \boldsymbol{u}\times\boldsymbol{v}, \tag{5.13}$$

which can be separated into its scalar and vector components

$$\begin{aligned} w_0 &= u_0 v_0 - \boldsymbol{u}\cdot\boldsymbol{v}, \\ \boldsymbol{w} &= u_0\boldsymbol{v} + v_0\boldsymbol{u} + \boldsymbol{u}\times\boldsymbol{v}. \end{aligned} \tag{5.14}$$

Finally, from $\mathrm{v}_r = \mathrm{w}\mathrm{u}^*$, calculated in the same manner, the vector component can be extracted

$$\boldsymbol{v_r} = w_0\boldsymbol{u}^* + u_0^*\boldsymbol{w} + \boldsymbol{w}\times\boldsymbol{u}^*. \tag{5.15}$$

For a detailed derivation of **Eq. (5.13)**, the reader is referred to Kuipers [148].

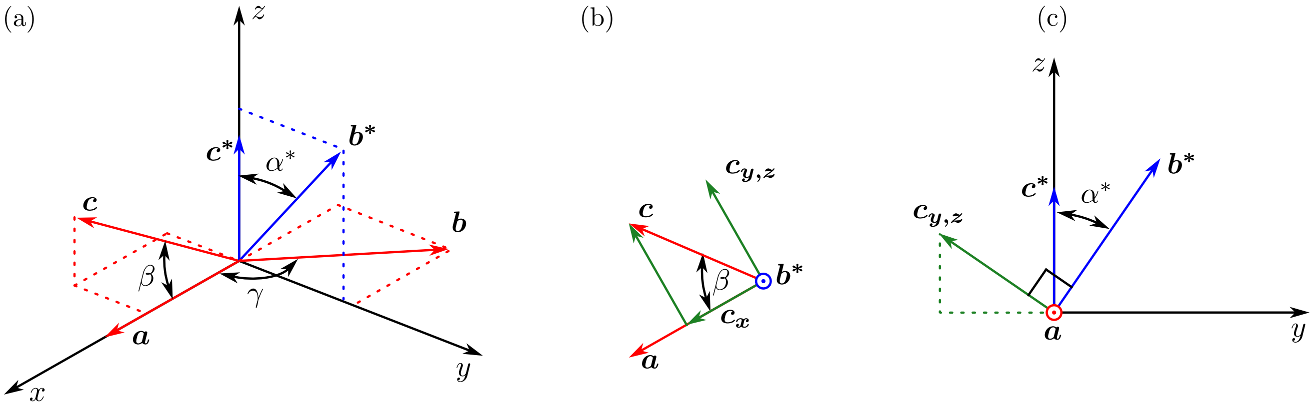

Fig. 5.3. Relationship between the orthonormal system and the real and reciprocal axes.

5.1.3 Orthogonalization

Recalling **Eq. (A.2)**, it is necessary to compute the reciprocal vectors $\boldsymbol{a}^*$, $\boldsymbol{b}^*$, and $\boldsymbol{c}^*$ in order to calculate $\boldsymbol{H}$. For these, in turn, **Eq. (A.14)** needs the lattice vectors $\boldsymbol{a}$, $\boldsymbol{b}$, and $\boldsymbol{c}$. Since the real-lattice vectors are not generally orthogonal, the first step to start the calculations consists of rewriting $\boldsymbol{a}$, $\boldsymbol{b}$, and $\boldsymbol{c}$ in terms of an orthonormal basis, i.e., $\hat{\boldsymbol{x}}$, $\hat{\boldsymbol{y}}$, and $\hat{\boldsymbol{z}}$ in a Cartesian coordinate system. Consider the diagram in **Fig. 5.3(a)**, where $\boldsymbol{a}$ has been aligned with the Cartesian x axis and $\boldsymbol{c}^*$ with the z axis [149]. With such alignment, it is trivial to define the first lattice vector

$$\boldsymbol{a} = a\hat{\boldsymbol{x}}. \tag{5.16}$$

From **Eq. (A.11)**, it follows that $\boldsymbol{c}^*||z$ and $\boldsymbol{b}$ are orthogonal; therefore, $\boldsymbol{b}$ lies within the xy plane, with an angle γ to the x axis. With that, $\boldsymbol{b}$ is can be expanded as

$$\boldsymbol{b} = b\cos\gamma\hat{\boldsymbol{x}} + b\sin\gamma\hat{\boldsymbol{y}}. \tag{5.17}$$

As for $\boldsymbol{c}$, it is somewhat more problematic to write in Cartesian coordinates. With β the angle between $\boldsymbol{c}$ and the x axis, the x coordinate is just $\boldsymbol{c}_{\boldsymbol{x}} = c\cos\beta\hat{\boldsymbol{x}}$. Once more, **Eq. (A.11)** dictates that $\boldsymbol{b}^*$ is perpendicular to both $\boldsymbol{a}$ and $\boldsymbol{c}$ so a view along $\boldsymbol{b}^*$, such as in **Fig. 5.3(b)**, shows the ac plane. Subtracting the x coordinate $\boldsymbol{c}_{\boldsymbol{x}}$ from $\boldsymbol{c}$ results in a vector $\boldsymbol{c}_{\boldsymbol{y},\boldsymbol{z}}$ on the ac plane, being therefore normal to $\boldsymbol{b}$. Furthermore, because the x coordinate was subtracted, $\boldsymbol{c}_{\boldsymbol{y},\boldsymbol{z}}$ also lies on the yz plane. Similarly, due to the aforementioned condition that $(\boldsymbol{a}||\hat{\boldsymbol{x}}) \perp \boldsymbol{b}^*$, it follows that $\boldsymbol{b}^*$ lies within the yz plane as well. With all the previous information, the diagram in **Fig. 5.3(c)** can be finally drawn, where a view along $\boldsymbol{a}$ shows the yz plane. From there, it follows that $\boldsymbol{c_y} = -c\sin\beta\sin(90^\circ - \alpha^*)\hat{\boldsymbol{y}}$ and $\boldsymbol{c_z} = c\sin\beta\cos(90^\circ - \alpha^*)\hat{\boldsymbol{z}}$, where the magnitude $|\boldsymbol{c_{y,z}}| = c\sin\beta$ from **Fig. 5.3(b)** was used. Having already obtained $\boldsymbol{c_x}$, $\boldsymbol{c}$ is finally written as

$$\boldsymbol{c} = c\cos\beta\hat{\boldsymbol{x}} - c\sin\beta\cos\alpha^*\hat{\boldsymbol{y}} + c\sin\beta\sin\alpha^*\hat{\boldsymbol{z}}, \tag{5.18}$$

where the identities $\sin(90^\circ - \alpha^*) = \cos\alpha^*$ and $\cos(90^\circ - \alpha^*) = \sin(\alpha^*)$ were used. As a summary, the three real-lattice vectors can be written

$$\begin{bmatrix} \boldsymbol{a} \\ \boldsymbol{b} \\ \boldsymbol{c} \end{bmatrix} = \begin{bmatrix} a & 0 & 0 \\ b\cos\gamma & b\sin\gamma & 0 \\ c\cos\beta & -c\sin\beta\cos\alpha^* & c\sin\beta\sin\alpha^* \end{bmatrix} \begin{bmatrix} \hat{\boldsymbol{x}} \\ \hat{\boldsymbol{y}} \\ \hat{\boldsymbol{z}} \end{bmatrix}. \tag{5.19}$$

5.2 Simulation with Python

5.2.1 Defining crystal orientation

Armed with the real-lattice vectors of an arbitrary crystal system written in terms of an orthonormal basis and the rotation operator, it is now possible to perform PF calculations of differently oriented crystals. In the following, the core parts of a Python script powering the PF simulations are detailed and related to the fundamentals treated in this work. The code has been uploaded and made publicly available in a Github repository [150].

The process starts with the definition of the `Crystal` Python class (blueprint in object-oriented programming, not to be confused with crystal class related to crystal symmetry), as shown in code lines 10 through 14. `Crystal` takes as argument the material in the parameter `mat` (a string, e.g., `’GaN’`), the crystal system in `system` (a string with the first three letters of the system, e.g. `’cub’` for cubic), the indices of the out-of-plane $\boldsymbol{Z}$ and in-plane $\boldsymbol{X}$ orientations (see **Fig. 5.1**) in `z` and `x` (Python lists, e.g., `[1,-1,2]`). If the orientations from the indices passed to `z` and `x` are not mutually orthogonal, the script calculates the correct value of either $\boldsymbol{Z}$ or $\boldsymbol{X}$ depending on the argument passed to the `approximation` parameter.

```
10 class Crystal:
11     def __init__(self, mat=’GaN’, system=’cub’, z=[0,0,1], x = [1,0,0],
12                  approximation=’x’):
13         self.mat = mat
14         self.system = system
```

When instantiated (discussed in the following section), the program first takes the inputs and stores it in variables belonging to the `Crystal` Python class (denoted as `self` in the definition).

If no values are entered, the script takes the default values after the `=` sign.

After some formatting (not discussed), from lines 40 through 42, a database is first loaded by the function `get_database()`. This database contains the six lattice parameters of the material and crystalline system entered as `Crystal` is instantiated (or default arguments if they are not given). Then, the functions `lattice_parameters()` and `orient()` are sequentially called, the latter with the arguments `z`, `x`, and `approximation` being passed from the instantiation of `Crystal`.

```
40        self.get_database()
41        self.lattice_parameters()
42        self.orient(z,x, approximation)
```

Real- and reciprocal-lattice vectors

The first function initially calls the values of a, b, c, $\cos\alpha$, $\cos\beta$, $\cos\gamma$, $\sin\alpha$, $\sin\beta$, and $\sin\gamma$, loaded from the database, and store them in the variables `a`, `b`, `c`, `cosal`, `cosbe`, `cosga`, `sinal`, `sinbe`, and `singa`, respectively.

```
60    def lattice_parameters(self):
61        a, b, c = self.real_spacing
62        cosal, cosbe, cosga = np.cos(self.real_ang_rad)
63        sinal, sinbe, singa = np.sin(self.real_ang_rad)
```

Then, the program uses **Eq. (A.16)** to calculate the reciprocal angles and stores the $\cos\alpha^*$ and $\sin\alpha^*$ in variables `cosal_r` and `sinal_r`.

```
65        try:
66            recip_ang_rad = np.arccos([
67                            (cosbe*cosga-cosal)/(sinbe*singa),
68                            (cosga*cosal-cosbe)/(singa*sinal),
69                            (cosal*cosbe-cosga)/(sinal*sinbe)])
70
71            cosal_r = np.cos(recip_ang_rad[0])
72            sinal_r = np.sin(recip_ang_rad[0])
```

That makes everything needed to calculate the real-lattice vectors in terms of an orthonormal basis. The matrix on the right side of **Eq. (5.19)** is then calculated and stored in `real_v`. Each row in `real_v` contains the three components of the real-lattice vectors $\boldsymbol{a}$, $\boldsymbol{b}$, and $\boldsymbol{c}$ in terms of $\hat{\boldsymbol{x}}$, $\hat{\boldsymbol{y}}$, and $\hat{\boldsymbol{z}}$. Note that each vector can be accessed individually by subsetting the `real_v` array.

```
79        self.real_v = np.array([
80                        [a,       0,                0],
81                        [b*cosga, b*singa,          0],
82                        [c*cosbe, -c*sinbe*cosal_r, c*sinbe*sinal_r]])
```

Right after, the volume is calculated, with the `numpy` function `linalg.det()` computing the determinant of the real-lattice vectors in `real_v` (**Eq. (A.13)**). The reciprocal-lattice vectors can now be calculated with the three cross products in **Eq. (A.14)**. In the code, the `numpy` function `cross()` serves that purpose, yielding the `recip_v` matrix, containing the three components of the three vectors. Note that Python uses 0-based indexing, meaning that the first element of an array is obtained by subsetting the 0-th element of such array.

```
84          Volume = np.linalg.det(self.real_v)
85
86          self.recip_v = np.array([
87                      np.cross(self.real_v[1], self.real_v[2]),
88                      np.cross(self.real_v[2], self.real_v[0]),
89                      np.cross(self.real_v[0], self.real_v[1])])/Volume
```

Orientation vectors from Miller indices

Once the reciprocal vectors have been calculated and the `lattice_parameters()` function finishes executing (see code lines 40 through 42), the function `orient()` is called with the arguments `z`, `x`, and `approximation` (as mentioned previously). This function uses the reciprocal vectors and the Miller indices of $\boldsymbol{Z}$ and $\boldsymbol{X}$ (specimen axes, see **Section 4.2**). Within `orient()`, the function `indices_to_vectors()` is called twice, once to convert indices (hkl) to a vector with an orthonormal basis and once more for $[uvw]$. With $\boldsymbol{Z}$ and $\boldsymbol{X}$ stored in `z_vector` and `x_vector`, the program is able to calculate $\boldsymbol{Y}$ through the cross product.

```
91      def orient(self, z, x, approximation):
92          self.z_vector = self.indices_to_vectors(z)
93          self.x_vector = self.indices_to_vectors(x)
94          self.y_vector = np.cross(self.z_vector, self.x_vector)
```

To convert indices to vectors, the function `indices_to_vectors()` takes in a Python list, containing the three indices, and stores them in a 2D `numpy` array. It then calculates the value of the matrix multiplication of **Eq. (A.6)** between the 3×1 `indices` and the 3×3 `recip_v` (obtained previously) arrays. This results in a 2D array whose first element (0 index in Python language) is an 3×1 array containing the components in an orthonormal basis representing the Miller indices passed in to the function.

```
111     def indices_to_vectors(self, indices):
112         indices = np.array([indices])
113         return np.matmul(indices, self.recip_v)[0]
```

5.2.2 PF angles of a family of planes

The previous section covered everything that happens when the `Crystal` Python class is instantiated. Instantiation of the Python class can be carried out by firstly importing `Crystal` from `cristal`, where the latter (lower case) is the name of the file (”crystal.py”) in which the `Crystal` Python class is defined. Then, it is enough to run, for example,

```
c1 = Crystal(mat='GaN', system = 'hex', z=[0,0,1], x = [1,0,0])
```

which calculates the vectors $\boldsymbol{a}$, $\boldsymbol{b}$, $\boldsymbol{c}$, $\boldsymbol{a}^*$, $\boldsymbol{b}^*$, $\boldsymbol{c}^*$, $\boldsymbol{Z}$, $\boldsymbol{Y}$, and $\boldsymbol{X}$ in terms of an orthonormal basis of wurtzite GaN (0001)[10$\bar{1}$0], i.e., $\boldsymbol{Z} = \boldsymbol{H}_{0001}$ and $\boldsymbol{X} = \boldsymbol{H}_{10\bar{1}0}$. Note that the parameters of `z` and `x` are passed as a list of only three indices regardless of the crystalline system, while the notation in this work uses four indices for hexagonal crystals. Calling now the method `add_pole()` on `c1` suffices to calculate a PF of a certain family of planes, say for example the $\{10\bar{1}0\}$.

```
c1.add_pole(ref=[1,0,0])
```

The `add_pole()` method is defined in the `Crystal` Python class as follows

```
    def add_pole(self, ref, twin_axis=None, twin_angle=None):
```

```
        self.planes_in_family(ref, twin=twin,
                              twin_axis=twin_axis,
                              twin_angle=twin_angle,
                              axis=axis)
        self.PF_plot()
```

After defining some functionality for rotations (not discussed), `planes_in_family()` performs the heavy lifting by using combinations and permutations to determine all the members of a certain family. Inside the `planes_in_family()`, the function `indices_to_vectors()` is called to obtain a vector $\boldsymbol{H}_{hkl}$ for each plane in the family (as described at the end of **Section 5.2.1**).

Finally, the function `calc_chi_phi()` is also called, where the following lines of the `Crystal` Python class definition

```
        chi = self.angle_between_vectors(self.z_vector, plane_vector)
        P_H = self.proj(plane_vector, self.z_vector)
        phi = self.angle_between_vectors(P_H, self.x_vector)
```

determine the angles χ and ϕ using **Eq. (5.1)** and **Eq. (5.4)**.

Once `planes_in_family()` finishes executing, the function `PF_plot()` produces a polar projection plot of the calculated angles, which can be saved to a file `'test.png'` by calling the method `save_fig()` on `c1`

```
c1.save_fig('test.png')
```

Fig. 5.4 shows the unit cell of wurtzite GaN with the $\{10\bar{1}0\}$ planes besides the simulated PF by the code described so far. All these planes are parallel to $\boldsymbol{Z}$, and therefore a tilted 90°. Moreover, since these planes represent the faces of a hexagon, the angles between them are 60°. Both of these features are clearly reproduced by the simulated PF.

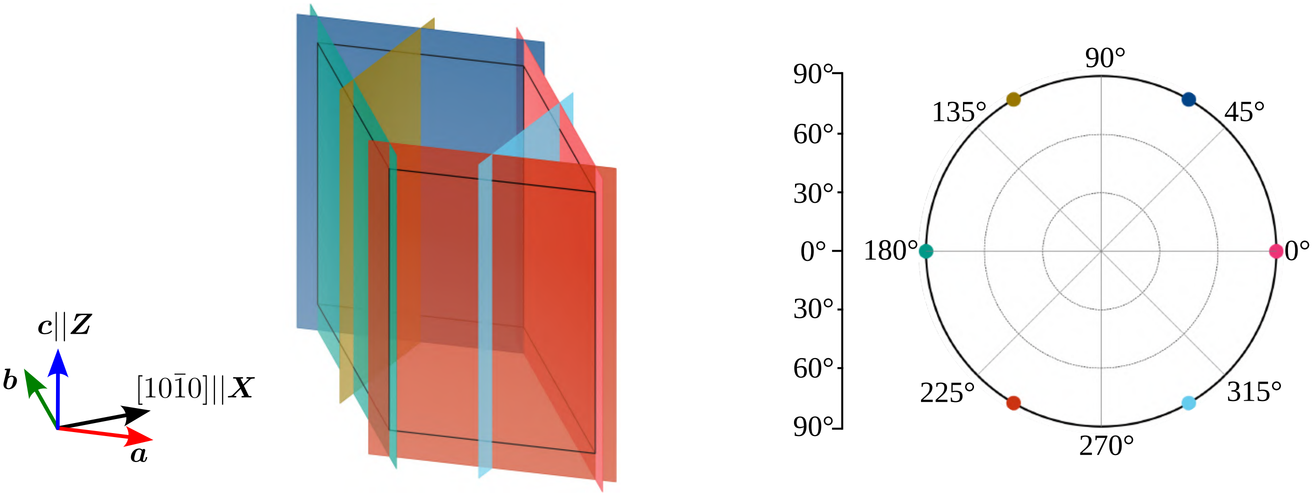

Fig. 5.4. Wurtzite unit cell showing the 6 $\{10\bar{1}0\}$ planes with the resulting simulation. Some of the planes, drawn using *VESTA3* [45] with data from **Table 2.1**, are shifted from their original place and colors of the PF were changed for a better view.

Furthermore, **Fig. 5.5(a)** shows the same unit cell with the $\{10\bar{1}3\}$ planes. In this case, it is not a trivial task to identify the angles at a first glance. A deeper analysis, however, brings clarity to the problem at hand. First, ϕ can be found with the projections onto the plane defined by $\boldsymbol{Y} = \boldsymbol{H}_{0001}$, which can be simply obtained by subtracting the projection of $\boldsymbol{H}_{10\bar{1}3}$ onto $\boldsymbol{H}_{0001}$, which is just $\boldsymbol{H}_{0003}$, from $\boldsymbol{H}_{10\bar{1}3}$—see **Eq. (5.2)**—resulting in $\boldsymbol{H}_{10\bar{1}0}$, that is, the same as for the $\{10\bar{1}0\}$ planes in the previous example. This means that the azimuthal angle ϕ between the $\{10\bar{1}3\}$ planes is 60°.

To determine χ, two views along $\boldsymbol{a}$ and [110] are represented in **Fig. 5.5(c)** and **Fig. 5.5(d)**. The first view displays the planes $(01\bar{1}3)$ and $(0\bar{1}13)$ extending into and out from the page. Measuring the angle between $\boldsymbol{Z}$ and the vectors representing these two planes yields $\chi \approx 32$ in both cases. The same values can be obtained for the $(1\bar{1}03)$ and $(\bar{1}103)$ in the view along [110].

Looking at the simulated PF in **Fig. 5.5(b)**, the 6 signals appear to have a separation of 60° between one another. Furthermore, the $\chi \approx 32$ can also be extracted from the PF. Exact values from the simulation can be obtained by inspecting the `dfs` attribute of `c1`, a Python dictionary that stores `pandas` data frames containing the information of each plane and its respective ϕ and χ angles.

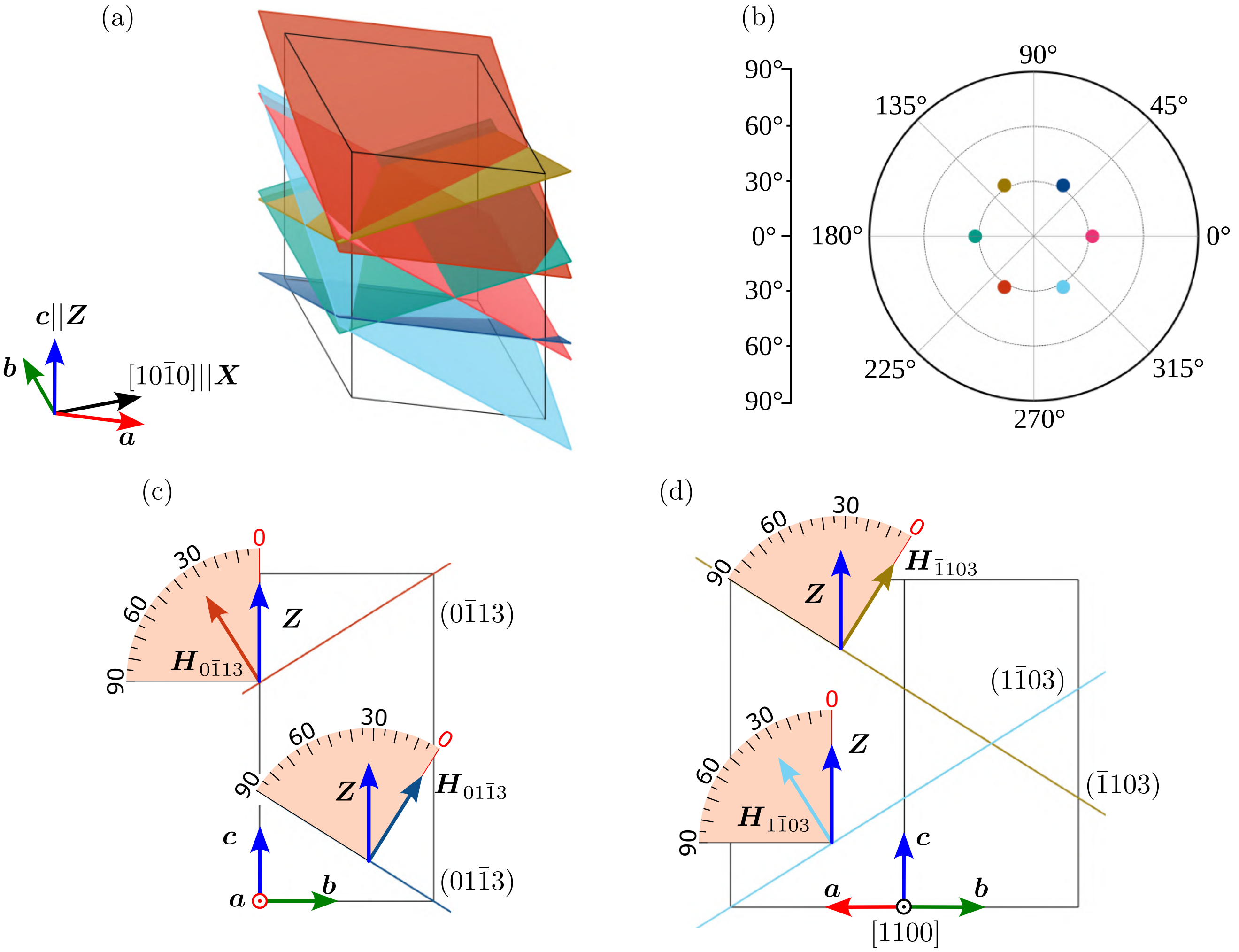

Fig. 5.5. (a) wurtzite unit cell showing 6 of the 12 $\{10\bar{1}3\}$ planes compared to the (b) simulation. Views along (c) $\boldsymbol{a}$ and (d) [110] so that polar angles are clearer to identify. Some planes are shifted from their original positions.

Subsetting the Python dictionary for the first family and the data frame

```
c1.dfs['1']['df']
```

yields the following information shown in **Table 5.1**, from which a few key points can be discussed. First, although there are 12 $\{10\bar{1}3\}$ planes, the angles at which a certain (hkl) plane appears are exactly the same for $(\bar{h}\bar{k}\bar{l})$. Therefore, they appear in pairs and only 6 signals are observed. Furthermore, the planes appear at a polar angle χ of 32.09° and at every 60° in the azimuthal angle ϕ, that is, exactly as discussed in previous paragraphs, thus validating the calculations.

Table 5.1. Polar χ and azimuthal ϕ angles for the different planes in the $\{10\bar{1}3\}$ family as calculated by the simulations.

Plane	χ/deg	ϕ/deg	Plane	χ/deg	ϕ/deg
$(10\bar{1}3)$	32.09	0	$(\bar{1}01\bar{3})$	32.09	0
$(01\bar{1}3)$	32.09	60	$(0\bar{1}1\bar{3})$	32.09	60
$(\bar{1}103)$	32.09	120	$(1\bar{1}0\bar{3})$	32.09	120
$(\bar{1}013)$	32.09	180	$(10\bar{1}\bar{3})$	32.09	180
$(0\bar{1}13)$	32.09	240	$(01\bar{1}\bar{3})$	32.09	240
$(1\bar{1}03)$	32.09	300	$(\bar{1}10\bar{3})$	32.09	300

5.2.3 Rotation and twins

As stated before, it could be of use to predict the PF of a twinned crystal, such as in this work. For that end, it could be only necessary to perform the simulation as in the previous section provided that the orientation vectors $\boldsymbol{Z}$ and $\boldsymbol{X}$ of the twin are known beforehand. However, this is not always the case and frequently only the twin axis and/or angle are known. For such cases, rotations about specific axes defined by their (hkl) indices can be performed.

Consider the unit cell in **Fig. 5.6(a)** schematizing a GaN (0001)$[10\bar{1}0]$ wurtzite unit cell with 6 $\{10\bar{1}3\}$ planes rotated by 54.7° about $\boldsymbol{b}$ (such rotation relates wurtzite to zincblende and will be discussed in more detail throughout **Section 5.2.3**). In this case, again, it is not a trivial task to visually identify the tilt and azimuthal angles .

To start the analysis, nevertheless, a view along $\boldsymbol{b}$ is shown in **Fig. 5.6(c)**, parallel to the planes $(10\bar{1}3)$ and $(\bar{1}013)$, with $\boldsymbol{c}$ inclined 54.7° about $\boldsymbol{b}$. From the drawing, measuring the angle between $\boldsymbol{H}_{10\bar{1}3}$ and $\boldsymbol{Z}_T$ ($\boldsymbol{Z}$ after applying the rotation), for example, yields $\chi_{10\bar{1}3} \approx 22°$. On the other hand, the angle between $\boldsymbol{H}_{\bar{1}013}$ and $\boldsymbol{Z}_T$ is $\chi_{\bar{1}013} \approx 87°$. Furthermore, because the planes are perpendicular to the page, their respective vectors lie within it, resulting in $\chi = 0$ for both planes. According to the previous analysis, a GaN sample with this orientation would need top be tilted $\approx 22°$ counterclockwise about $\boldsymbol{b}$ to bring the $(10\bar{1}3)$ plane into diffraction condition, i.e., parallel to the surface, with no rotation needed, should an x-ray diffraction PF measurement experiment be carried out.

As for the $(01\bar{1}3)$ plane, a rotation about $\boldsymbol{Z}_T$ of $\approx 28.5°$ is necessary for the alignment, as shown in the view of **Fig. 5.6(d)**, generated by rotation about $\boldsymbol{Z}_T$ clockwise as viewed from the top through 28.5° using *VESTA3* [45]. After rotating, it is easier to see that the required polar angle is $\chi \approx 75°$, and, since a clockwise rotation was needed to bring the plane perpendicular to the page, it follows that the it is located at $\phi \approx 28.5°$ in the counter-clockwise direction.

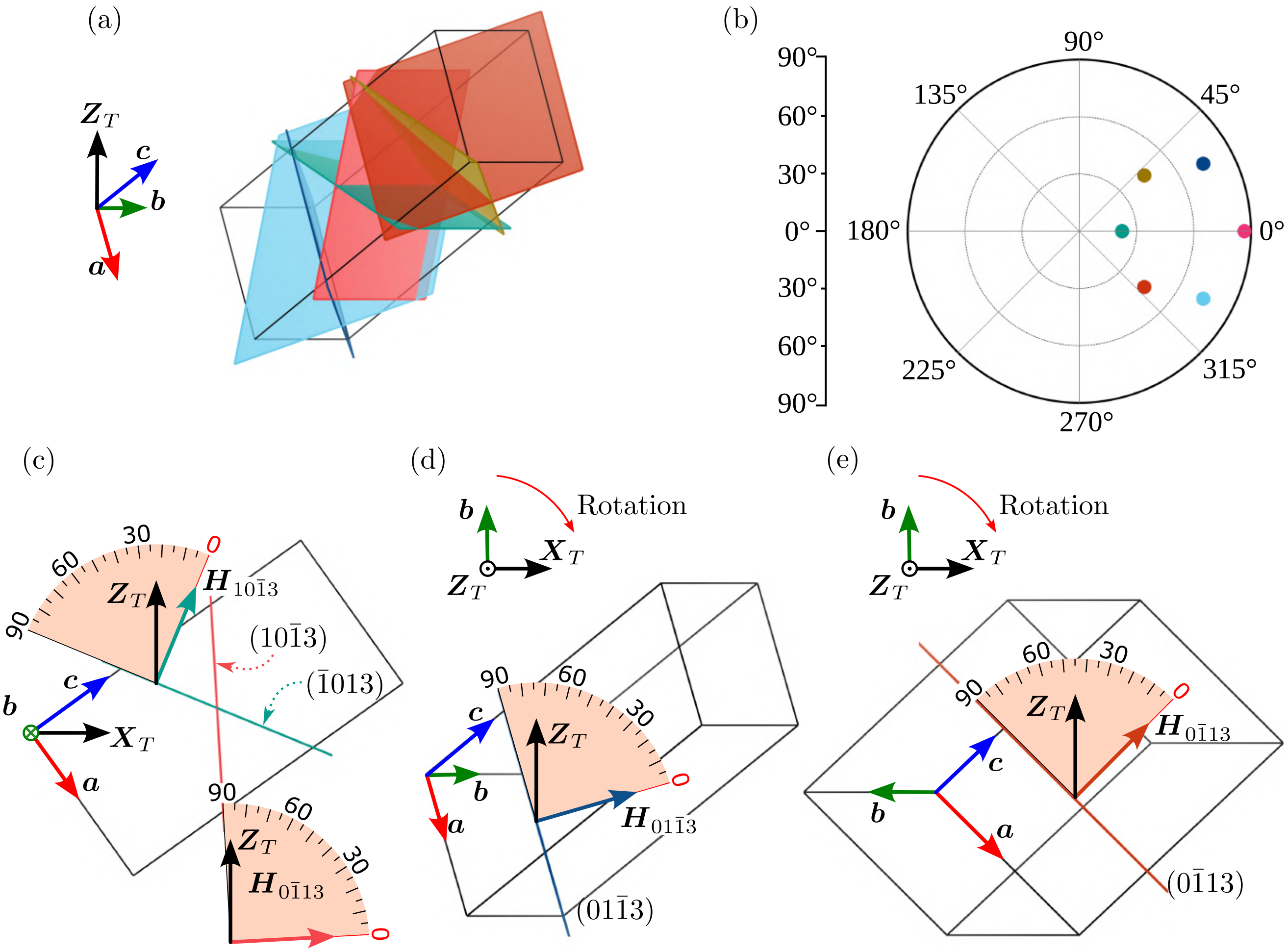

Fig. 5.6. (a) wurtzite unit cell rotated 54.5° about ***b*** showing 6 $\{10\bar{1}3\}$ planes compared to the (b) simulation. Views along (c) ***b*** with further rotations by (d) 28.5° and (e) 319.3° about $\boldsymbol{Z}_T$.

Similarly, **Fig. 5.6(e)** shows the view obtained after rotating the unit cell about $\boldsymbol{Z}_T$ through 319.5° clockwise from the top. Measuring the angle in this case results in $\chi \approx 45°$, that, combined with $\phi \approx 319.5°$ counter-clockwise, makes the complete description of the orientation of the $(0\bar{1}13)$ plane.

The simulated PF in **Fig. 5.6(b)** is then simply produced by first instantiating the `Crystal` Python class, naming it `c2` for example, just as in the previous example

```
c2 = Crystal(mat='GaN', system = 'hex', z=[0,0,1], x = [1,0,0])
```

Then, when adding the poles by calling the method `add_pole()` on `c2`, the twin axis and angle can be passed as additional parameters such as

```
c2.add_pole(ref=[1,0,3], twin_axis='b', twin_angle=54.7)
```

where the argument `54.7` indicates a rotation by 54.7°, whereas the `'b'` argument passed to the `twin_axis` parameter indicates that the rotation is to be carried out around $\boldsymbol{b}$, calculated at instantiation as previously mentioned.

The rotation is carried out by the function `calc_chi_phi()` (see **Section 5.2.2**) calling the function `rotate_vector()` onto each $\boldsymbol{H}_{hkl}$ vector before calculating χ and ϕ. Note that indices can also be used as arguments for the `twin_axis` parameter instead of `'b'`. The function `rotate_vector()`, defined within the `Crystal` Python class, calculates the rotation of `v` (the vector defining each plane), about `u` ($\boldsymbol{b}$ in this example) trough `ang` (54.7°) as follows

```python
    def rotate_vector(self , v, v2, ang):
        if ang == 0:
            return v

        angle = np.deg2rad(ang)
        u = np.sin(angle/2)*v2/np.linalg.norm(v2)
        u0 = np.cos(angle/2)
        u_conj = -u
        w = u0*v+np.cross(u,v)
        w0 = -np.dot(u,v)
        vr = w0*u_conj + u0*w + np.cross(w, u_conj)
        return vr
```

where `u` and `u0` correspond to $\boldsymbol{u}$ and u_0 components of u in **Eq. (5.10)**, `w` and `w0` to $\boldsymbol{w}$ and w_0 in **Eq. (5.14)**, and `vr` to $\boldsymbol{v_r}$ in **Eq. (5.15)**, which is the vector sought after.

With all that, the final results from this simulation are shown in **Table 5.2**. Comparing to the angles obtained from **Fig. 5.6** and *VESTA3* [45], a very good agreement is found. Considering that the angles in the figure were measured visually with the help of a protractor, the error between the two data sets can be considered negligible, validating the simulations once more.

Table 5.2. Tilt χ and rotation ϕ angles for the different planes in the $\{10\bar{1}3\}$ family.

Plane	χ/deg	ϕ/deg	Plane	χ/deg	ϕ/deg
$(10\bar{1}3)$	86.79	0	$(\bar{1}01\bar{3})$	86.79	0
$(01\bar{1}3)$	74.17	28.57	$(0\bar{1}1\bar{3})$	74.17	28.57
$(\bar{1}103)$	45.06	40.53	$(1\bar{1}0\bar{3})$	45.06	40.53
$(\bar{1}013)$	22.61	0	$(10\bar{1}\bar{3})$	22.61	0
$(0\bar{1}13)$	45.06	319.47	$(01\bar{1}\bar{3})$	45.06	319.47
$(1\bar{1}03)$	74.17	331.43	$(\bar{1}10\bar{3})$	74.17	331.43

Part IV: Experimental Section

Chapter 6: Nucleation Temperature of undoped zb-GaN epilayers

6.1 Growth

6.1.1 PAMBE setup

A group of 4 samples (series **S**) was prepared in Riber C21 molecular beam epitaxy (MBE) system in order to investigate the effect of nucleation temperature on the crystalline properties of zb-GaN epilayers. The MBE system used, shown in **Fig. 6.1**, is equipped with ionic pumps that produce a background pressure of $\sim 5 \times 10^{-10}$ Torr. During growth of nitrides, a cryogenic pump can also be used which, in combination with flowing liquid N_2, brings the pressure down to $\sim 3 \times 10^{-10}$ Torr.

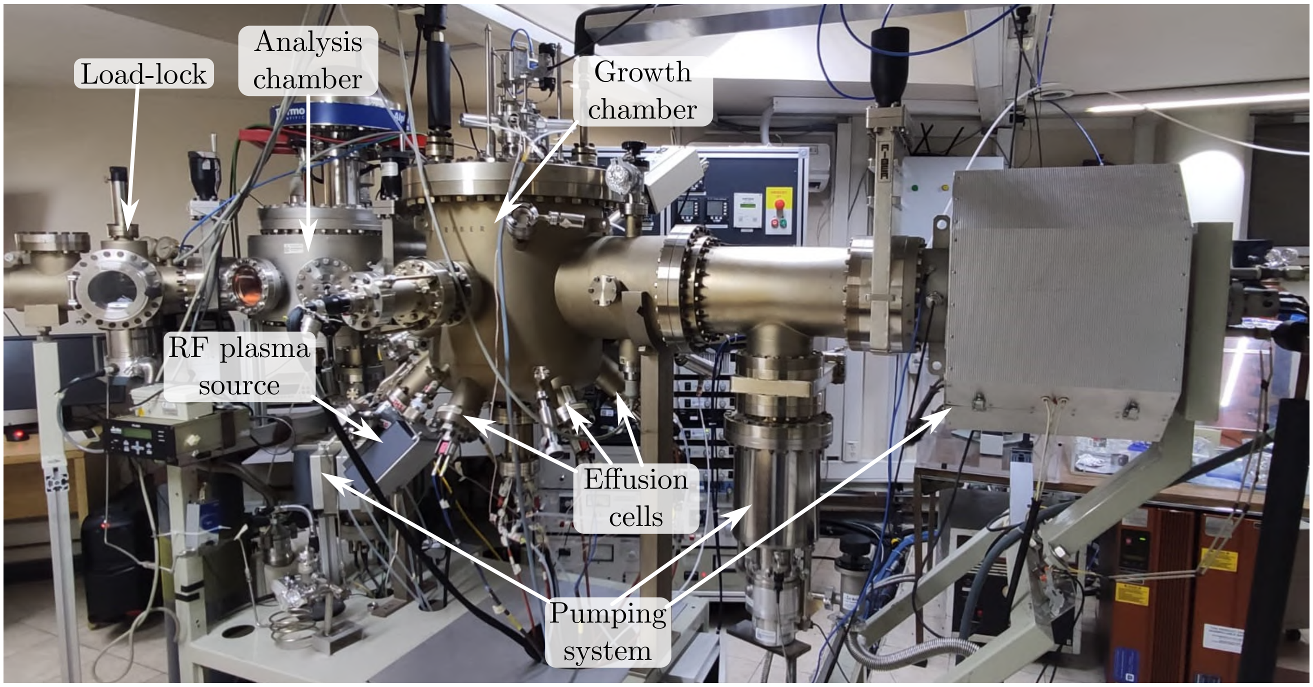

Fig. 6.1. Riber C21 MBE system used for the growth of the samples.

Furthermore, the growth chamber utilizes an RF plasma source in order to provide reactive N species. On the other hand, conventional effusion cells are used to provide Ga and As (as well as Mg, used for the series **N** and **G** discussed in **Chapter 7**) species. To maintain the pressure in the main chamber, there is an analysis chamber that acts as a buffer right after the load-lock.

6.1.2 Growth conditions

The growth process of the samples with structure as in **Fig. 6.2** started by introducing the GaAs (001) substrates to the MBE through the load-lock. After being transferred to the growth chamber, they were heated up to 580 °C for 20 minutes in order to clean the surface. To prevent GaAs decomposition due to As desorption, the As shutter was opened when the substrate reached 380 °C to supply an As overpressure using a beam equivalent pressure (BEP) of 7.59×10^{-6} Torr, obtained by heating the As cell to 137 °C. The process was monitored by reflection high-energy electron diffraction, revealing a clean surface once the GaAs (2×4) reconstruction appeared.

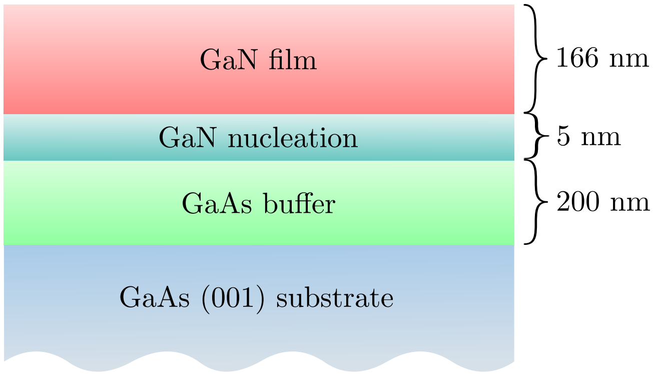

Fig. 6.2. Structure of the samples grown for series **S**.

Table 6.1. Substrate temperature for the nucleation layer growth of samples within series **S**.

Sample	T_{n}/°C
S1	655
S2	665
S3	675
S4	685

On top of the reconstructed surface, the growth of a 200 nm thick GaAs buffer layer was carried out after the substrate temperature was raised to 590 °C. This was achieved by simply opening the Ga shutter at a $\mathrm{BEP}_{\mathrm{Ga}}$ of 2.58×10^{-7} Torr, with a Ga cell temperature of 941 °C, while keeping As flux for 15 minutes. Subsequently, the Ga shutter was closed and its temperature decreased to 929 ° C, for a $\mathrm{BEP}_{\mathrm{Ga}}$ of 2.06×10^{-7}, while the substrate temperature was raised once more to the nucleation temperature as shown in **Table 6.1** in 3 minutes.

Meanwhile, the N plasma source was initiated and stabilized at 150 W and 0.4 sccm of N_2 flux. At that point, the growth of a 5 nm thick GaN nucleation layer started by opening the N and, 3 seconds later, Ga shutters. After the first 30 seconds of the GaN nucleation layer growth, As flux toward the substrate was stopped and only the Ga and N shutters remained open (see **Section 3.2.3**). After 90 seconds of starting the nucleation layer, the substrate temperature was raised one last time in 72 seconds to 700 °C for the last layer. For that, the Ga and N shutters were left open for 40 minutes more for a total of 166 nm in nominal thickness. **Fig. 6.3** shows a schematic of the growth temperature and cells used.

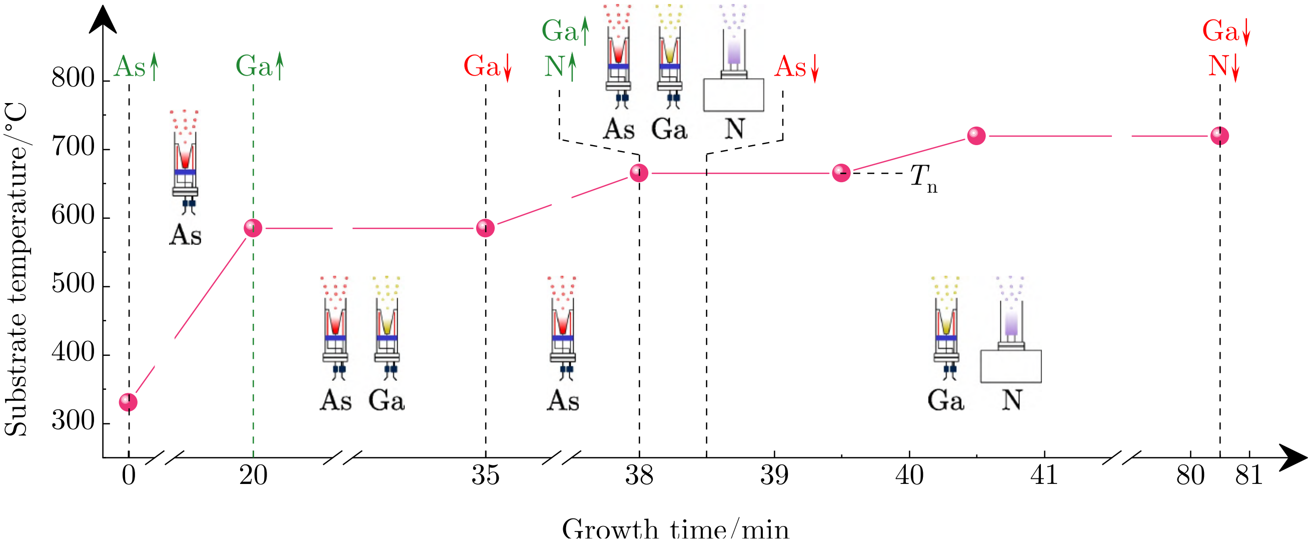

Fig. 6.3. Temperature during growth. Green (red) remarks with upward (downward) arrows indicate when a cell was opened (closed).

6.2 Characterization

6.2.1 Morphology

In order to characterize the surface of the samples, Nomarski micrographs were taken with a magnification of x50. Moreover, scanning electron microscopy (SEM) measurements were carried out in a JEOL 7401F, using an acceleration voltage of 2 kV with a lower secondary electron detector. Additionally, atomic force microscopy (AFM) was carried out in an AutoProbe CR-C Instrument from Veeco to study the roughness variations as function of the nucleation temperature. To that end, root mean square (RMS)-roughness measurements were taken from 10×10 μm^2 AFM scans using the free, open-source software Gwyddion [151]. To gain an insight on inhomogeneity, 5 measurements across different areas of the sample were taken.

6.2.2 Crystallinity

To study the out-of-plane orientation, symmetric x-ray diffraction (XRD) ω-2θ scans were conducted between 30° and 90° in a Rigaku SmartLab system, equipped with a rotatory Cu anode working as a Kα light source conditioned in parallel beam, first treated with a two-bounce Ge (220) monochromator before hitting the sample. After diffraction, the beam was received by a 5° collimator before being collected by a point detector. To compare the crystalline quality, by means of the full-width at half-maximum (FWHM), ω scans were carried out on 5 areas about the 002_{zb} reflection using an additional two-bounce Ge (220) analyzer on the receiving end.

To measure crystalline phase purity, complete pole figure (PF) measurements ($\phi = 0$ to 90°, $\chi = 0$ to 360°) were also taken from the samples in an in-plane configuration (**Fig. 4.9**), using two 0.5° collimators with no monochromator or analyzer. The samples were placed in the holder such that the $\langle 110 \rangle_{\mathrm{GaAs}}$ directions (identified by the cleavage planes) pointed to $\phi = 0$ ($\boldsymbol{X}$). For zincblende, the 2θ angle was fixed for the 113 reflection, while the $10\bar{1}3$ was measured for wurtzite (see **Section 4.3.1**). Then, the PF underwent absorption and background corrections using the 3D Explore software from Rigaku. Since randomly oriented GaN samples were not available, a Si powder reference provided by Rigaku was utilized for defocus corrections following the method described by Saleh et al. [152].

Subsequently, the integrated intensity of both reflections was calculated using **Eq. (4.21)**, enabling the determination of the volumetric phase ratio between wurtzite and zincblende using **Eq. (4.22)**. For the zincblende reflections, a multiplicity (number of visible planes) of 12 was considered, whereas a multiplicity of 6 was used for the wurtzite reflections. The XRD PF measurements were taken over 3 different areas of the sample to obtain statistical information on sample uniformity. From the zincblende PF, additionally, the twin content was calculated by measuring using the same process taking into account the intensity coming from twinned reflections with a multiplicity of 6, as discussed in **Section 6.3**. The obtained PF were compared to simulations carried out as described in **Chapter 5**. All orientation relationships between zincblende, zincblende twins, and wurtzite were calculated using the same script.

Finally, the samples were characterized via electron backscatter diffraction (EBSD) in a JEOL 7610F SEM, equipped with an Oxford EBSD detector, using an acceleration voltage of 15 kV, yielding an information depth of a few tenths of nm [153, 154], and sample tilt of 70° from the horizontal. The EBSD data was processed using the free, open-source library MTEX [155] for MATLAB® to plot phase and orientation maps. The orientation density function (ODF) was also calculated, from which the EBSD PF and inverse PF (IPF) were obtained.

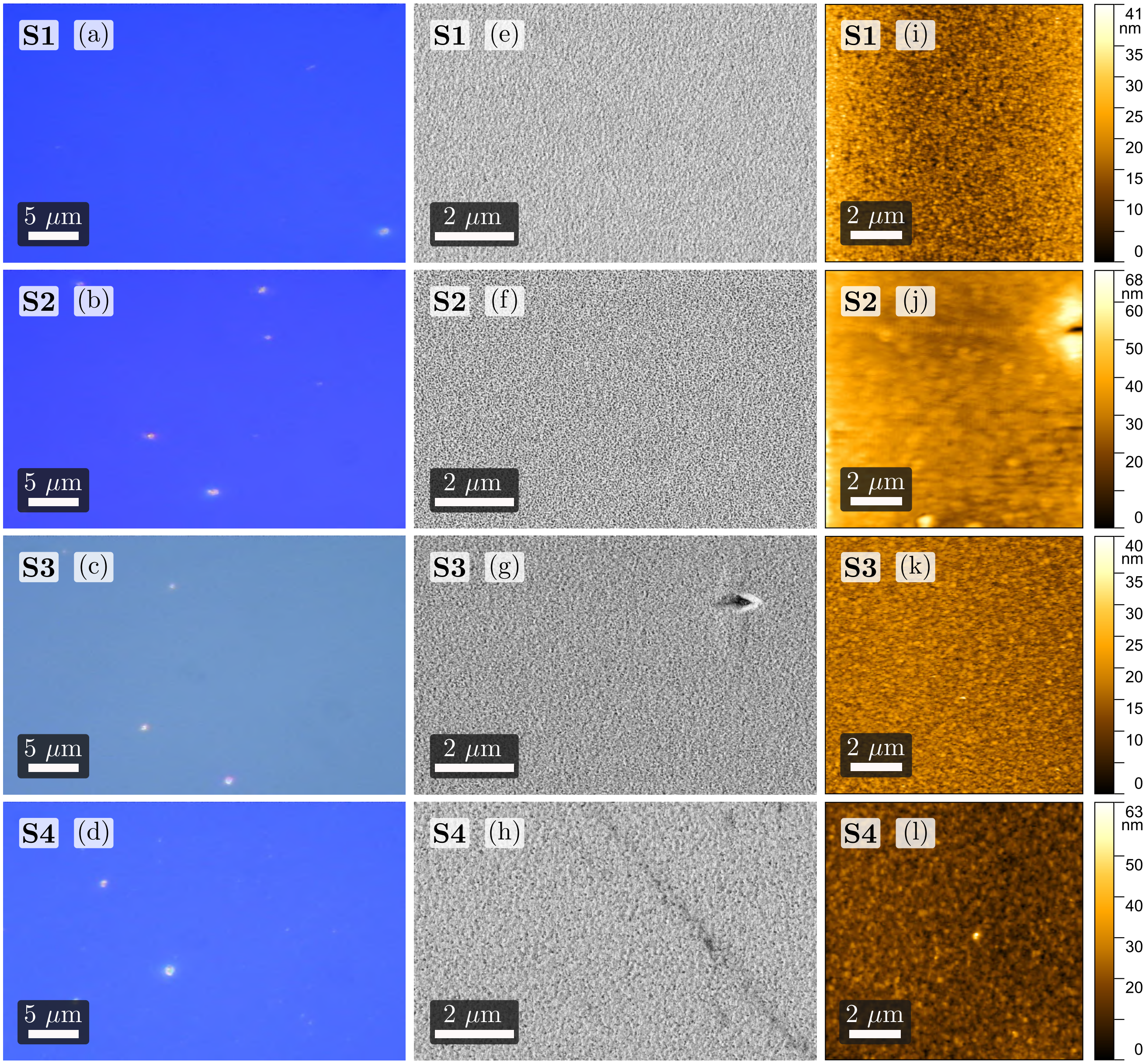

Fig. 6.4. (a)-(d) Nomarski, (e)-(h) SEM, and (i)-(l) AFM micrographs from the surface of samples **S1** through **S4**.

6.3 Results and discussion

6.3.1 Morphology

Fig. 6.4 shows Nomarski, SEM, and AFM micrographs from samples **S1** through **S4**. The Nomarski images show sign of some metal droplets on the surface of the samples. They are, however, in much a lesser amount than in series **G**, which will be discussed in Chapter 7. Conversely, SEM and AFM reveal rough surfaces with pits for the complete set and no droplets were identified in these micrographs. Although SEM and AFM suggest that the growth took place under N-rich conditions, Nomarski microscopy indicates that the growth was rather Ga-stabilized. It is likely that, because of heating transport inhomogeneity, different temperatures resulted in various growth regimes across a single sample. RMS-roughness values are presented and discussed in **Section 6.3.9**.

6.3.2 Out-of-plane orientation

The resulting ω-2θ scans from the four samples of series **S** are show in **Fig. 6.5**. The two reflections from the GaAs (001) substrate are clearly visible dominating the x-ray diffractograms. Moreover, the presence of the 002_{zb} and 004_{zb} GaN reflections confirm that the dominant out-of-plane orientation of the grown zb-GaN was the (001), much like the substrate. Furthermore, the peak at about 34.5° suggest either zb-GaN misorientation toward the [111] direction or the formation of wz-GaN inclusions. The latter assumption is supported by the appearance of the 0004_{wz} GaN reflection. Note, however, that the intensity of this reflection is barely above the noise level of the machine used for the measurement and is therefore not a categorical confirmation.

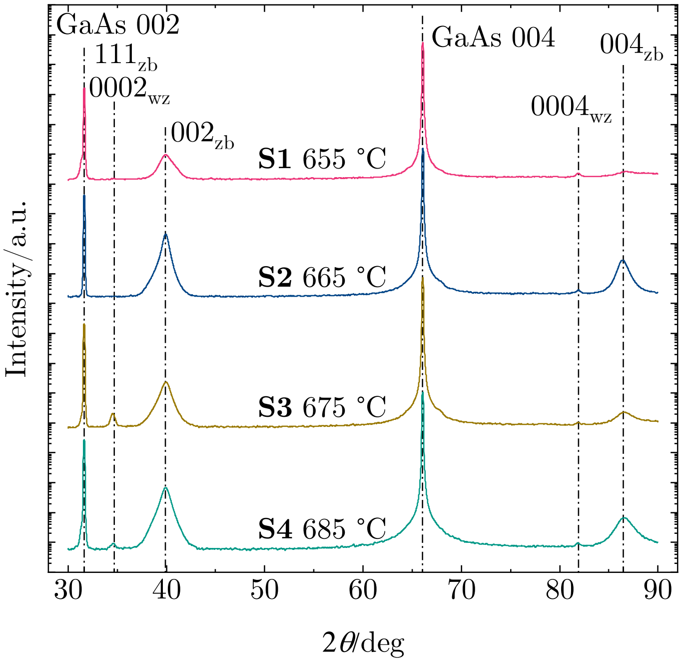

Fig. 6.5. XRD ω-2θ scans from series **S**. Reflections belong to zincblende and wurtzite GaN, unless otherwise stated.

Comparing the different nucleation temperatures, a few points can be discussed. In the first place, the two higher temperatures entail more pronounced $0002_{\mathrm{wz}}/111_{\mathrm{zb}}$ and 0004_{wz} reflections, indicating a greater amount of inclusions and misorientation. The two lowest temperatures, on the other hand, seemed to have caused a noticeable lesser amount of these two types of defects, since the $0002_{\mathrm{wz}}/111_{\mathrm{zb}}$ peak is completely absent. From these latter two samples, the one with $T_{\mathrm{n}} = 655$ °C, sample **S1**, presented a less intense 002_{zb} and an almost absent 004_{zb} reflection. Sample **S2**, conversely, presents the remarkably more intense 002_{zb} and 004_{zb} GaN signals. It is important to note that wz-GaN inclusions should not be discarded due to the appearance of the weak 0004_{wz} peak. Therefore, further analysis is required to make a precise assessment of crystalline quality.

6.3.3 Simulated zincblende pole figures

To better understand the experimental XRD PF results, **Fig. 6.6(a)** shows the simulated PF of the $\{113\}_{\mathrm{zb}}$ planes of GaN with Miller indices (001)[110]. Only 12 poles can be observed from the 24 members of the $\{113\}_{\mathrm{zb}}$ family due to XRD not being able to distinguish a plane (hkl) from its inverse $(\bar{h}\bar{k}\bar{l})$. Furthermore, **Fig. 6.6(b)** shows the simulation of the same family of planes obtained from the same crystal after adding rotations through 60° about the $\langle 111 \rangle$ twin axes.

The values for the angles and axes were chosen to fit the experimental results shown in **Section 6.3.4**. Note that 6 out of the 12 visible poles overlap with the poles from the untwinned simulation. In the calculations for twin content, only the 6 non-overlapping poles are considered and, therefore, the considered multiplicity factor is 6. The reader is referred to **Chapter 5** for a detailed description on how the simulations are performed.

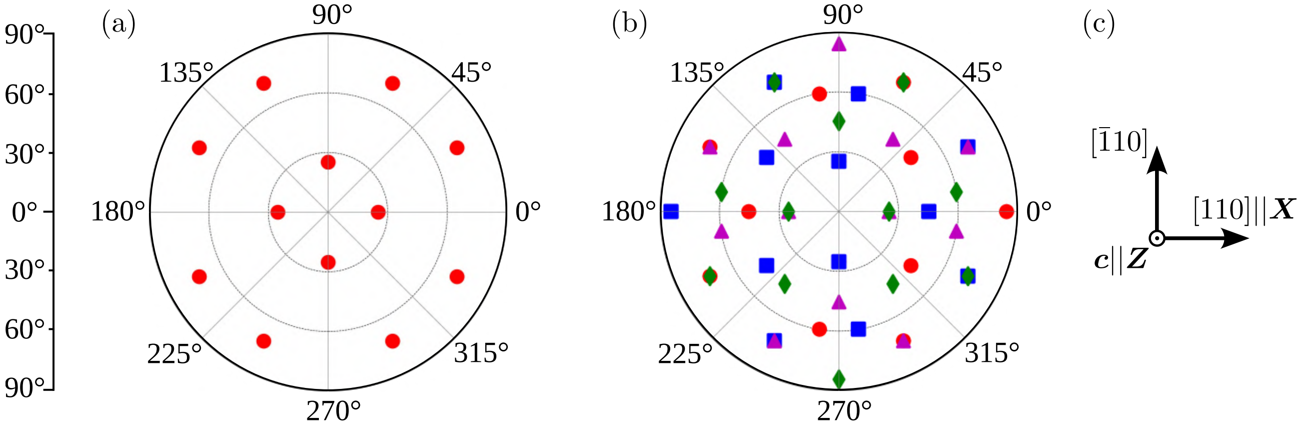

Fig. 6.6. Simulation of the 113_{zb} (a) without and (b) with rotations through 60° about the: [111] (red circles); [$\bar{1}\bar{1}$1] (blue squares); [$\bar{1}$11] (magenta triangles); and [1$\bar{1}$1] (green diamonds) directions. The axes in (c) indicate the orientation considered before rotation. Parts of this figure are published in [156].

6.3.4 Experimental zincblende pole figures

Using the results from the simulated 113_{zb} PF, **Fig. 6.7** shows a comparison between the experimental results and the predictions. For sample **S1** in **Fig. 6.7(a)**, the poles coming from the GaN (001)[110] 113_{zb} reflection are indicated with red circles, just as in the simulated PF in **Section 6.3.3**. The 12 visible poles from the $\{113\}_{zb}$ family are identified in the PF from all samples nearby the χ and ϕ angles where they are predicted showing their characteristic 4-fold symmetry. Together with the ω-2θ scans in **Fig. 6.5**, the PF categorically confirm the successful epitaxial growth of zb-GaN on GaAs with the same ideal orientation (001)[110] as the substrate.

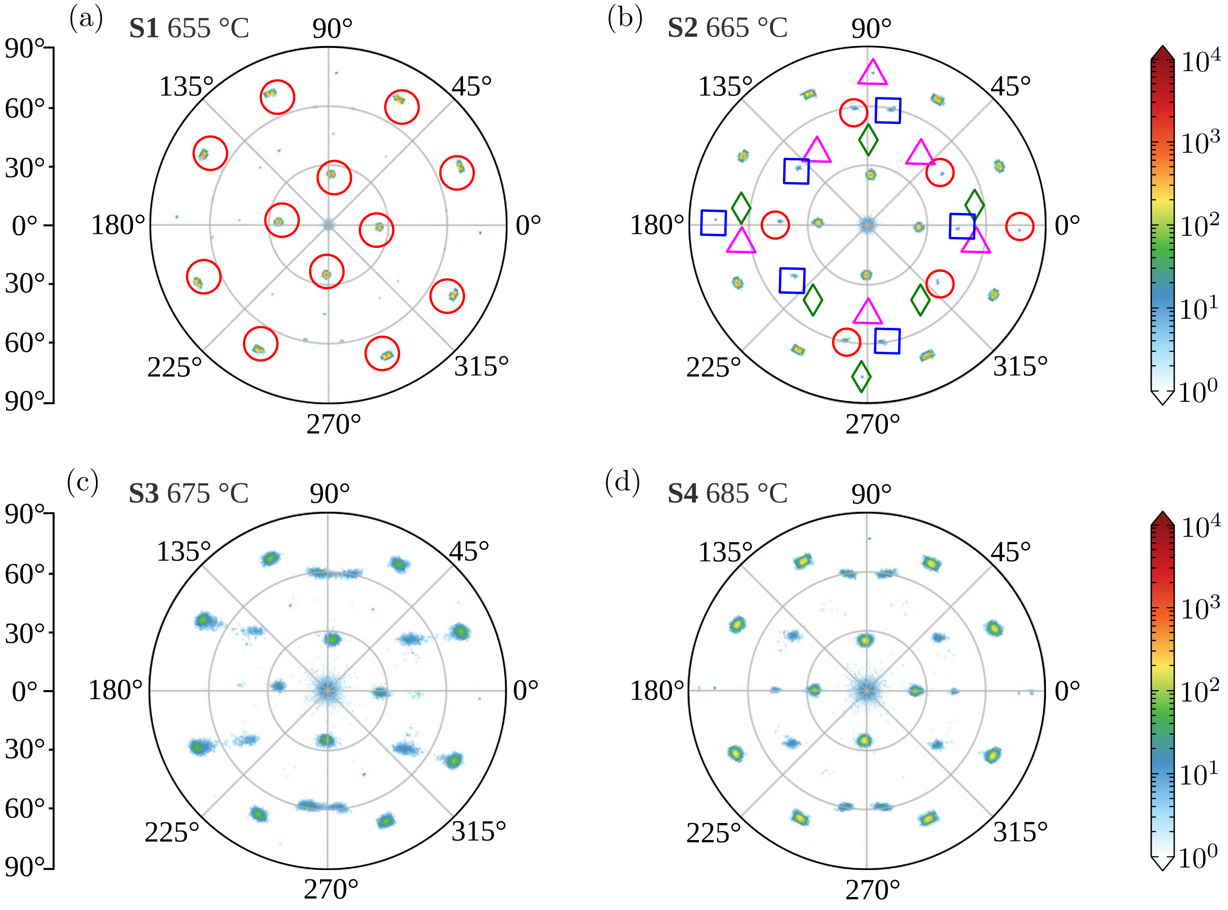

Fig. 6.7. Experimental PF from samples (a) **S1**, (b) **S2**, (c) **S3**, and (d) **S4**. In (a), the signals from the untwinned 113_{zb} GaN (001)[110] reflections are indicated with data from the simulation. In (b), the same is indicated for twinned 113_{zb} GaN (001)[110] reflections. Note that the the specimen axis $\boldsymbol{X}$ points toward 0° while the $\boldsymbol{Z}$ points out from the page as in the simulated PF in **Fig. 6.6**. The nucleation temperatures are indicated.

The other poles appearing in the experimental 113_{zb} PF are attributed to twins formed during growth by rotations through 60° about the $\langle 111\rangle_{zb}$ twin axes, generated by rotation of the triple bond—see **Fig. 2.2(d)**—by 60° changing the correct zincblende stacking from

ABCA**B**CABC to ABCA**B**ACBA, where stacking is still that of zincblende's but mirrored, in this example, with respect to layer **B**. In **Fig. 6.7(b)**, 6 of the 12 visible 113_{zb} reflections are indicated using the same symbols and colors as in the simulation shown in **Fig. 6.6(b)**. The remaining 6 poles overlap with those from untwinned crystal and are therefore not marked.

Just as in the simulation, red circles indicate the reflections generated by the twin formed by rotation through 60° about the [111] axis. Similarly, the blue squares, magenta triangles, and green diamonds indicate the reflections from the twins obtained by rotation through the same angle about the $[\bar{1}\bar{1}0]$, $[\bar{1}11]$, and $[1\bar{1}1]$ axes. A complete description of orientation, i.e., with Miller indices in $(hkl)[uvw]$ format, can be made from the 4 twins by analyzing carefully the rotations made.

For instance, to calculate the $\boldsymbol{H}_{hkl}||\boldsymbol{Z}$ for the twin indicated by red circles in **Fig. 6.6(b)**, a rotation through -60° about the [111] axis can be applied to $\boldsymbol{H}_{001}$ (which is parallel to $\boldsymbol{Z}$ before the rotation). This would result in an $\boldsymbol{H}_{hkl}$ vector that will lie perpendicular to the surface once the original rotation (through 60°) is applied. Using the software described throughout **Chapter 5**, this can be simply done by using the method `rotate_vector()` as shown in **Section 5.2.3** yielding the vector $\boldsymbol{H}_{hkl}||\boldsymbol{Z}$, which can be transformed back to Miller indices by using the method `vector_to_indices()`. With this, the Miller indices of twins generated by rotation about [111] and $[\bar{1}\bar{1}1]$ are $(\bar{1}22)[411]$ and $(1\bar{2}2)[41\bar{1}]$, respectively. On the other hand, the ideal orientation of the twins by rotation about the $[\bar{1}11]$ and $[1\bar{1}1]$ are $(\bar{2}\bar{1}2)[101]$ and $(212)[10\bar{1}]$. Notice that the rotations through 60° are equivalent to those through -60° (just as the two rotation directions yield the same result along the stacking direction in **Fig. 2.2**). For clarity, a schematic representation of the unit cells of the $(1\bar{2}2)[41\bar{1}]$ and $(212)[10\bar{1}]$ twins is shown in **Fig. 6.8**, where some crystallographic relations to the zb-GaN matrix with (001)[110] orientation are indicated.

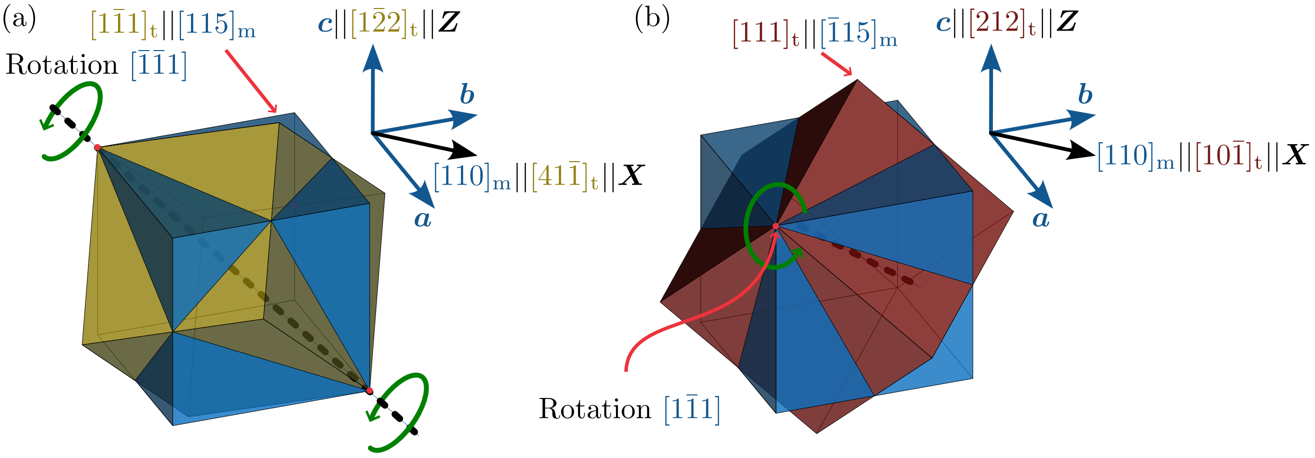

Fig. 6.8. Relations between the (a) $(1\bar{2}2)[41\bar{1}]$ and (b) $(212)[10\bar{1}]$ twins to the zb-GaN matrix. Parts of this figure are published in [156].

Once identified the origin of each reflection, the PF in **Fig. 6.7** show that sample **S2** produced the least amount of twins, denoted by the low-intensity reflections coming from them. In turn, samples **S3** and **S4** exhibited the highest amounts of twins. This suggests that a lower temperature during nucleation produces higher-quality, purer samples. Numerical results and a more detailed comparison is given in **Section 6.3.9**.

6.3.5 Simulated wurtzite pole figures

Similar to the 113_{zb} simulations, **Fig. 6.9** shows the predicted $10\bar{1}3_{\mathrm{wz}}$ angles in a PF. To adjust to the experimental results discussed in **Section 6.3.6**, however, initial rotations through 54.7° (angle between $[001]_{\mathrm{zb}}$ and $[111]_{\mathrm{zb}}$) were needed about $\pm\boldsymbol{b}$ of wurtzite GaN $(0001)[10\bar{1}0]$ and $(000\bar{1})[0100]$ crystals (note that $[0100] = \boldsymbol{b}$). The resulting PF with this rotations is shown in **Fig. 6.9(a)**. Furthermore, **Fig. 6.9(b)** shows the simulation where rotations through 15.8° (angle between $[001]_{\mathrm{zb}}$ and $[115]_{\mathrm{zb}}$) were employed.

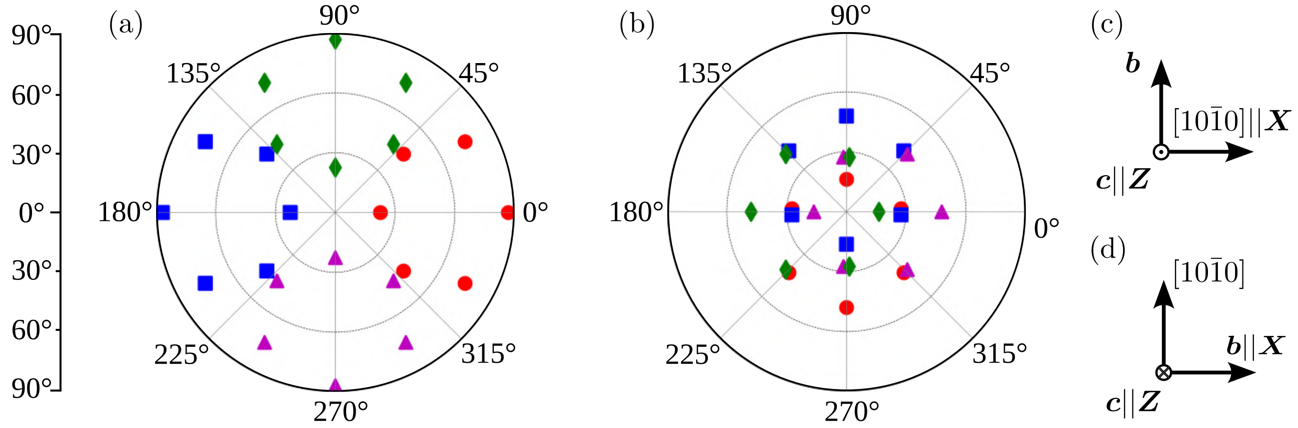

Fig. 6.9. Simulation of the $10\bar{1}3_{\mathrm{wz}}$ PF from wz-GaN with rotation (a) through 54.7° and: Miller indices $(0001)[10\bar{1}0]$ about $\boldsymbol{b}$ (red circles) and $-\boldsymbol{b}$ (blue squares); indices $(000\bar{1})[0100]$ about $\boldsymbol{b}$ (magenta triangles) and $-\boldsymbol{b}$ (green diamonds). Simulation with rotations (b) through 15.8° and: indices $(000\bar{1})[0100]$ about $\boldsymbol{b}$ (red circles) and $-\boldsymbol{b}$ (blue squares); indices $(0001)[10\bar{1}0]$ about $\boldsymbol{b}$ (magenta triangles) and $-\boldsymbol{b}$ (green diamonds). A vector representation is given for both orientations used for the simulations for (c) $(0001)[10\bar{1}0]$ and (d) $(000\bar{1})[0100]$. Parts of this figure are published in [156].

6.3.6 Experimental wurtzite pole figures

Looking at the experimental PF from the $\{10\bar{1}3\}_{\mathrm{wz}}$ family, various wurtzite inclusions may be identified in **Fig. 6.10**. The inclusions grown on well-oriented zb-GaN are shown in **Fig. 6.10(a)**, while **Fig. 6.10(b)** shows the same grown on twinned GaN for sample **S2**. Each of them show their characteristic 6-fold symmetry of the $\{10\bar{1}3\}$ family about the [0001] direction.

Since only inclusions along $\boldsymbol{X}$ are observed, it is likely that either Ga- or N-polar directions favor the formation of this kind of defects. As mentioned in **Section 3.2.3**, Ga-polar directions are a tad bit more prone to defects than the N-face, which would explain why this behavior is observed.

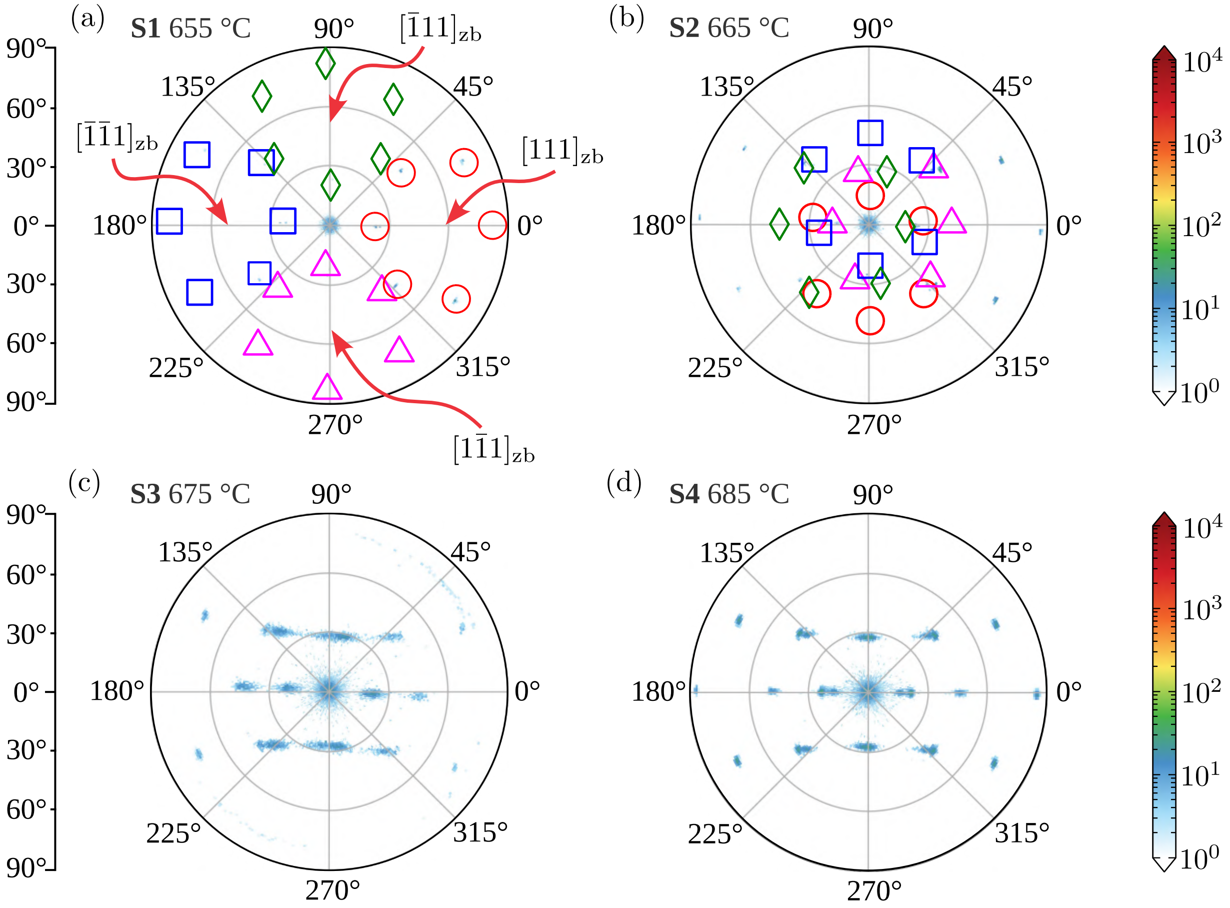

Fig. 6.10. Experimental PF from samples (a) **S1**, (b) **S2**, (c) **S3**, and (d) **S4**. In (a) and (b), the $10\bar{1}3_{wz}$ reflections are indicated with the same colors and shapes to match the rotations (through 54.7° and 15.8°) described for the calculation of the PF in **Fig. 6.9**. The nucleation temperatures are indicated.

The centers of these groups of reflections, i.e., the $\langle 0001\rangle_{wz}$ directions, lying 54.7° away from the surface normal indicate that the c-plane of wurtzite aligns with the $\{111\}$ zincblende faces. It is important to note that polarity plays a major role if a correct crystallographic relationship is to be established. Looking at **Fig. 2.1**, and more enlightening, **Fig. 2.2**, it becomes clear that the polarities of $[0001]_{wz}$ and $[111]_{zb}$ are the same, with bonds going from Ga to N in the stacking direction. However, this is not the case when comparing $[0001]_{wz}$ and $[\bar{1}11]_{zb}$.

While in the former the bonds go from Ga to N atoms, they go from N to Ga in the latter. Considering that the polarity of $[\bar{1}11]_{zb}$ goes from N to Ga (**Fig. 2.1**), it follows that $[0001]_{wz}||[111]_{zb}$ and $[000\bar{1}]_{wz}||[\bar{1}11]_{zb}$ (as well as $[0001]_{wz}||[\bar{1}\bar{1}1]_{zb}$ and $[000\bar{1}]_{wz}||[1\bar{1}1]_{zb}$ with similar reasoning). Because of this, it was necessary to use two different orientations in the simulation so that the correct $\langle 0001 \rangle$ could be aligned to the 4 corners of the zincblende unit cell, indicated in **Fig. 6.10(a)** with red arrows.

In turn, the *m*-planes, or $\{10\bar{1}0\}$, align with the $\{112\}_{\text{zb}}$ faces. As an example, for the wz-GaN growing along $[\bar{1}\bar{1}1]_{\text{zb}}$—red circles in **Fig. 6.10(a)**—, the relation $[\bar{1}010]_{\text{wz}}||[\bar{1}\bar{1}\bar{2}]_{\text{zb}}$ is found. Additionally, the inclusion growing in the $[111]_{\text{zb}}$ direction have the relation $[10\bar{1}0]_{\text{wz}}||[11\bar{2}]_{\text{zb}}$, as seen as well in **Fig. 2.2**.

Recalling that some twinned $\{111\}_{\text{t}}$ faces are parallel to the well-oriented $\{115\}_{\text{zb}}$ planes, and that the latter are 15.8° tilted from the $[001]_{\text{zb}}$surface, it follows that the reflections indicated in **Fig. 6.10(b)** (where rotations through 15.8° were added) come from wurtzite inclusions growing on twinned zb-GaN. These inclusions inherit the relation $[0001]_{\text{wz}}||[115]_{\text{zb}}$. This means that, just like the twinned 111_{zb} planes, misoriented $[000\bar{1}]_{\text{wz}}$ grown on twins could also be contributing to the reflection at 34.5° in **Fig. 6.5**.

Regarding the amount of wurtzite inclusions, it is noteworthy that sample **S2** presented the lowest amount of wurtzite inclusions. Conversely, samples **S3** and **S4** presented the highest amounts of inclusions. Moreover, the inclusions in these two samples seem to have been grown preferably on the twinned zb-GaN, since the reflections coming from them are more intense.

6.3.7 Crystallographic relations

Throughout **Section 6.3.4** and **Section 6.3.6**, some crystallographic relations between zincblende and wurtzite GaN as well as their twins have been given. Graphical representations of their unit cells are shown in **Fig. 6.11(a)**, where some of these relations are also indicated. In this diagram, these crystallographic relations are much clearer. For example, the angle between $[111]_{\text{zb}}$ and $[0001]_{\text{wz}}$ of $\sim 54.7°$ is somewhat more appreciable there. Furthermore, the twinned zb-GaN and the wz-GaN growing on top also show how their $\{111\}_{\text{t}}$ and $\{0001\}_{\text{t}}$ planes are aligned close to the surface. The $\boldsymbol{Z}$ and $\boldsymbol{X}$ directions are given for all the unit cells shown.

The atomistic view along $[\bar{1}10]_{\text{zb}}$ in **Fig. 6.11(b)** shows these relations from a different perspective. In there, the $(0001)_{\text{wz}}||(111)_{\text{zb}}$ interface between the matrix zb-GaN and wz-GaN, with indices $(\bar{3}034)[30\bar{3}8]$, growing directly onto it is straightforward to distinguish matching the polarities of both sides. The same goes for the $(111)_{\text{t}}||(\bar{1}\bar{1}1)_{\text{m}}$ interface between zb-GaN and one of its twins with MIller indices $(22\bar{1})[\bar{1}\bar{1}\bar{4}]$, and the $(000\bar{1})_{\text{t}}||(11\bar{1})_{\text{t}}$ interface between twinned zb-GaN and wz-GaN growing on it with indices $(10\bar{1}\bar{7})[\bar{2}02\bar{1}]$. The planes normal and perpendicular to the surface, i.e., the ones defining the ideal orientations, are shown for the 4 domains.

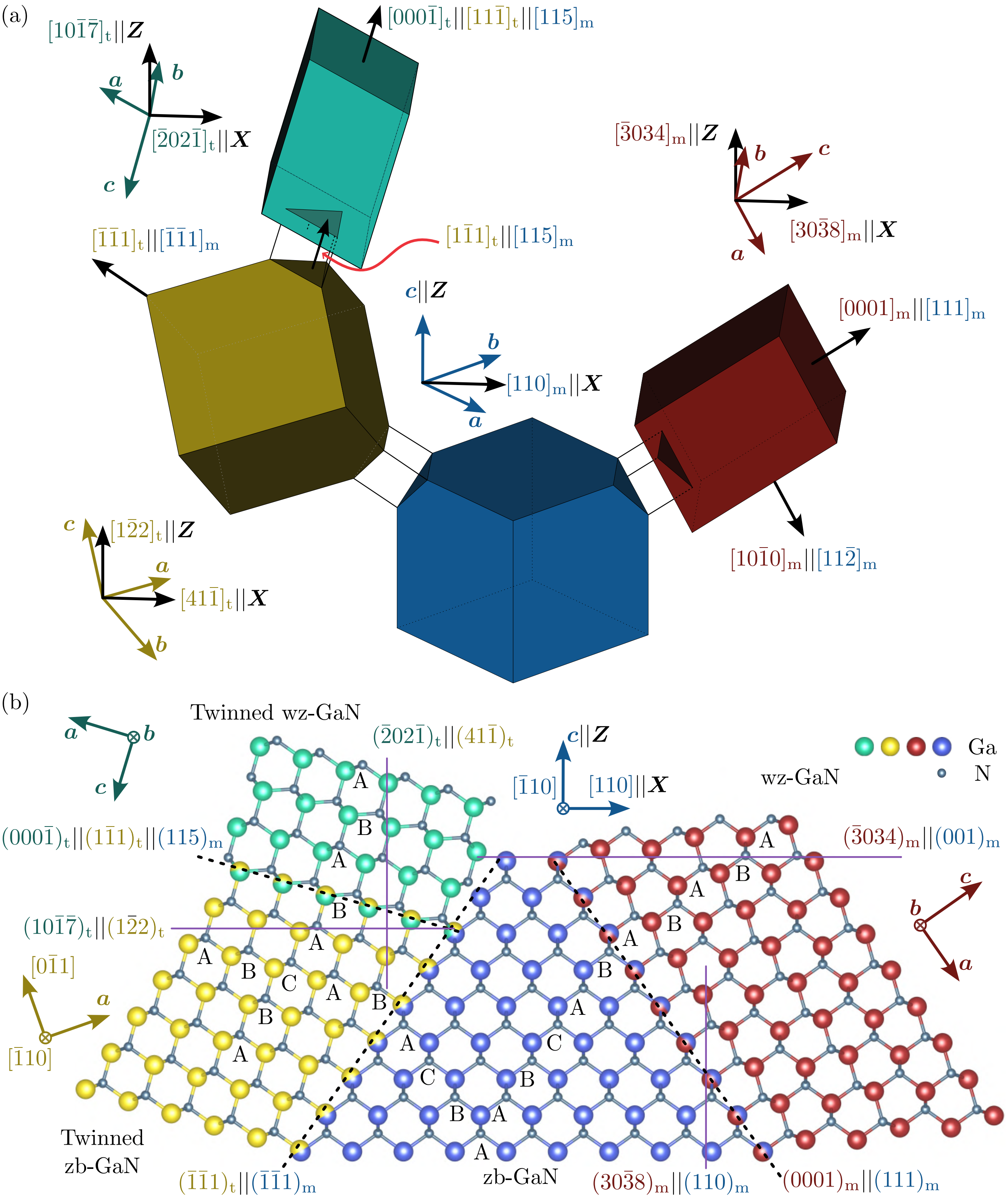

Fig. 6.11. (a) graphical representation and (b) atomistic along $[\bar{1}10]_{zb}$. In blue Ga atoms: matrix zb-GaN (three indices with subindex "m"); red: wz-GaN grown on the matrix zb-GaN (four indices with subindex "m"); yellow: twinned zb-GaN (three indices with subindex "t"); cyan: wz-GaN grown on twinned zb-GaN (four indices with subindex "t").

Moreover, as mentioned multiple times, it is clear that these two types of defects grow on top of the {111} faces of zb-GaN. This is because of the similarities between the $\langle 111\rangle_{\mathrm{zb}}$ and $\langle 0001\rangle_{\mathrm{wz}}$ directions, where only the stacking sequence differs from one phase to the other. Hence, stacking faults are the main factor to consider when analyzing the contamination of zb-GaN by wz-GaN and their twins. The atomistic view in **Fig. 6.11(b)** also depicts these defects.

For example, starting in the zb-GaN zone in the center, one can easily follow the stacking direction along the diagonally-placed [111] axis. There, the ABCABCABC (see **Fig. 2.2** for more details) stacking sequence of zincblende change into wurtzite's ABABAB, leading to the wz-GaN inclusion. Similarly, going from the zb-GaN matrix to the twin located to the left, now the stacking goes from ABCABCABC to ACBACBACB of the twinned zincblende (as described in **Section 6.3.4** as well). From there, going up into the twinned wz-GaN zone, the stacking changes again from ABCABCABC to ABABAB, exactly as in the matrix.

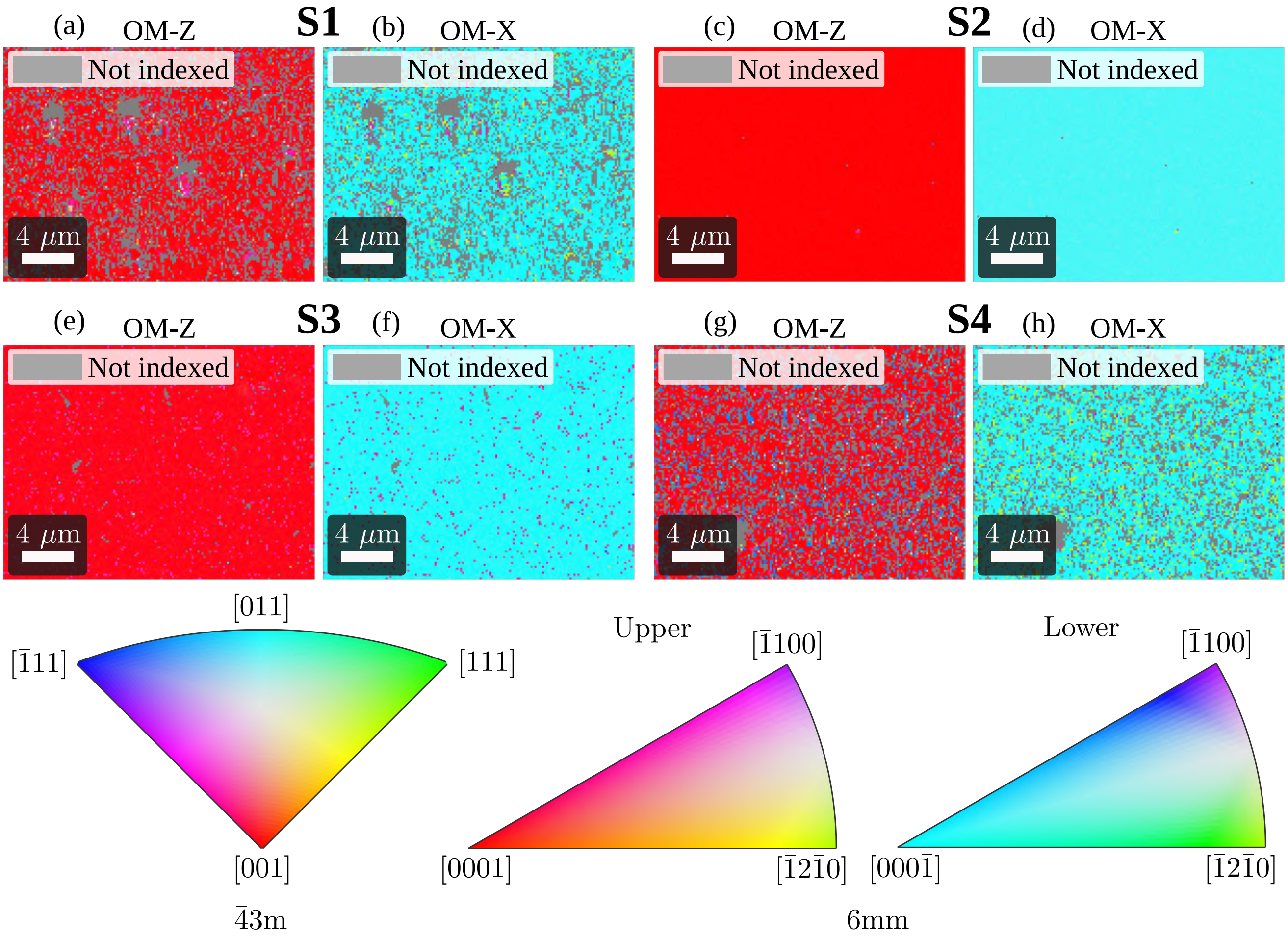

Fig. 6.12. EBSD ***Z*** and ***X*** orientation maps (OM) from series **S**. On the bottom, the IPF keys for point groups $\bar{4}3m$ and 6mm are shown. For the latter, both the upper and lower keys are shown as suggested by Nolze and Hielscher [157].

6.3.8 EBSD characterization

The orientation of the samples discussed so far may be also analyzed via EBSD. For that end, **Fig. 6.12** shows the orientation maps along $\boldsymbol{Z}$ and $\boldsymbol{X}$. The dominating red color (representing $[001]_{\mathrm{zb}}$ or $[0001]_{\mathrm{wz}}$) along $\boldsymbol{Z}$ suggests that the main orientation of zb-GaN out-of-plane was perpendicular to the 001_{zb} planes, considering only zincblende (for reasons that will become clearer in **Section 6.3.9**).

Furthermore, the widespread cyan coloring—representing $[011]_{\mathrm{zb}}$ or $[000\bar{1}]_{\mathrm{wz}}$—in the maps along $\boldsymbol{X}$ indicates that zb-GaN has the {110} planes aligned perpendicular to the in-plane direction. This reveals then the (001)[110] ideal orientation of zb-GaN, in perfect agreement with the XRD discussion thus far. This orientation is confirmed by the IPF shown in **Fig. 6.13**. For all samples, there is a high density of orientations toward the $[001]_{\mathrm{zb}}$ along $\boldsymbol{Z}$. The same case goes for the IPF along $\boldsymbol{X}$, where the highest densities of orientations are found near the $[011]_{\mathrm{zb}}$ (not explicitly indicated) zone of the IPF.

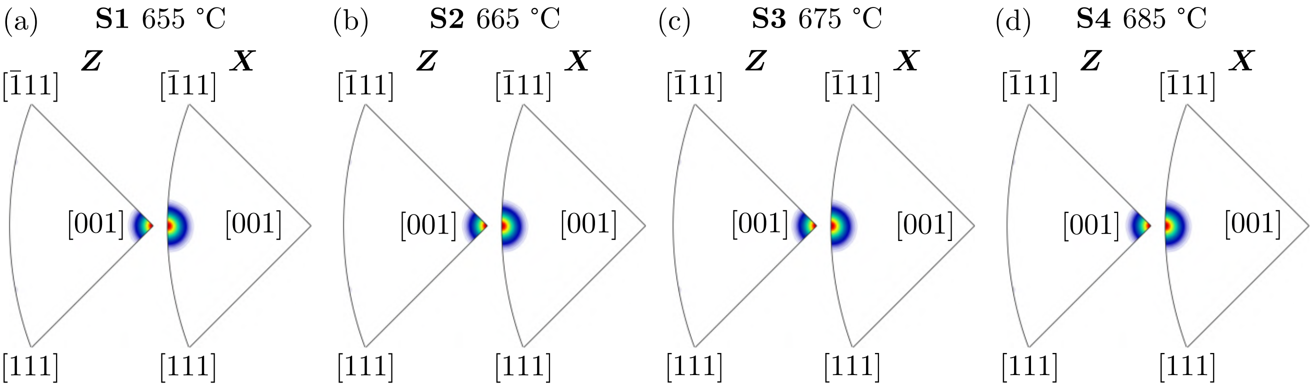

Fig. 6.13. EBSD inverse PF obtained from the orientation maps in **Fig. 6.12** for samples (a) **S1**, (b) **S2**, (c) **S3**, and (d) **S4**. The nucleation temperatures are indicated.

Moreover, the orientation maps also indicate the degree of orientation; while sample **S2** exhibits a significantly more homogeneous coloring in both maps, samples **S4**, **S3**, and **S1** display different shades of various colors. This means that the latter samples presented an importantly greater degree of misorientation. Conversely sample **S2** seems to have grown very nicely oriented. Looking at the 113_{zb} and $10\bar{1}3_{\mathrm{wz}}$ EBSD PF in **Fig. 6.14**, obtained through the ODF, this is more detailed. In most of the samples, the poles from zb-GaN twins are not detected. Only sample **S3** shows these reflections, suggesting a higher amount of twins. On the other hand, samples **S1**, **S3**, and **S4** show clear signals of wurtzite inclusions, with samples **S1** and **S3** showing even the wz-GaN twins. The EBSD $10\bar{1}3_{\mathrm{wz}}$ PF of sample **S2** may be counterintuitive even, since the wurtzite inclusions do not seem to have order. Instead, the reason for this may be that EBSD detected so little amount of wz-GaN that it was not enough to obtain a clear orientation for it.

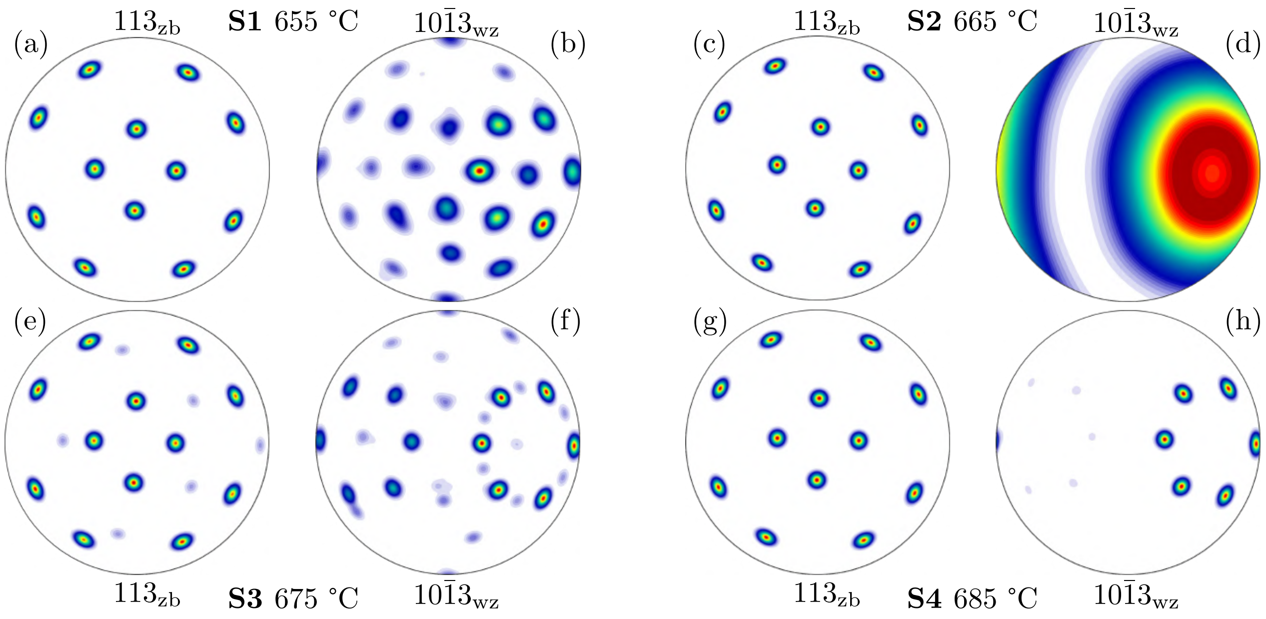

Fig. 6.14. EBSD 113_{zb} and $10\bar{1}3_{wz}$ PF from samples (a)-(b) **S1**, (c)-(d) **S2**, (e)-(f) **S3**, and (g)-(h) **S4**. The nucleation temperatures are indicated.

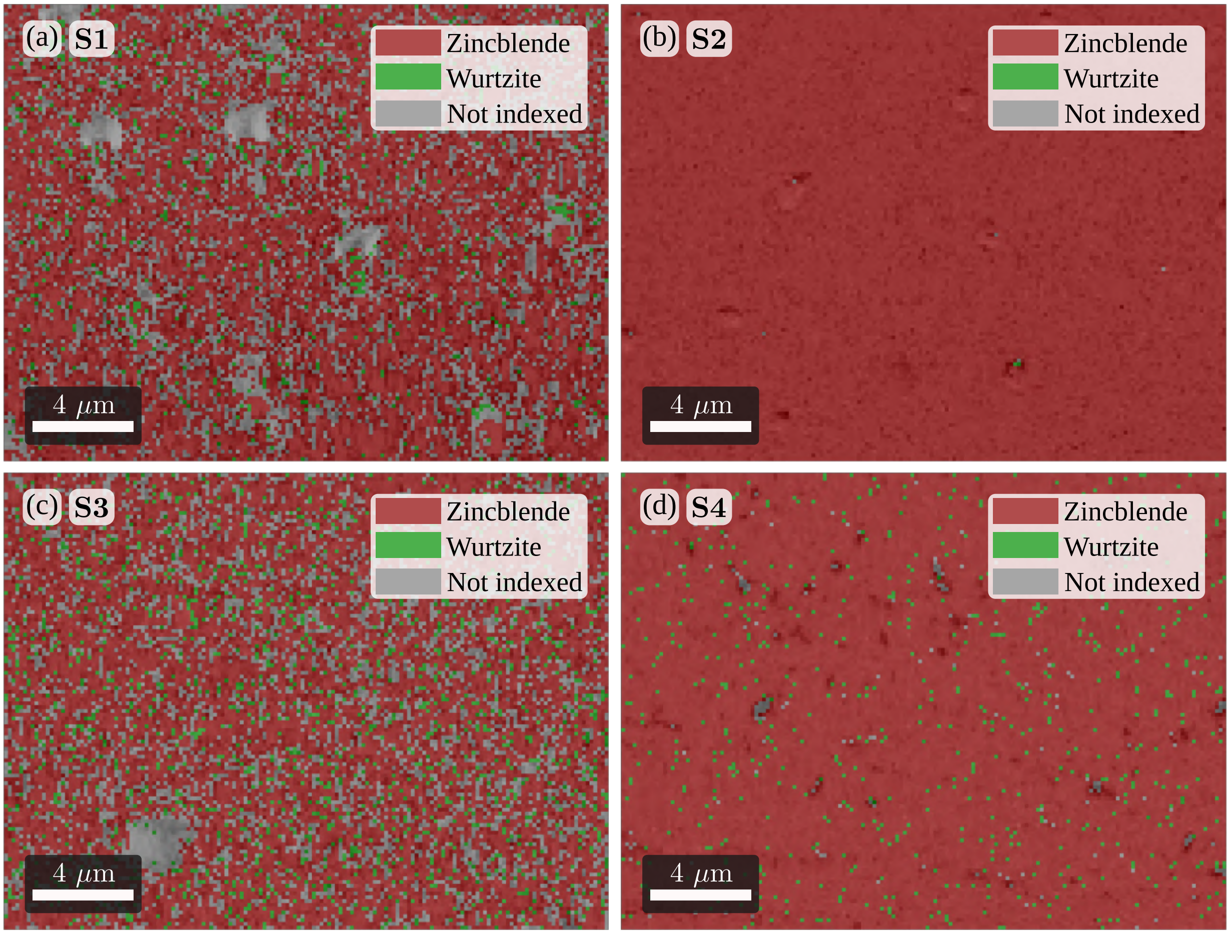

Fig. 6.15. EBSD phase maps from samples (a) **S1** (b) **S2**, (c) **S3**, and (d) **S4**.

6.3.9 Quantitative results

Table 6.2 shows the zincblende and untwinned zincblende content calculated from the XRD PF, the zincblende content from the EBSD phase maps from **Fig. 6.15** (obtained via MTEX), the rocking-curve FWHM from the ω scans, and the RMS-roughness from AFM. For easier interpretation, the data from **Table 6.2** is plotted in **Fig. 6.16** as function of nucleation temperature.

Table 6.2. Results from the figures-of-merit used for samples **S**. For the XRD PF calculations (first two columns), only the 113_{zb} reflections from the well-oriented zb-GaN, as indicated in **Fig. 6.7(a)** were considered for the integrated intensity calculation with **Eq. (4.21)**, while the complete $10\bar{1}3_{\mathrm{wz}}$ PF were used for wurtzite. The reported values are the average ± the standard error, when multiple measurements were taken. For EBSD data, numbers inside parenthesis indicate the percentage of unindexed area.

	Zincblende content/%	Untwinned content/%	EBSD zincblende content/%	FWHM/arcmin	RMS-roughness/nm
S1	98.4 ± 0.6	97.8 ± 0.7	95.1 (28.9)	125.4 ± 2.5	5.4 ± 1.4
S2	99.6 ± 0.3	99.7 ± 0.3	99.9 (0.1)	83.4 ± 0.8	5.7 ± 0.6
S3	81.8 ± 2.4	85.4 ± 2.1	89.4 (23.9)	147.0 ± 4.5	6.4 ± 1.3
S4	60.0 ± 3.6	71.0 ± 3.3	96.6 (1.0)	145.8 ± 4.0	6.4 ± 1.1

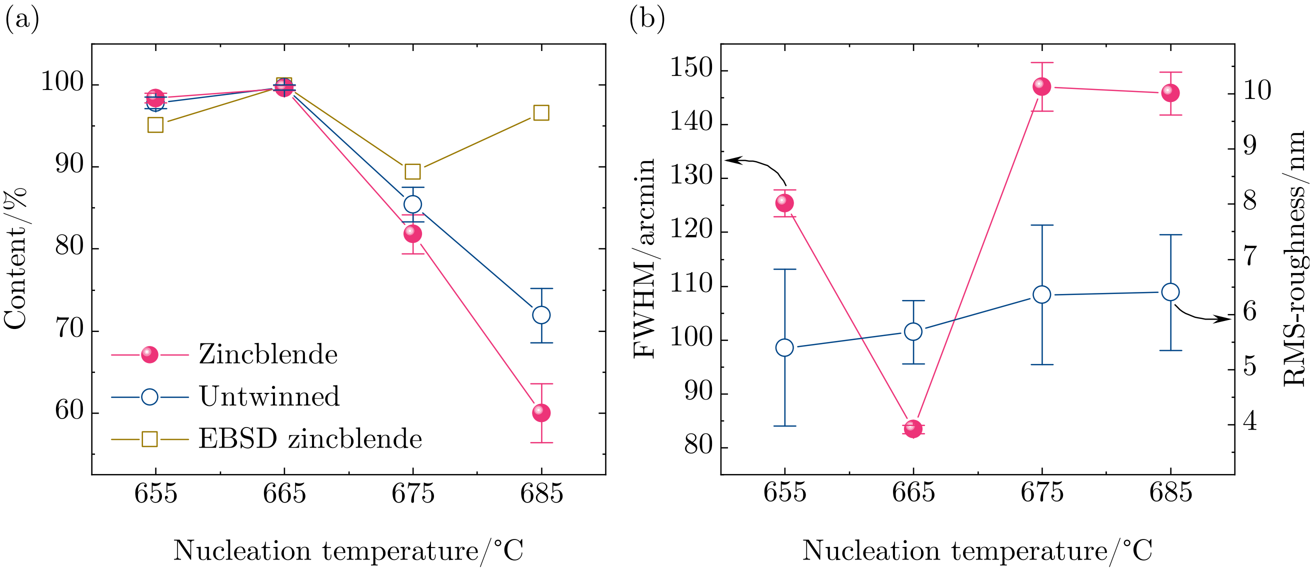

Fig. 6.16. For sample series **S**, (a) zincblende and untwinned zincblende contents from XRD PF and EBSD phase maps, as well as (b) FWHM of the 002_{zb} reflection and RMS-roughness from $10 \times 10\ \mu\mathrm{m}^2$ AFM scans.

First, the zincblende and untwinned contents in **Fig. 6.16(a)** confirm the qualitative conclusions so far; the best sample in terms of crystalline phase purity is sample **S2**, being grown at a nucleation temperature of 665 °C. Moreover, a tendency is seen in almost all figures-of-merit used in this work. Crystalline purity, as measured by XRD PF, for example, starts at a high value of 98.4 % and grows a small amount to $\sim$ 99.6 % as nucleation temperature goes from 655 to 665 °C. However, as it increases further to 675 °C, zincblende content significantly drops to $\sim$ 81.8 %. This trend continues as the nucleation temperature reaches its maximum of 685 °C, with a crystalline purity as low as $\sim$ 60.0 %. The same trend is identified for the amount of untwinned content, decreasing dramatically for the highest temperatures. This is not exactly the case for the zincblende content from EBSD phase maps, where the highest nucleation temperature yielded a remarkable $\sim$ 96.6 %.

Very similarly, the trend in surface quality, as suggested by roughness values in **Fig. 6.16(b)**, indicates that the lower the temperature, the flatter, higher-quality surface achieved. Nevertheless, the crystalline quality, denoted by the FWHM of the 002_{zb} reflection (see **Section 4.2.2**), does not follow this trend exactly as the surface quality. Rather, the crystalline quality starts decreasing to a minimum for sample **S2** grown at 665 °C. Then, it increases again and almost flattens for the two highest temperatures. Moreover, from the EBSD phase maps, one can gain some insight into the quality of the films by means of the unindexed percentage: the higher this value, the lower the quality, since this produces less clear diffraction patterns, harder to index. The remarkable small amount of unindexed surface in sample **S2**, once again suggests that this very sample exhibits the highest quality. On the other hand, the high unindexed percentages displayed by samples **S1** and **S3** suggest low qualities according to EBSD. Up to this point, there is a good agreement between EBSD and XRD, with sample **S4** being the exception.

It is likely that the reason behind this important changes of the figures-of-merit across the different samples was due to changes in nucleation modes due to the various temperatures used. This could be arising from changes in adatom mobility, rising as temperature increases due to the higher thermal energy provided. With this, it is safe to assume that the lower mobilities promoted by the 655 and 665 °C in samples **S1** and **S2** yielded a higher density of smaller nuclei when compared to 675 and 685 °C. The results of this work show that nucleation at 665 °C produced small enough nuclei so that dislocations, generated due to relaxation, glided out from them and annihilated when various nuclei coalesced (see **Section 3.2.3**). In contrast, the bigger, lower density nuclei at higher temperatures in samples **S3** and **S4** suffered from greater amount of dislocations, and hence tilt (see **Fig. 4.7**), leading to misorientations with subsequent twinning and wurtzite formation. It is noteworthy that lowering temperature to 655 °C likely resulted in mobility decreasing more than enough, rendering slightly worse purity and quality, suggesting that the optimal temperature was 665 °C.

Chapter 7: Growth Stoichiometry of Mg-doped zb-GaN Epilayers

7.1 Growth

7.1.1 Growth conditions

Two groups (series **G** and **N**) of Mg-doped zb-GaN thin films where prepared on GaAs (001) substrates in the Riber C21 molecular beam epitaxy (MBE) system described for series **S** in **Section 6.1.1** in order to investigate the effects of *p*-type doping on the structure of zb-GaN thin films on GaAs (001) substrates.

Just as for series **S** the growth process of the structures shown in **Fig. 7.1** started by transferring the GaAs (001) substrates into the growth chamber of the MBE. There, they were heated up to 585 °C in 20 minutes for desorption. The As shutter was opened at a beam equivalent pressure (BEP) of 7.59×10^{-6} Torr (at a cell temperature of 137 °C) as the substrate temperature went past 380 °C in order to prevent GaAs decomposition. The process was controlled by the GaAs 2×4 surface reconstruction with reflection high-energy electron diffraction.

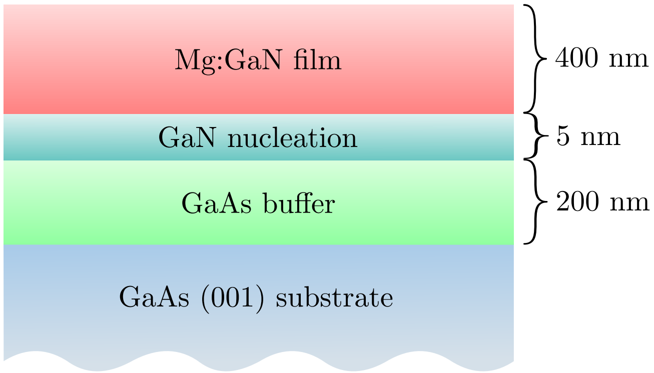

Fig. 7.1. Structure of the doped samples grown for series **N** and **G**.

Once again, the process continued with the growth of a 200 nm thick GaAs homoepitaxial layer on top of the reconstructed substrate at a temperature of 690 °C. For this, the Ga shutter was opened at a BEP_{Ga} of 2.58×10^{-7} Torr (cell temperature of 941 °C) and maintained open with the As shutter for 15 minutes.

Right after, the substrate temperature was raised to 665 °C (as in sample **S2**), while the radio-frequency (RF) plasma source was ignited at 100 (**G**) or 150 W (**N**) and a N_2 flux of 0.4 sccm. To start the growth of the nucleation layer, the Ga shutter was opened first using a $\mathrm{BEP}_{\mathrm{Ga}}$ of 1.95×10^{-7} Torr (cell temperature of 929 °C). Only 3 seconds later, the N shutter was also opened. During the first 30 seconds of the nucleation layer, the growth took place under an As overpressure (see **Section 3.2.3**) using the same $\mathrm{BEP}_{\mathrm{As}}$ as in the previous layer.

After 90 seconds since the start of the nucleation layer, the substrate temperature was raised to 700 °C, while maintaining the Ga and N shutters open. At that temperature, the Mg cell was opened at various T_{Mg} as shown in **Table 7.1** for 110 minutes for a total of ∼ 400 nm of nominal thickness. A schematic of the growth procedure is shown in **Fig. 7.2**, indicating at what times are the cells opened/closed.

Table 7.1. Mg cell temperature and RF-plasma power used for series **G** and **N**.

Sample	Plasma power/W	T_{Mg}/°C
G1	100	360
G2	100	380
G3	100	400
N1	150	360
N2	150	380
N3	150	400

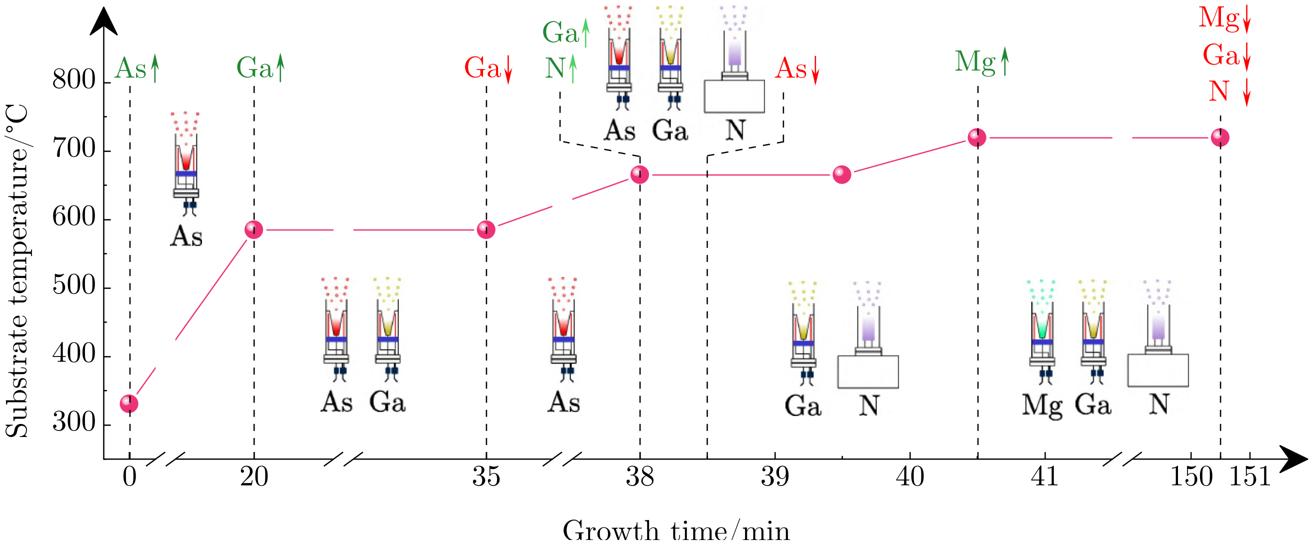

Fig. 7.2. Temperature during growth. Green (red) remarks with upward (downward) arrows indicate when a cell was opened (closed).

7.2 Characterization

7.2.1 Morphology and crystallinity

The surface and crystallinity of samples **G** and **N** was characterized in the exact same manner as samples **S**. For a detailed description on x-ray diffraction (XRD), atomic force microscopy (AFM), scanning electron microscopy (SEM), Nomarski, and electron backscatter diffraction (EBSD), as well as how the full-width at half-maximum (FWHM) and root mean square (RMS) values are obtained, the reader is referred to **Section 6.2.1** and **Section 6.2.2**. Additionally, sample **G2** underwent energy-dispersive x-ray spectroscopy (EDX) to analyze possible Ga droplets.

7.2.2 Mg content

To evaluate composition, samples **G** and **N** were measured via Secondary-ion mass spectrometry (SIMS) in a TOF-SIMS-V from IONTOF. This equipment uses a Bi_3+ ion current of 0.3 pA accelerated at 30 kV in a pulsed manner.

For depth profiling, O_2^+ (120 nA, 1 kV) and Cs^+ (170 nA, 2 kV) ions were used to sputter the sample. Ions $CsGa^+$, $CsMg^+$, Cs_2As^+, and Cs_2N^+ were used to record the intensities of Ga, Mg, As, and N, respectively, in order to diminish the matrix effect.

Finally, Hall-effect measurements were conducted at room temperature to obtain the amount of electrically active Mg atoms in the films. For that, an in-house made system was used, equipped with Nd magnets producing a magnetic field of 0.55 T. Square pieces of $\sim 10 \times 10$ mm^2 were used with circular Au/Ni contacts evaporated at the corners.

7.3 Results and discussion

7.3.1 Morphology

Fig. 7.3 shows the Nomarski, SEM, and AFM micrographs from samples **G**. On the other hand, **Fig. 7.4** shows the same measurements obtained from samples **N**. A clear difference can be noted between the two types of samples observing their surface morphologies.

First, Normarski images reveal the dense presence of droplet-like features across the whole surface of samples **G**. Conversely, the surface of samples **N** seems much cleaner from these features. A similar picture is seen in the SEM micrographs, particularly for samples **G1** and

G2. Moreover, these measurements reveal a smooth, low-pit density surface in between these droplets when compared to samples **N**, where a highly pitted surface arised likely from the growth conditions. This is confirmed by the uniform colors in areas without droplets in the AFM images in samples **G** and the grainy appearance of the whole surface of samples **N**.

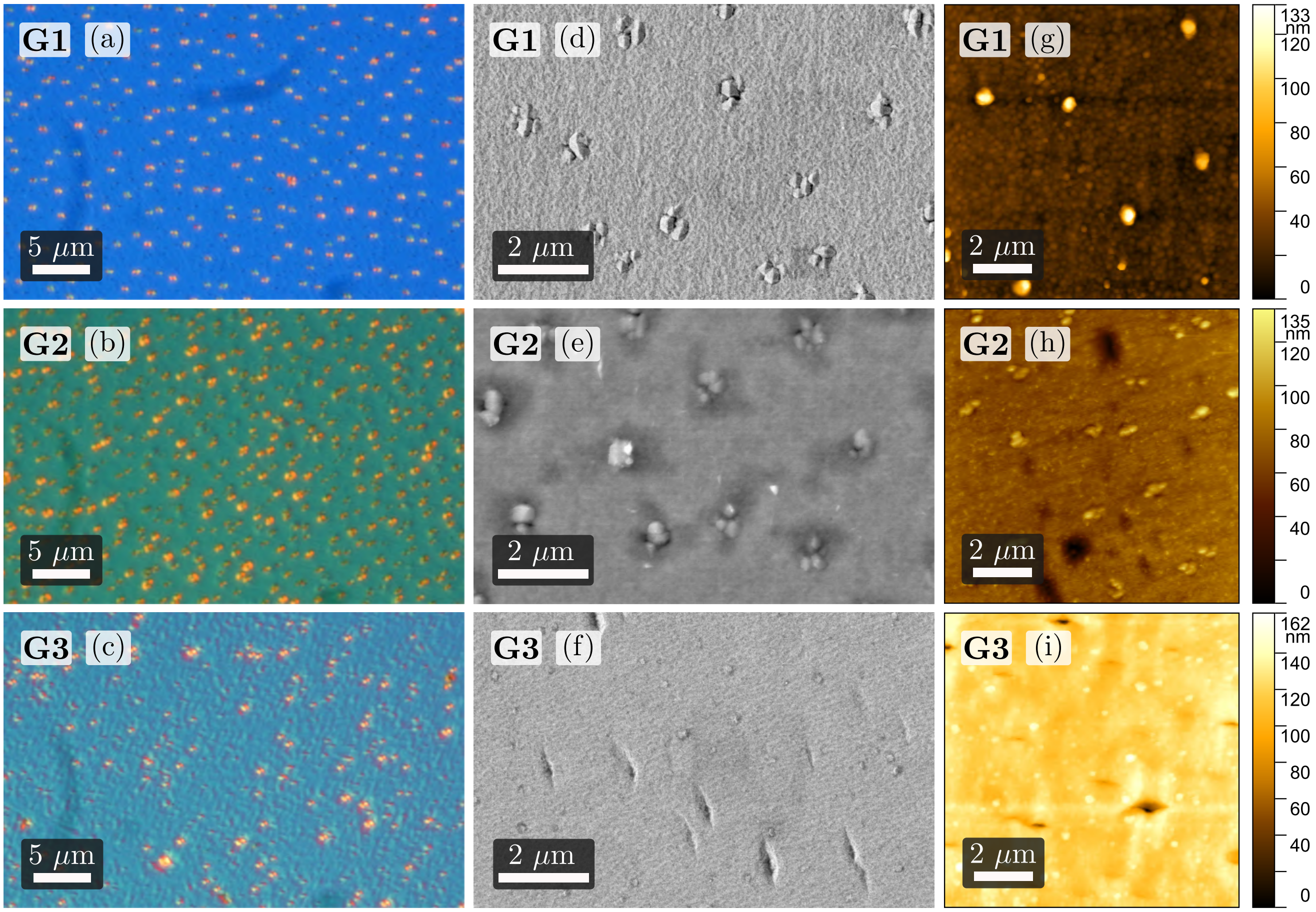

Fig. 7.3. (a)-(c) Nomraski, (d)-(f) SEM, and (g)-(i) AFM micrographs from samples **G**. Parts of this figure are published in [156].

Comparing the surface morphology between the two types of samples, a reasonable assumption can be made about the stoichiometry. That is, the lower power of 100 W used for igniting the N plasma in samples **G** led to a smaller amount of nitrogen reactive species, pushing the Ga/N ratio towards Ga-rich conditions in fashion that provoked the accumulation of Ga on the surface.

Because of this very same reason, the higher adatom mobility resulted in smoother surfaces with low amounts of pits. Conversely, the 150 W used for the plasma source in samples **N** generated enough reactive N species to keep the Ga/N ratio within the N-stabilized regime observed as well in samples **S** (see **Fig. 6.4**), for which the same RF power was used.

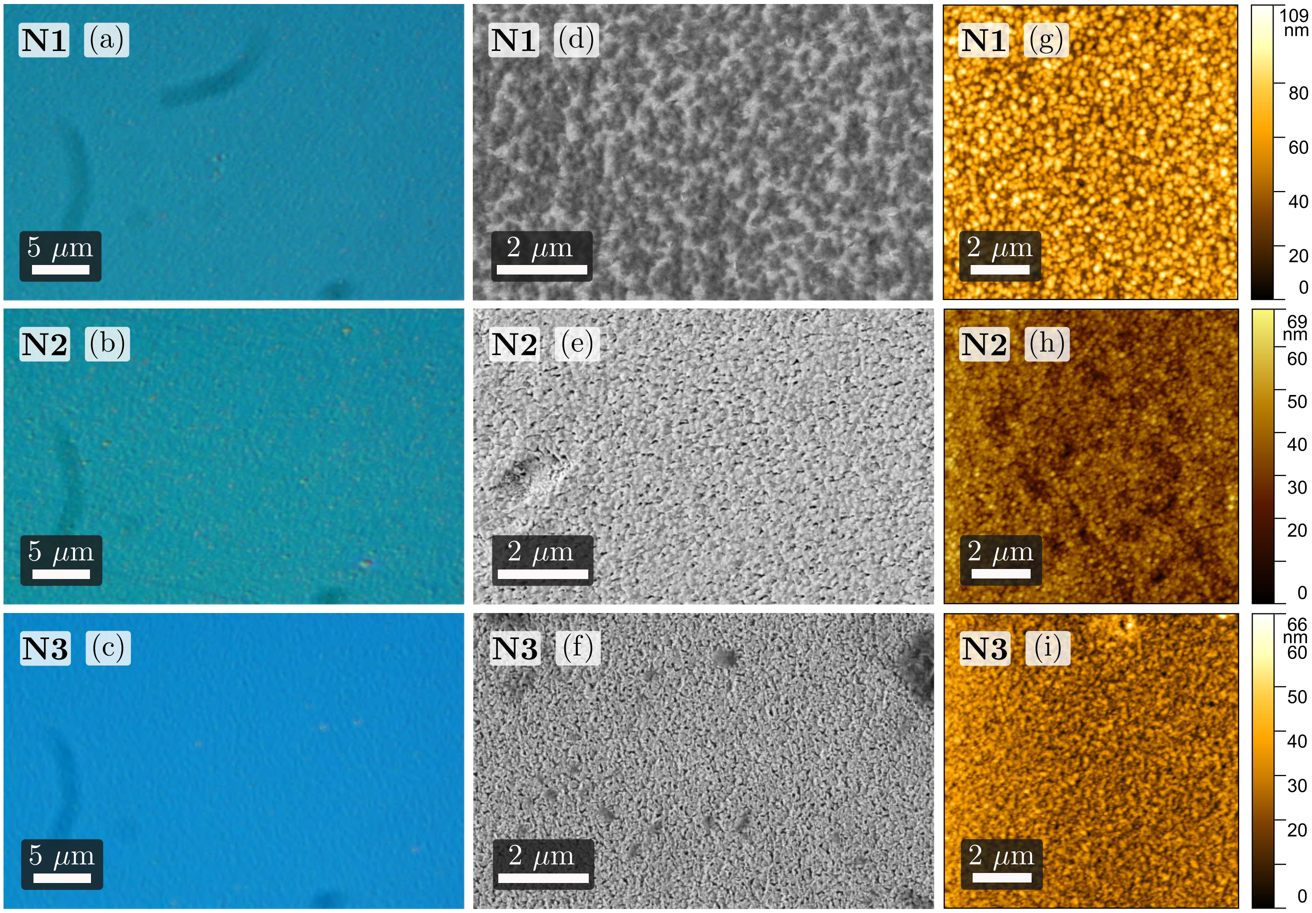

Fig. 7.4. (a)-(c) Nomraski, (d)-(f) SEM, and (g)-(i) AFM micrographs from samples **N**. Parts of this figure are published in [156].

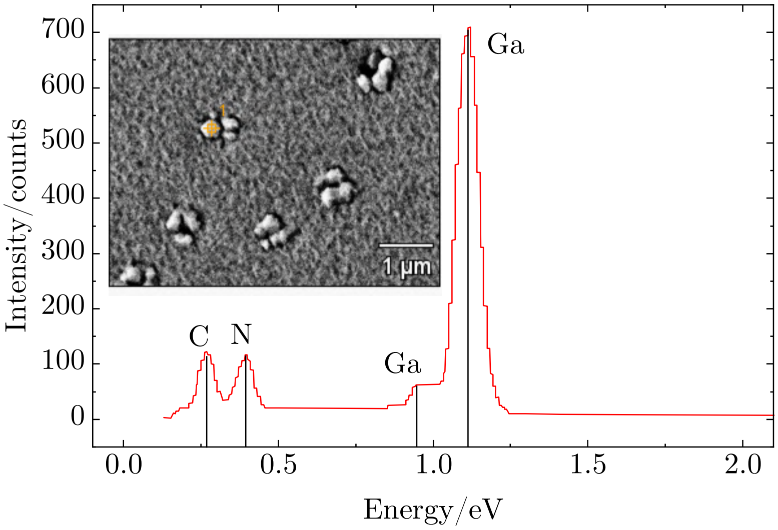

Fig. 7.5. EDX analysis carried out on a droplet as indicated in the inserted image.

To have more certainty about this assumption, Fig. 7.5 shows the results obtained from EDX, which revealed a ∼ 80/20 Ga to N ratio within the droplets, compared to the near 50/50 obtained in some areas outside them. These results support the idea that 100 W at the plasma source was enough to push the conditions well within the Ga-droplet regime.

7.3.2 Out-of-plane orientation

The appearance of the 002_{zb} and 004_{zb} reflections in the symmetric ω-2θ scans in Fig. 7.6 are a clear indication the $(001)_{\mathrm{zb}}$ planes oriented parallel to the surface, following the orientation given by the substrate so that $(001)_{\mathrm{zb}}||(001)$ GaAs.

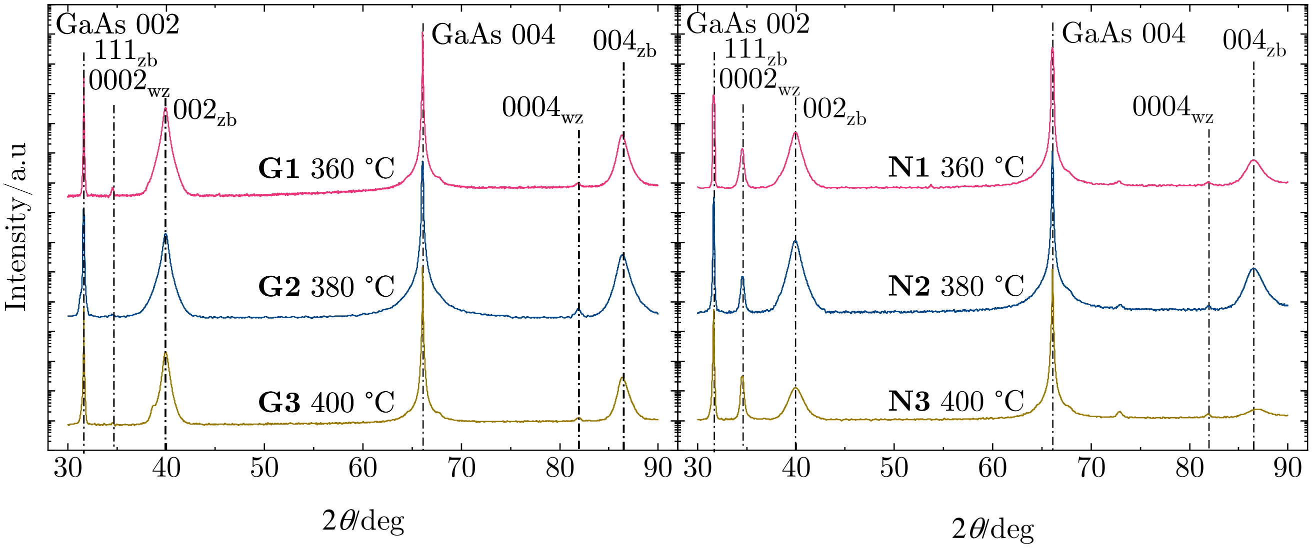

Fig. 7.6. XRD ω-2θ scans from samples **G** and **N**. Reflections belong to zincblende and wurtzite GaN, unless otherwise stated. Parts of this figure are published in [156].

Furthermore, the reflection at ∼ 34.5° indicates the formation of $(111)_{\mathrm{zb}}$ or $(0001)_{\mathrm{wz}}$ domains. These scans also show a profound variation between the two sample series. On the one hand, samples **N** exhibit an intense, unwanted peak at ∼ 34.5°. Conversely, these samples also show weaker 004_{zb} reflections. Samples **G**, on the other hand, display a negligible $111_{\mathrm{zb}}/0002_{\mathrm{wz}}$ and a stronger 004_{zb} reflection.

7.3.3 Experimental zincblende pole figures

For a complete description of orientation of the samples, Fig. 7.7 shows the results of the pole figure (PF) measurements obtained from samples **G** and **N**. Just as for samples **S**, the simulated PF of the 113_{zb} reflection from GaN (001)[001] is superimposed on the experimental PF measured from sample **G1** and is shown in Fig. 7.7(a).

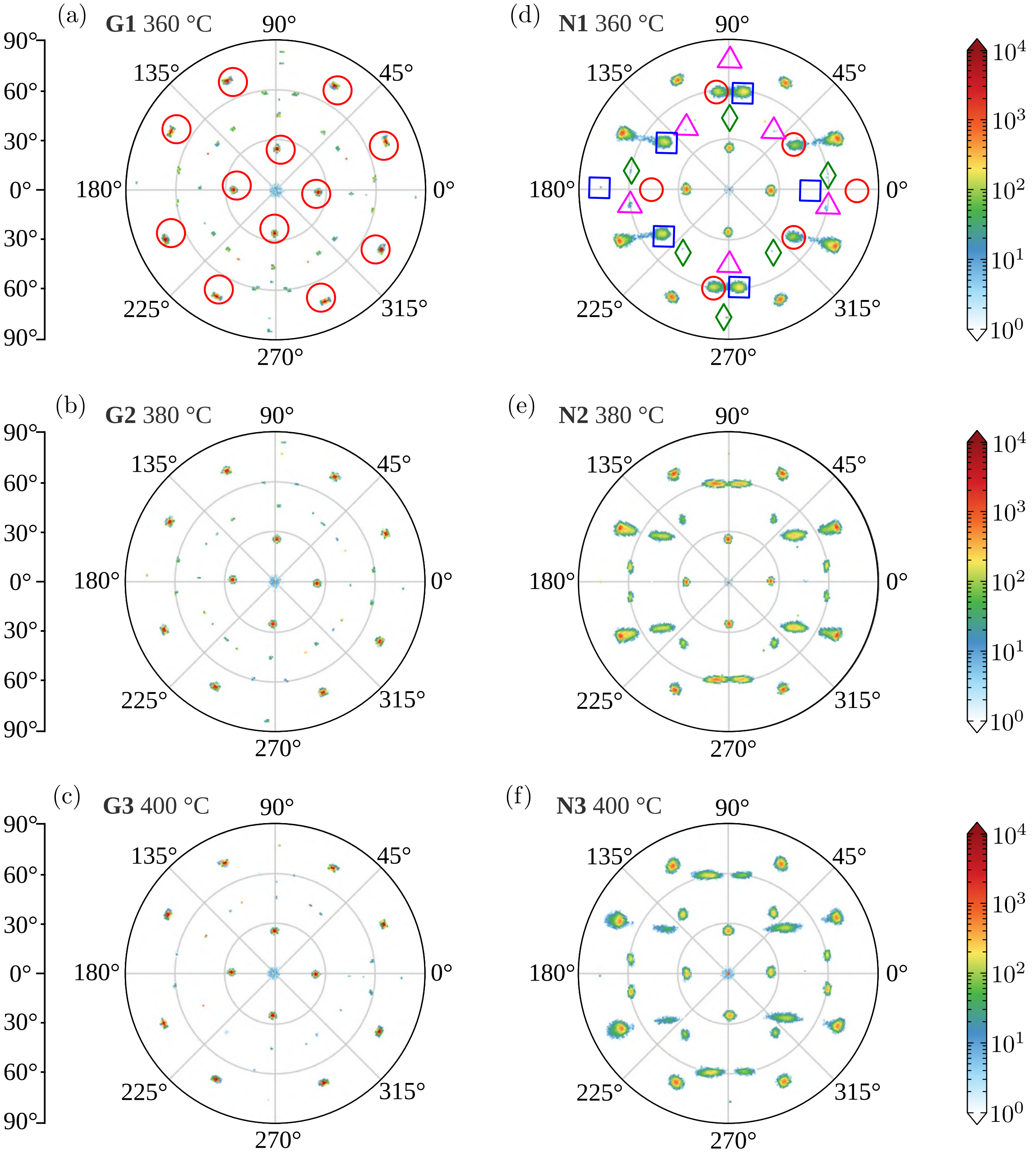

Fig. 7.7. Experimental 113_{zb} PF of samples **G** and **N** with simulation from GaN (001)[110] superimposed on the results from sample **G1** in (a). Twinned 113_{zb} reflections are indicated for sample **N1** in (d). Mg cell temperatures are indicated. Parts of this figure are published in [156].

Again, the 12 visible reflections from the $\{113\}_{\mathrm{zb}}$ family are clearly identified in all PF vert close to the prediction from the simulation, confirming the $(110)_{\mathrm{zb}}||(110)_{\mathrm{GaAs}}$ in-plane relation. This means that the final orientation of the zb-GaN samples is described by the Miller indices (001)[110], corroborating the successful epitaxial growth of the films on GaAs substrates. Moreover, 6 of the 12 visible reflections coming from the GaN $(\bar{1}22)[411]$, $(1\bar{2}2)[41\bar{1}]$, $(\bar{2}\bar{1}2)[101]$ and $(212)[10\bar{1}]$ twins (see **Section 6.3.4**) are indicated for sample **N1** in **Fig. 7.7(d)**. The same reflections can be identified for the rest of the samples to various extents. For details on the simulation, the reader is referred to **Section 6.3.3** and **Fig. 6.6**. Additionally, **Fig. 6.8** shows the crystallographic relations between zb-GaN and some of its twins.

The 113_{zb} PF measurements significantly differentiate between samples **G** and **N**. In the first place, the former group exhibits strong, sharp reflections coming from untwinned zb-GaN. Furthermore, the twinned reflections are remarkably weak in comparison to their untwinned counterparts. On the other hand, samples **N** displayed much broader untwinned and more intense twinned reflections, meaning that the degree of misorientation and the amount of twins was significantly greater in samples **N** than **G**.

7.3.4 Experimental wurtzite pole figures

The results from the XRD $10\bar{1}3_{\mathrm{wz}}$ PF measurements are shown in **Fig. 7.8**. The simulated $10\bar{1}3_{\mathrm{wz}}$ reflections obtained from GaN $(0001)[10\bar{1}0]$ and $(000\bar{1})[0100]$ with rotations through 54.7° about $\boldsymbol{b}$ and $-\boldsymbol{b}$ are superposed on the experimental PF in **Fig. 7.8(a)**.

Unlike samples **S**—in **Fig. 6.10**—, where only 2 wurtzite inclusions (along $\boldsymbol{X}$) are seen, most **G** and **N** samples exhibit 4 (along $\boldsymbol{X}$ and $\boldsymbol{Y}$). As mentioned in **Section 3.2.3**, different polarities can lead to different amounts of defects. It is then likely that the doping atoms are affecting this, making it irrelevant whether the direction is Ga- or N-polar by creating defect centers.

Additionally, in all inclusions the 6-fold symmetry can be observed, forming hexagons around the $[0001]_{\mathrm{wz}}$ direction in the center, which is located at $\sim 54.7^\circ$ away from the PF origin. This leads to the same orientation relation found for the wurtzite inclusions of samples **S**, which grew on the $\{111\}$ facets of zincblende.

Analyzing the reflections of wurtzite growing on top of zincblende twins, as depicted in **Fig. 7.8(d)**, it is noted that most the wurtzite inclusions grew preferably on the twins when these were present in greater amounts, i.e., in samples **N**. For details on the simulation of the $10\bar{1}3_{\mathrm{wz}}$ PF, see **Section 6.3.5** and **Fig. 6.9**. Finally, **Fig. 6.11** depicts schematic and atomistic representation between zb-GaN, wz-GaN growing on it as well as their twins.

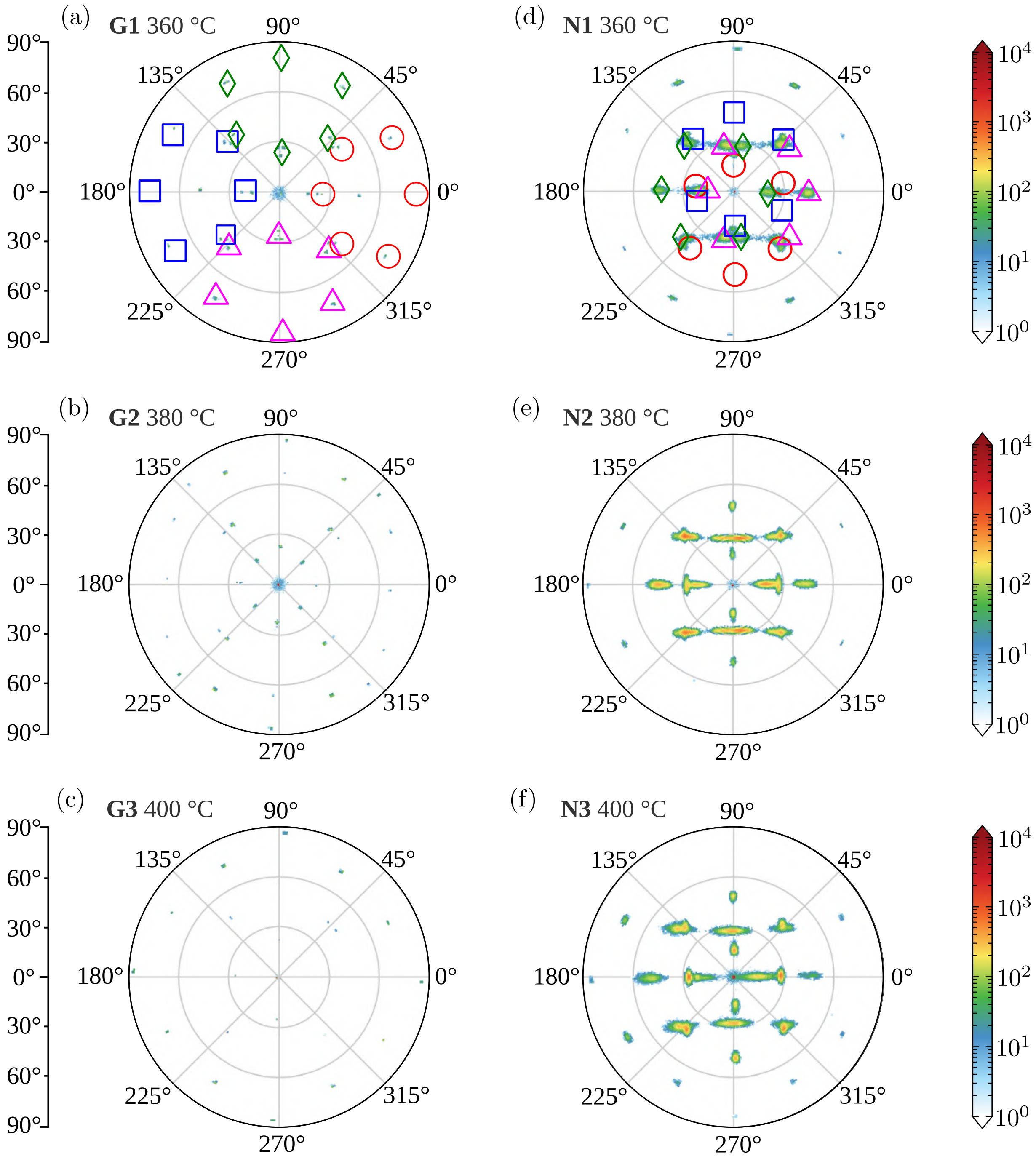

Fig. 7.8. Experimental $10\bar{1}3_{\mathrm{wz}}$ PF of samples **G** and **N**. The $10\bar{1}3_{\mathrm{wz}}$ GaN $(0001)[10\bar{1}0]$ and $(000\bar{1})[0100]$ reflections with 54.7° rotations are shown for sample **G1** in (a). The corresponding twinned reflections are indicated for sample **N1** in (d). Mg cell temperatures are indicated. Parts of this figure are published in [156].

7.3.5 EBSD characterization

The orientation maps in **Fig. 7.9** along $\boldsymbol{Z}$ and $\boldsymbol{X}$ give another perspective about the crystallographic relations between the substrate and the epilayers. A first glance shows that both maps from all samples **G** are remarkably homogeneous, without considering the unindexed areas in sample **G3**. Conversely, both orientation maps from samples **N** consist of a mixture of different shades of colors. That means that samples **N** exhibit a significantly higher degree of misorientation when compared to their **G** counterparts.

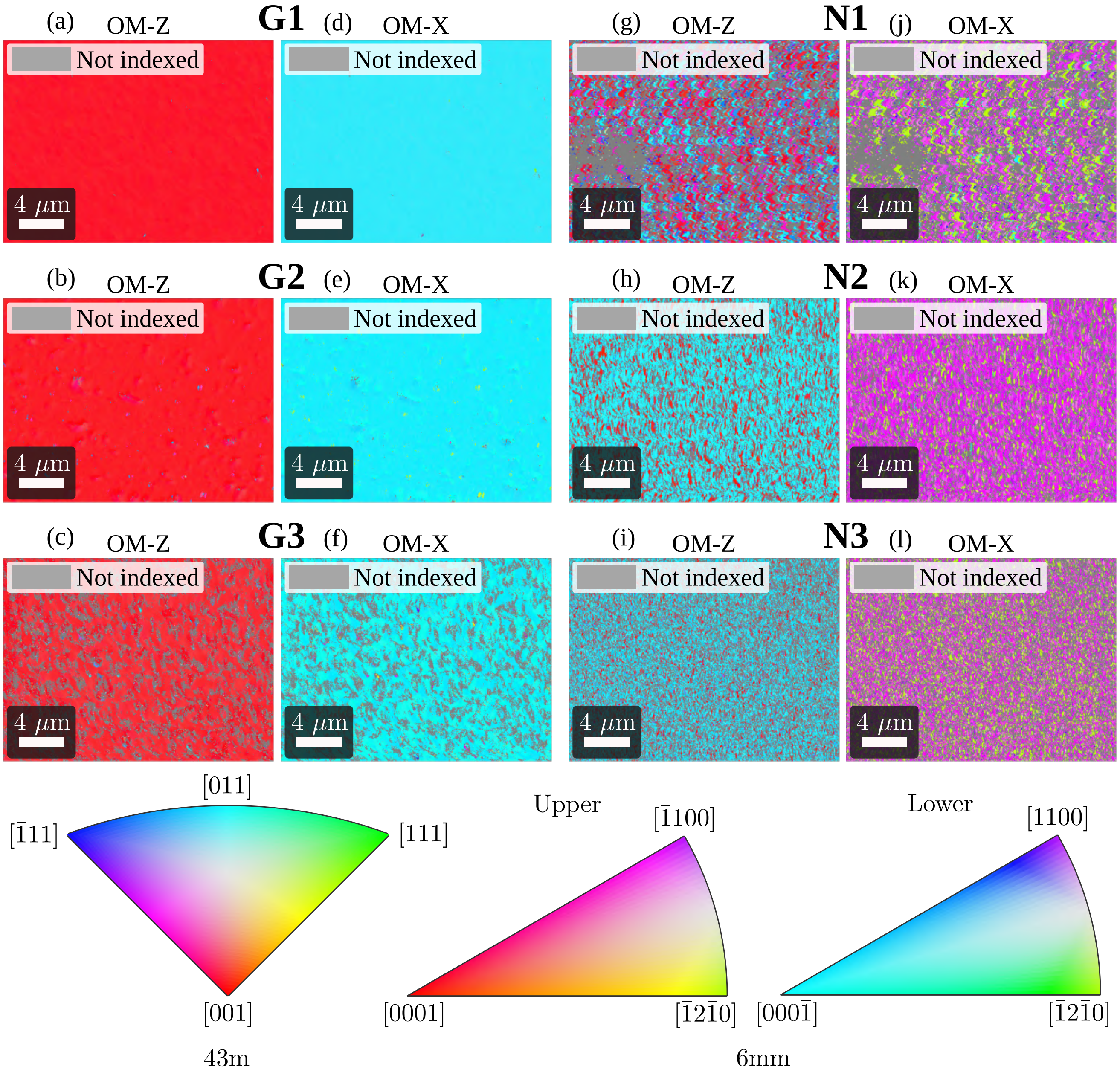

Fig. 7.9. EBSD orientation maps along ***Z*** (a)-(c) and (d)-(f) ***X*** from samples **G** as well as along ***Z*** (g)-(i) and (j)-(l) ***X*** from samples **N**. The IPF keys for point groups $\bar{4}3m$ and 6mm are shown. Parts of this figure are published in [156].

In the case of samples **G**, the red-dominated orientation map along ***Z*** indicates that the main out-of-plane orientation was either $[001]_{\mathrm{zb}}$ or $[0001]_{\mathrm{wz}}$ according to the inverse PF (IPF) keys. Considering that most of the EBSD area of these samples crystallized in the is zincblende phase (see Section 7.3.6), it is safe to conclude that it was rather the former orientation, i.e., $[001]_{\text{zb}}$. Furthermore, the cyan maps along $\boldsymbol{X}$ reveal that the main orientation in-plane was, considering now only zincblende, $[011]_{\text{zb}}$ according to the IPF key. This is in perfect agreement with the (001)[110] ideal orientation determined by the XRD ω-2θ scans and PF.

On the other hand, the mixture of cyan and red in the maps in samples **N** along $\boldsymbol{Z}$ indicate the $[001]_{\text{zb}}$ or $[0001]_{\text{wz}}$ and $[011]_{\text{zb}}$ or $[000\bar{1}]_{\text{wz}}$. Contrary to samples **G**, the **N** set resulted in almost pure wurtzite according to EBSD (see Section 7.3.6). Considering only those IPF keys results in the $\langle 0001\rangle_{\text{wz}}$ orientations out-of-plane. In-plane texture is revealed by the maps along $\boldsymbol{X}$, where magenta coloring, i.e., $[\bar{1}100]_{\text{wz}}$, dominates.

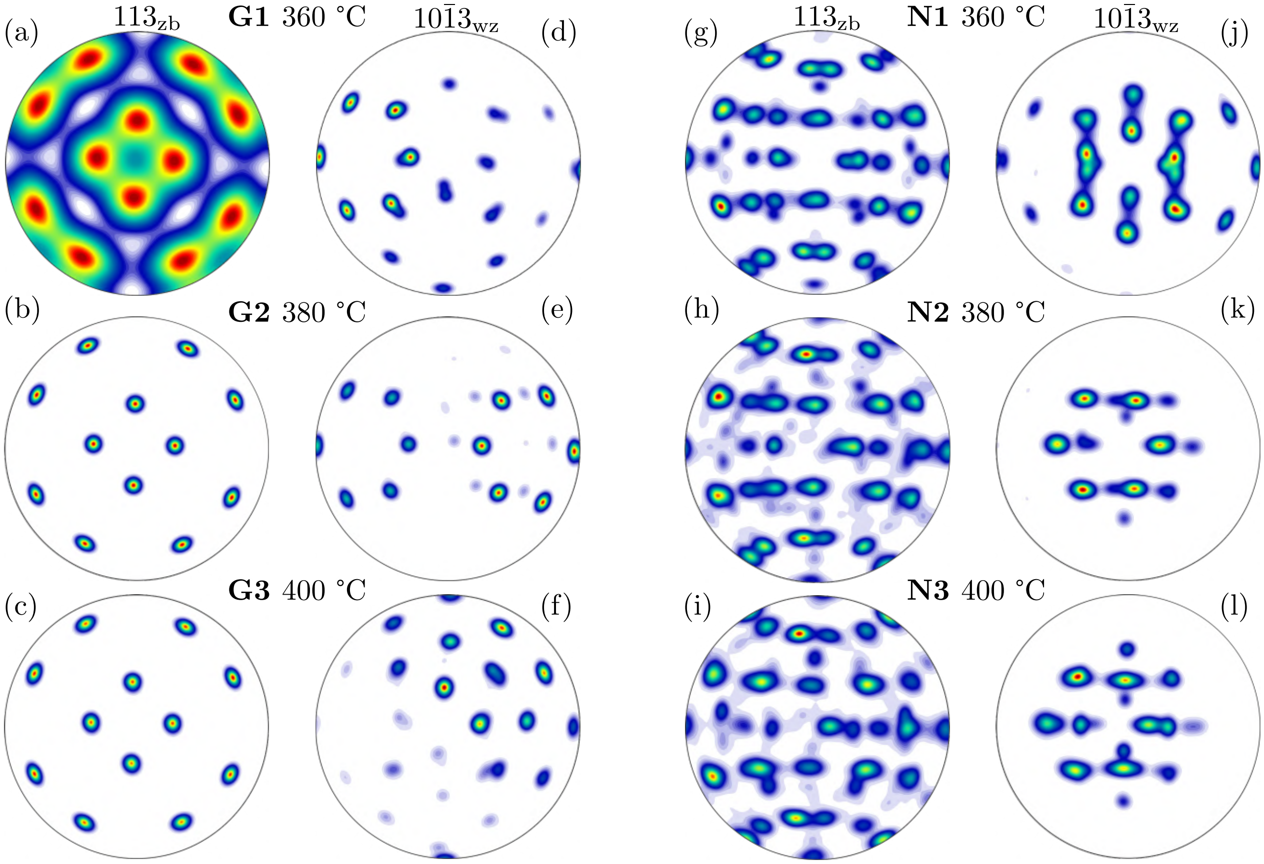

Fig. 7.10. EBSD (a)-(c) 113_{zb} and (d)-(f) $10\bar{1}3_{\text{wz}}$ PF from samples **G** as well (g)-(i) 113_{zb} and (j)-(l) $10\bar{1}3_{\text{wz}}$ PF from samples **N**. Mg cell temperature are shown. Parts of this figure are published in [156]

To confirm this analysis, the 113_{zb} and $10\bar{1}3_{\text{wz}}$ PF, computed from the orientation density function (ODF), are shown in Fig. 7.10. Comparing the EBSD PF from samples **G** to their XRD counterparts shows that there is good agreement between the two techniques. Except for sample **G1**, which shows a somewhat higher degree of misorientation, the rest of the 113_{zb} PF reveal almost the exact same texture.

Nevertheless, while the 113_{zb} XRD PF measurements show evidence of twins, EBSD does not, suggesting higher crystalline purities. Yet, reflections coming from wurtzite inclusions are clearly present with the same texture in the $10\bar{1}3$ PF.

On the other hand, both the 113_{zb} and $10\bar{1}3_{\mathrm{wz}}$ PFs from samples **N** show coherent results when comparing XRD and EBSD. In the former, most reflections from both twinned and untwinned zb-GaN can be observed. In the later, EBSD also shows a tendency of wurtzite to grow preferably on zb-GaN twins when these are present as well.

The upper wurtzite IPFs along $\boldsymbol{Z}$, also computed through the ODF, shown for both sample series in **Fig. 7.11**, categorically confirm this from a different point of view. In **Fig. 7.11(a)** and **Fig. 7.11(d)** the $[\bar{3}308]$ and $[\bar{1}107]$ directions are indicated, respectively. Note that the former belongs to the same family as $[\bar{3}038]_{\mathrm{wz}}$, while the latter is equivalent to $[10\bar{1}\bar{7}]_{\mathrm{wz}}$. These two directions are associated with wurtzite inclusions grown on the untwinned twinned zb-GaN, respectively, as observed in **Fig. 6.11**.

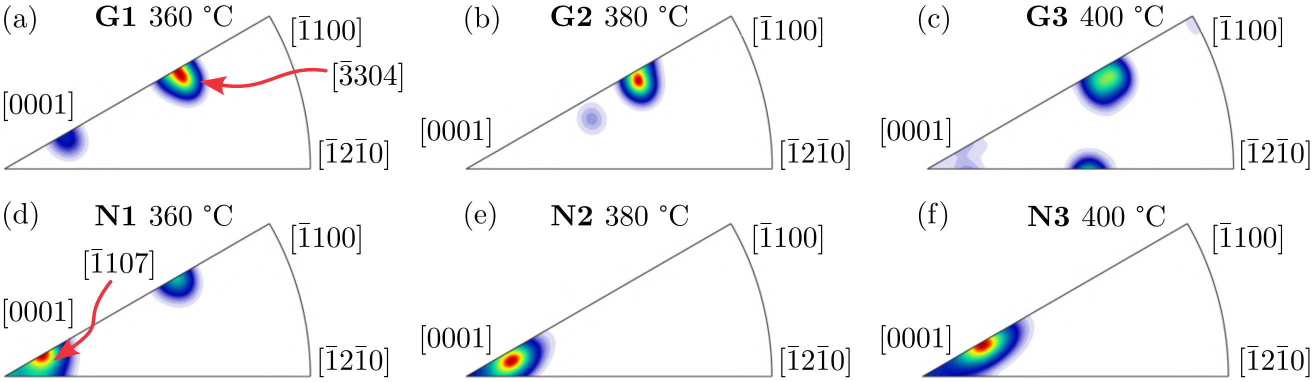

Fig. 7.11. EBSD upper wurtzite IPF along $\boldsymbol{Z}$ from samples **G** (a)-(c) and (d)-(f). Directions (a) $[\bar{3}304]$ and (b) $[\bar{1}107]$ are indicated for samples **G1** and **N1**, respectively. Mg cell temperature are shown. Parts of this figure are published in [156].

Considering that, it follows from the higher orientation densities near the $[\bar{1}107]$ direction in samples **N** that wurtzite inclusions grow preferably on twinned rather than untwinned zb-GaN. In samples **G**, on the contrary, the majority of the orientations are located near the $[\bar{3}308]$ direction, meaning that wurtzite grew on untwinned zb-GaN, perhaps due to the low amount of twins on which to grow.

Finally, **Fig. 7.12** shows the phase maps obtained from EBSD. These results once again show the very clear difference between samples **G** and **N**. While the former set entails almost pure zincblende, the opposite can be argued for the latter set. This qualitative analysis is in perfect agreement with the results from XRD discussed so far.

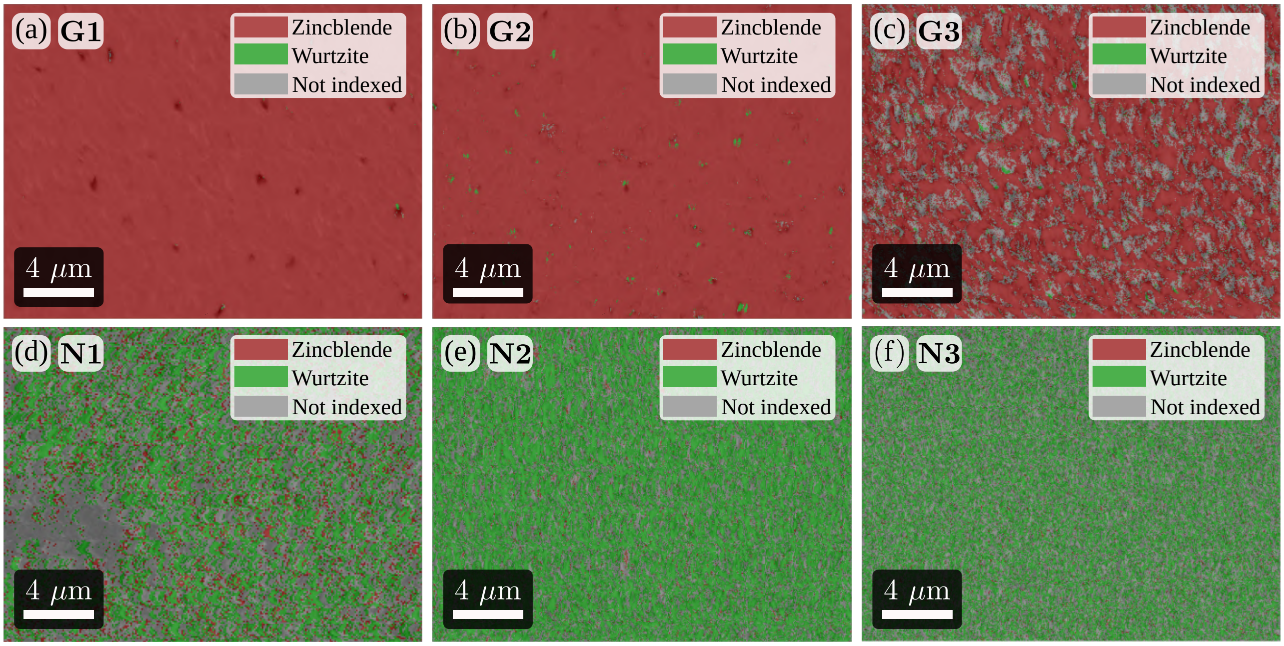

Fig. 7.12. EBSD phase maps from samples (a)-(c) **G** and (d)-(f) **N**. Parts of this figure are published in [156].

7.3.6 Quantitative results

Table 7.2 summarizes key quantitative results comparing zincblende Mg:GaN samples grown under Ga-rich and N-rich conditions, samples **G** and **N**, respectively, as described in **Section 7.3.1**. The data shows that samples **G**, prepared with 100 W RF plasma power, have considerably higher zincblende content than those grown with 150 W power, i.e., samples **N**. In particular, the conditions for sample **G3** resulted in an outstanding 99.9 % zincblende phase purity, as determined by XRD analysis.

Moreover, samples **G2** and **G1** also exhibit excellent zincblende contents of 97.8 % and 97.0 %, respectively. These samples also grew with low amounts of twins, with sample **G3** having a remarkably high 99.1 % of untwinned zb-GaN. In contrast, the 150 W samples in series **N** display significantly more twinning defects, with untwinned contents as low as 57.5 % in sample **N2**.

Notably, XRD and EBSD measurements are in close agreement with one another for the Ga-rich samples, but show significantly larger discrepancies for N-rich films. This suggests that rougher surfaces and defective crystalline quality (as discussed further in this text) caused issues indexing EBSD patterns. In that sense, the FWHM and RMS roughness measurements correlate closely with zincblende phase contents, revealing a marked difference in crystalline and surface quality between the Ga-rich and N-rich growth conditions.

Table 7.2. Results from the figures-of-merit used for samples **G** and **N**. For the XRD PF calculations (first two columns), only the 113_{zb} reflections from the well-oriented zb-GaN, as indicated in **Fig. 7.7(a)** were considered for the integrated intensity calculation with **Eq. (4.21)**, while the complete $10\bar{1}3_{wz}$ PF were used for wurtzite. The reported values are the average ± the standard error, when multiple measurements were taken. For EBSD data, numbers inside parenthesis indicate the percentage of unindexed area. RMS roughness numbers in parentheses indicate measurements in between droplets.

	Zincblende content/%	Untwinned content/%	EBSD zincblende content/%	FWHM/arcmin	RMS roughness/nm
G1	97.0 ± 0.9	94.1 ± 0.1	99.9 (< 0.1)	57.6 ± 1.7	9.8 ± 0.5 (4.8 ± 0.1)
G2	97.8 ± 0.3	96.6 ± 0.8	99.5 (0.2)	71.3 ± 1.6	8.6 ± 0.3 (4.9 ± 0.3)
G3	99.9 ± 0.1	99.1 ± 0.2	97.4 (27.2)	67.0 ± 3.0	5.9 ± 0.1 (5.6 ± 0.1)
N1	49.1 ± 2.2	67.6 ± 3.0	19.2 (47.1)	123.7 ± 1.1	10.2 ± 0.5
N2	35.8 ± 4.5	57.5 ± 4.8	< 0.1 (30.1)	102.9 ± 3.9	7.8 ± 0.6
N3	27.0 ± 1.9	56.9 ± 1.2	4.4 (46.4)	167.9 ± 5.1	8.8 ± 0.4

Additionally, the former set of samples, i.e., series **G**, exhibits more uniform properties across the analyzed regions, indicated by the smaller standard errors. In contrast, N-rich samples display significantly inferior crystalline and surface figures of merit.

This divergence likely stems from the surfactant effect of excess Ga atoms under the Ga-rich regime during growth of samples **G**, produced by the diminished amount of reactive N species due to the 100 W of plasma power used. The heightened adatom mobility, a characteristic of Ga-rich conditions (see **Section 3.2.3**), likely enabled Ga and Mg atoms to incorporate in an orderly fashion, facilitating two-dimensional layer-by-layer growth.

This seems to have minimized defects like stacking faults and dislocations, ultimately yielding higher zincblende purity, superior crystalline quality, smoother surfaces (especially in areas between droplets, as indicated by numbers in parenthesis in **Table 7.2**, as well as a high degree of orientation (as discussed in previous sections).

Under N-rich conditions, restricted adatom mobility disrupts the growing crystal. The excess nitrogen hinders surface diffusion, increasing disorderly incorporation of Ga and Mg. This defective growth promotes defects like twinning and wurtzite inclusions via stacking faults (see **Section 3.2.3**). These, in turn, lead to higher roughness, inferior crystalline quality, greater twin and wurtzite inclusions, and misorientation. All these defects also impede interpretation of EBSD patterns, explaining the discrepancy from XRD analysis.

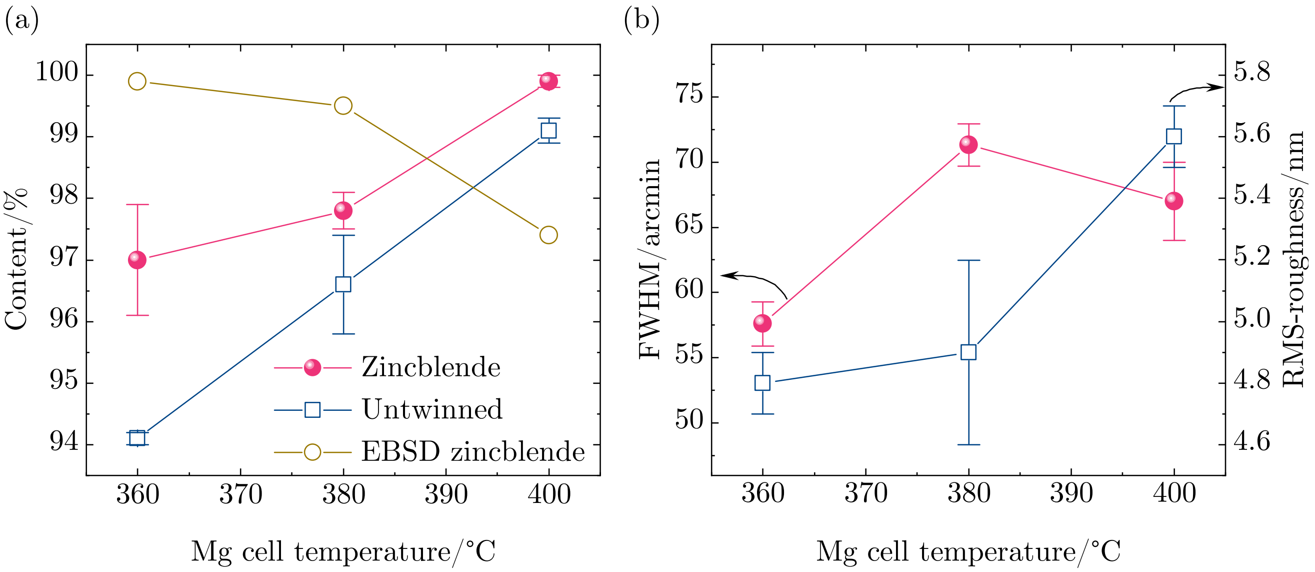

Fig. 7.13. For sample series **G**, (a) zincblende and untwinned zincblende contents from XRD PF and EBSD phase maps, as well as (b) FWHM of the 002_{zb} reflection and RMS-roughness from $10 \times 10\ \mu\mathrm{m}^2$ AFM scans. Roughness values in between droplets are plotted as indicated by numbers in parentheses in **Table 7.2**. Parts of this figure are published in [156].

Analyzing the impact of Mg doping temperature on samples **G**, as shown in **Fig. 7.13**, suggests that increasing the Mg cell temperature increases crystalline purity, yielding zincblende contents greater than 99 % with barely no twins, according to XRD PF measurements. However, the crystalline quality and surface roughness tell the opposite story. It seems that, overall, increasing Mg cell temperature produced a reduced crystalline quality (denoted by higher FWHM values) and rougher surfaces.

Considering that the rates of change in crystalline quality and surface roughness going from a Mg cell temperature of 360 °C in sample **G1** to 400 °C in sample **G3** are considerably greater, it is then reasonable to assume that, the greater the Mg atoms (due to higher cell temperatures), the more nucleation centers acting as defect generators. Moreover, the crystalline purities revealed by EBSD also indicate diminished quality the higher the Mg cell temperature are.

The impact of varying Mg doping temperature becomes much more apparent when examining the N-rich sample series **N**. For that, **Fig. 7.14** shows a comparison between samples **N1**, **N2**, **N3**, and **S2**, i.e., an undoped sample with the same nucleation temperature of 665 °C and 150 W of plasma power. While sample **S2** comprises nearly pure zincblende with negligible twinning, despite its N-rich stoichiometry, samples **N** are significantly more defective.

More specifically, zincblende content strongly decreases when adding Mg dopants at a Mg cell temperature of 360 °C from more than 99.6 % (sample **S2**) to 49.1 % (sample **N1**). This continues as Mg cell temperature increases further to 380 °C, where purity goes down to 35.8 % in sample **N2**, and 400 °C, where zincblende content reaches its lowest of 27 % in sample **N3**.

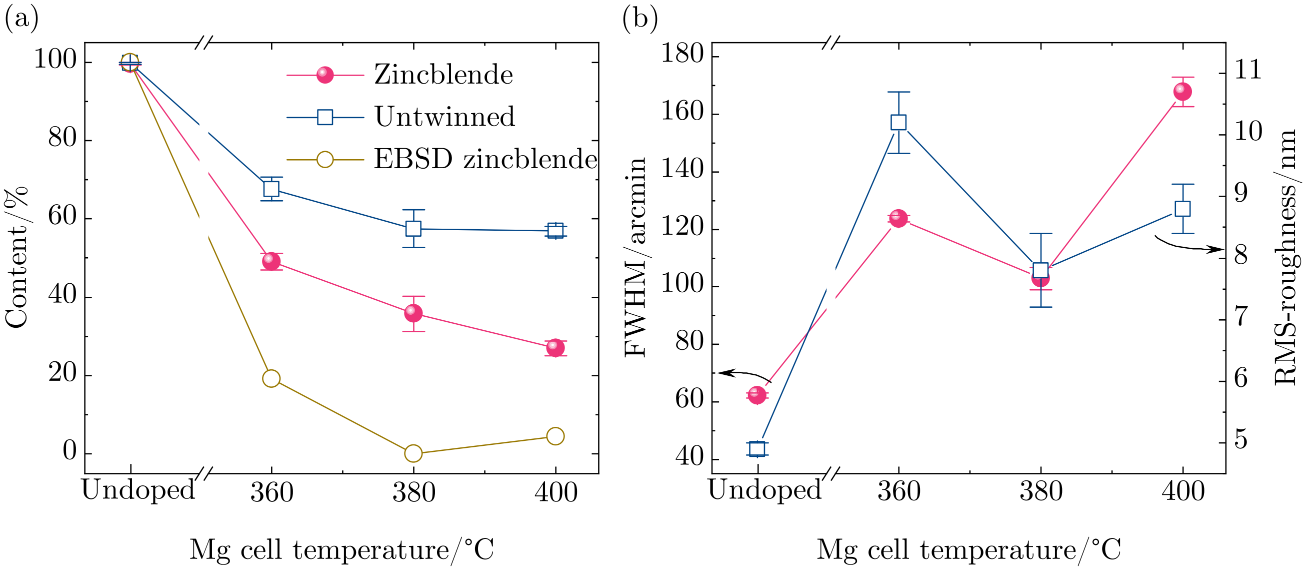

Fig. 7.14. For sample series **N**, (a) zincblende and untwinned zincblende contents from XRD PF and EBSD phase maps, as well as (b) FWHM of the 002_{zb} reflection and RMS-roughness from $10 \times 10\ \mu m^2$ AFM scans. Sample **S2** (grown with 150 W as series **N**) is added for comparison, with its FWHM adjusted using **Eq. (4.13)**. Parts of this figure are published in [156].

Very similar trends are observed in twinning and wurtzite inclusions by EBSD, as well as XRD ω scans FWHM and AFM RMS roughness, all going up with Mg cell temperature. Under N-rich conditions, the low Ga/N ratio deprives the growing front of sufficient surfactant atoms in samples **N**. With no excess Ga helping Mg incorporate more orderly, the disrupted crystallization provokes high defect densities, like stacking faults, spurring phase transitions and twinning.

7.3.7 Mg incorporation and activation

Further evidence of the previous discussion can be found by analyzing the incorporation and electrical activation of Mg atoms, as measured by SIMS and Hall-effect, respectively. For that, **Fig. 7.15** shows a plot of the results in **Table 7.3**.

There are a couple of key points that can be observed from the graph. First, there does not seem to be a significant increase of Mg content with Mg cell temperature in any of the measurements. At the very least, there is no clear trend since the contents go up and down in most cases. There are various reasons as to why the samples behave like so. Either there are not enough samples to obtain a clear trend, they are not homogeneous enough to express the expected trend or a saturation point is close to be reached.

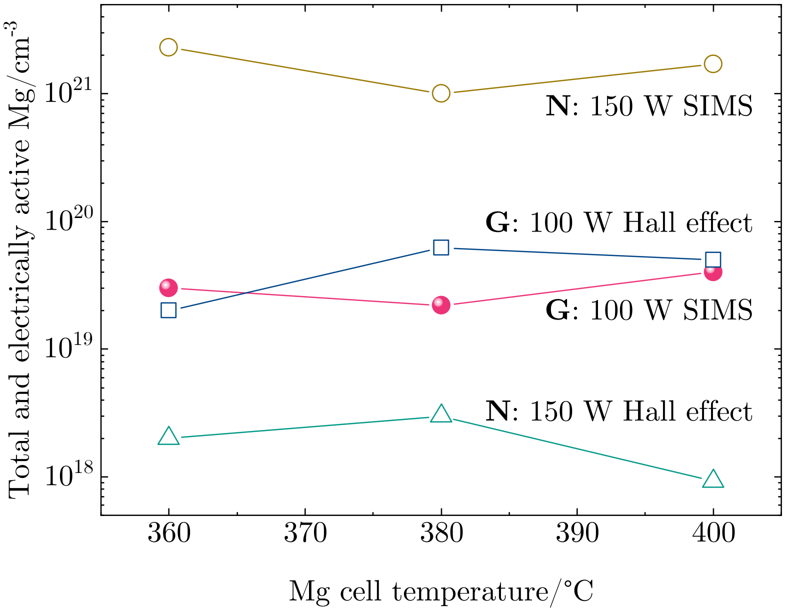

Fig. 7.15. Mg content and hole concentration measured from SIMS and Hall effect from samples **G** and **N** as function of Mg cell temperature.

Table 7.3. Mg and hole concentrations measured from SIMS and Hall effect the doped samples.

	SIMS/cm^{-3}	Hall effect/ cm^{-3}		SIMS/cm^{-3}	Hall effect/ cm^{-3}
G1	3.0×10^{19}	2.0×10^{19}	**N1**	2.3×10^{21}	2.0×10^{18}
G2	2.2×10^{19}	6.2×10^{19}	**N1**	1.0×10^{21}	3.0×10^{18}
G3	4.0×10^{19}	5.0×10^{19}	**N1**	1.7×10^{21}	9.2×10^{17}

Moreover, the hole concentration obtained by Hall effect, in the mids 10^{19}, shows good agreement with the total Mg content by SIMS for samples **G**, with the small discrepancies being likely due to measurement error or slight inhomogeneities between the analyzed areas. Additionally, the studied areas are enormously different; while Hall-effect analyzes macroscopic samples of about $\sim 10 \times 10$ mm^2, SIMS studies areas in the order of a few μm^2. This could be the reason as to why there seems to be higher amount of holes than Mg atoms.

This is not so much the case in samples **N**, for there are important discrepancies of ~ 3 orders of magnitude between the total incorporated Mg of $\sim 10^{21}$ and the electrically active dopants of $\sim 10^{18}$. Interestingly, these samples incorporate more Mg atoms than their **G** counterparts by about 2 orders of magnitude.

It is likely that, under Ga-rich conditions, there is some degree of competition of the incorporation between Ga and Mg atoms. Because there is not enough N for both kind of atoms, Ga seems to be preferably incorporating into the lattice. Nevertheless, the opposite behavior occurs when considering the hole concentration measured by Hall-effect. Although incorporated in less amounts, most of the Mg atoms in samples **G** are electrically active.

This all means that Ga-rich conditions enable higher activation efficiency compared to N-rich stoichiometry. This matches the structural characterization—Ga-rich samples had far fewer defects. The defects under N-rich growth likely trap much of the Mg in electrically inactive sites. Overall, the electrical and compositional data aligns with and provides further evidence for the importance of Ga-rich conditions for effective Mg doping of zb-GaN.

7.3.8 Comparison to reported figures of merit

While prior works have somewhat extensively examined Mg-doping of zincblende GaN, its quantitative impact on wurtzite inclusions and twinning remains widely unreported. Nevertheless, comparisons to similar studies on Si-doped and undoped GaN grown on various substrates using both MBE and metalorganic vapour phase epitaxy (MOVPE) provide useful context, as compiled in **Table 7.4**.

A key observation is that, unlike Si-doping (n-type), which significantly affects phase purity under Ga-rich growth with variations between 70 and 98 % [116], Mg-doping sustains exceptional zincblende phase contents in the 97.3 to 99.9 % range across the investigated growth temperatures. However, both Si and Mg doping increase XRD FWHM of the 002_{zb} reflection of GaN, indicating reduced crystalline quality at higher doping temperatures.

Remarkably, Mg-doped GaN on GaAs attains phase purity rivaling films grown on almost lattice-matched 3C-SiC substrates on both MBE and MOVPE. This is even in spite the large GaN-GaAs lattice mismatch of 25.54 % (see **Table 3.1**). This highlights the promise of GaAs for zincblende GaN integration. Therefore, the lower crystalline quality on GaAs is expected given the greater mismatch. The latter substrate, however, makes it up by being significantly more widespread and cheaper than SiC. Even then, the crystalline quality achieved in this work is highly competitive with prior GaN-on-GaAs and GaN-on-MgO reports.

Finally, while few works examine surface roughness alongside phase purity, the surface quality attained is comparable to existing benchmarks. However, definitive comparisons require consistent measurement conditions, underscoring the need for standardization in the analyzed areas.

Table 7.4. Comparison of reported values of RMS roughness, XRD ω-scans FWHM of the 002_{zb} reflection, zincblende content and twin content to those obtained in this work. FWHM values between parentheses are estimations to account for the difference in thickness with **Eq. (4.13)**.

Structure	Substrate	RMS roughness /nm	FWHM /arcmin	Zincblende content/%	Twin content/%	Ref
MBE Mg:GaN (400 nm)	GaAs (001)	4.8	57.6	99.9 (99.9)[a]	0.9[a]	This work
MBE GaN (371 nm)	GaAs (001)	–	83.84 (81.33)	98.5[b]	–	[31]
MBE GaN	GaAs (001)	–	–	97.24[c]	0.39[c]	[30]
MBE GaN	GaAs (001)	–	70	99.6[d]	–	[29]
MBE Si: GaN (300 nm)	MgO (001)	–	71 (60.7)	98[b]	–	[116]
MBE GaN (250 nm)	MgO (110)	–	–	95[b]	–	[25]
MBE GaN (1400 nm)	3C-SiC/Si (001)	–	21 (24.03)	83[b]	–	[27]
MBE GaN/AlN (600 nm)	3C-SiC/Si (001)	0.75[e]	20 (22.89)	99.7[b]	–	[28]
MOVPE GaN (300 nm)	3C-SiC/Si (001)	10.4[f]	–	> 98[g]	–	[144]
MOVPE GaN/AlGaN (600 nm)	3C-SiC/Si (001)	15.3[f]	41 (46.93)	97.13[g]	–	[145]
MOVPE GaN (500 nm)	3C-SiC/Si (001)	9.7[f]	26 (28)	99.7[g]	–	[146]

a Using XRD PF of GaN 113_{zb} and $10\bar{1}3_{wz}$ reflections. Value in parentheses is from EBSD.
b Using the GaN 002_{zb} and $10\bar{1}1_{wz}$ reflections from XRD reciprocal space maps.
c Using XRD rocking curves from 002_{zb}, 111_{zb}, $10\bar{1}0_{wz}$, and $10\bar{1}1_{wz}$ GaN reflections.
d Using XRD PF of GaN 002_{zb} and 0002_{wz} reflections. Value in parentheses is from EBSD.
e Over an area of $6 \times 6\ \mu\text{m}^2$.
f Over an area of $10 \times 10\ \mu\text{m}^2$.
g Using the GaN 113_{zb} and $10\bar{1}3_{wz}$ reflections from XRD reciprocal space maps.

Chapter 8: Conclusions and Outlook

This work examined the impact of different growth conditions on the crystalline purity and structure of zincblende (zb) GaN epilayers grown on GaAs (001) substrates by plasma-assisted molecular beam epitaxy. Three main aspects were investigated in detail: nucleation temperature, Mg doping level, and growth stoichiometry.

First, **Chapter 5** presented simulations, written in the Python programming language, of x-ray diffraction (XRD) pole figures (PF) for zincblende and wurtzite (wz) GaN. The simulations also including twins, which aided analysis of the experimental measurements. A thorough description of the algebra powering the simulation was first given. This included orthogonalization, rotation, and calculation of angles from different crystallographic orientations represented by vectors. Furthermore, some examples from the simulation were given and compared to other means of calculating pole figure angles.

The simulations matched well with experiments, validating the computational approach based on calculating diffraction angles from crystal orientations and lattice parameters. This enabled clear identification, and subsequent quantification, of reflections from untwinned zb-GaN, twinned zb-GaN, wurtzite inclusions on untwinned zincblende, and wurtzite on twinned zincblende. The simulations were key to unraveling the preferred growth directions under different conditions.

Then, **Chapter 6** systematically studied the effect of varying the growth temperature of a $\sim$ 5 nm thick nucleation layer from 655 to 685 °C in 10 °C increments for undoped zb-GaN epilayers grown GaAs by plasma-assisted molecular beam epitaxy (PAMBE). Structural properties were examined via XRD, electron backscatter diffraction (EBSD), and atomic force microscopy (AFM). Lower temperatures of 655 and 665 °C yielded the best results, with up to 99.6 % phase zincblende purity—from which 99.7 % was untwinned material—, 83 arcmin XRD rocking curve full-width at half-maximum (FWHM), and 5 nm root mean square (RMS) roughness. This meant excellent phase purity and superb crystalline quality with a smooth surface. Moreover, the sample grown with a nucleation temperature of 665 °C exhibited the greatest degree of orientation coherence to the substrate.

Growing at a higher nucleation temperature of 675 °C and above caused more wurtzite inclusions, twins, rough surfaces, poor crystalline quality and misorientation due to the poorer nucleation. This condition likely stemmed from higher mobilities due to greater thermal energies, leading to lower density of big nuclei where misfit dislocations could not glide out from them. Conversely, nuclei at lower temperatures were likely small enough, arising from the restricted adatom mobility, such that the said dislocations could reach the edges or annihilate each other, producing superior crystalline purity and quality.

The analysis shown here demonstrated the critical importance of having precise control of this ultrathin nucleation layer so that GaN quality in the zincblende phase can be ultimately optimized. Moreover, this work shows the profound effects of the first stages, e.g., < 5 nm, of heteroepitaxial growth of GaN on GaAs.

Finally, **Chapter 7** thoroughly examined Mg-doped zb-GaN epitaxial films grown under Ga-rich (100 W of N plasma) and N-rich (150 W of N plasma) conditions, as determined by SEM, AFM, and Nomarski micrographs. According to the obtained results, Ga-rich growth enabled a record high phase purity up to 99.9 % zincblende content—with 99.1 % of it untwinned— as well as an excellent 57 arcmin rocking curve FWHM for homoepitaxial films grown on nucleation layers with the conditions optimized as described in **Chapter 6**. Moreover, Ga-rich grown samples yielded smooth surfaces with RMS roughness values down to 4.8 nm, as measured by AFM, in areas between Ga droplets. In contrast, N-rich films had severe wurtzite contamination and twinning with as low as 27 % zincblende purity. Moreover, rocking curve FWHM and AFM roughness values as high as 167.9 arcmin and 10.2 nm, respectively, were measured from these samples, indicating significantly lesser crystalline and surface quality.

The results found up to this point clearly indicate the superiority of Ga-stabilized growth, most likely resulting from the enhanced mobility due to the Ga wetting layer formed thanks to excess Ga atoms. In turn, this conditions led to smaller amounts of stacking faults and dislocations, producing greater zincblende purity with higher crystalline quality.

Furthermore, dopant content studies via Secondary ion mass spectrometry and Hall effect measurements showed 2 to 3 orders of magnitude more electrically active Mg for Ga-rich films. This highlights the surfactant role of excess Ga in promoting step-flow growth and enabling effective Mg incorporation into electrically active sites. Under N-rich conditions, Mg seems to incorporate rather in an unorderly fashion, leading to high densities of stacking, causing all the defects hereby described.

On the other hand, varying Mg doping cell temperature from 360 to 400 °C was also analyzed for both regimes. Increasing Mg doping temperature for Ga-rich films slightly reduced crystalline and surface quality; however, these samples maintained exceptional phase purity above 97 %. For N-rich films, higher Mg cell temperatures exacerbated defects and decreased zincblende contents down to just 27 %. This supports the idea that Mg atoms lead to defect centers when no excess Ga is present to act as a surfactant and help orderly incorporation.

Through detailed structural and electrical evaluation, this work determined the optimal growth conditions for high-quality, highly-pure zb-GaN on GaAs substrates. Low nucleation temperatures around 665°C and Ga-rich stoichiometry were most critical for minimizing defects leading to twins and wurtzite inclusions. This helps pave the way for monolithic integration of zb-GaN optoelectronics on mainstream GaAs platforms.

However, ongoing work should first explore optimizing even more the growth conditions. For instance, the N plasma power could be fine-tuned between 100 and 150 W in order to obtain Ga/N ratios that allow avoiding Ga droplets altogether while retaining the excellent properties described in this work. With the same objective, other MBE schemes such as alternating growth could be employed. Further confirmation via higher-resolution techniques, such as transmission electron microscopy, could also help these fine-tuned optimizations. Moreover, the effects of nucleation temperature and doping on other properties— e.g., bandgap, thermal properties, deeper electrical characterization—could also be conducted. Finally, the techniques hereby described could be used to optimize the growth conditions of AlN, InN, and/or their ternaries so that nitride heterostructures can be produced. Once this is done, doping could be investigated in the same manner to grow *p*-*n* junctions.

Then, the research work could lean towards potential device applications. For instance, the excellent phase purity and crystalline quality could enable high-efficiency zb-GaN-based light emitting diodes on GaAs; even laser diodes may be viable at some point. Beyond optoelectronics, applications in high-frequency transistors, sensors, and power electronics based on the GaAs platform could benefit from high-quality zb-GaN epilayers studied in this work. Realizing the full potential of zb-GaN on GaAs, and other substrates, remains an exciting open frontier with room for much follow-on research.

References

[1] N. E. Holden, T. B. Coplen, J. K. Böhlke, L. V. Tarbox, J. Benefield, J. R. de Laeter, P. G. Mahaffy, G. O'Connor, E. Roth, D. H. Tepper, T. Walczyk, M. E. Wieser, and S. Yoneda, "IUPAC Periodic Table of the Elements and Isotopes (IPTEI) for the Education Community (IUPAC Technical Report)", Pure and Applied Chemistry **90**, 1833–2092 (2018).

[2] P. M. Cabral, J. C. Pedro, and N. B. Carvalho, "Nonlinear device model of microwave power GaN HEMTs for high power-amplifier design", IEEE Transactions on Microwave Theory and Techniques **52**, 2585–2592 (2004).

[3] D. Li, X. Sun, H. Song, Z. Li, Y. Chen, H. Jiang, and G. Miao, "Realization of a High-Performance GaN UV Detector by Nanoplasmonic Enhancement", Advanced Materials **24**, 845–849 (2012).

[4] I. Akasaki, H. Amano, N. Koide, M. Kotaki, and K. Manabe, "Conductivity control of GaN and fabrication of UV/blue GaN light emitting devices", Physica B: Condensed Matter **185**, 428–432 (1993).

[5] S. Nakamura, T. Mukai, and M. Senoh, "Candela-class high-brightness InGaN/AlGaN double-heterostructure blue-light-emitting diodes", Applied Physics Letters **64**, 1687–1689 (1994).

[6] *The Nobel Prize in Physics 2014*, NobelPrize.org, `nobelprize.org/prizes/physics/2014` (visited on 12/07/2022).

[7] S. Hammersley, M. J. Kappers, F. C.-P. Massabuau, S.-L. Sahonta, P. Dawson, R. A. Oliver, and C. J. Humphreys, "Effects of quantum well growth temperature on the recombination efficiency of InGaN/GaN multiple quantum wells that emit in the green and blue spectral regions", Applied Physics Letters **107**, 132106 (2015).

[8] V. Fiorentini, F. Bernardini, F. Della Sala, A. Di Carlo, and P. Lugli, "Effects of macroscopic polarization in III-V nitride multiple quantum wells", Physical Review B **60**, 8849–8858 (1999).

[9] R. Grady and C. Bayram, "Simulation of zincblende AlGaN/GaN high electron mobility transistors for normally-off operation", Journal of Physics D: Applied Physics **50**, 265104 (2017).

[10] W. Saito, Y. Takada, M. Kuraguchi, K. Tsuda, and I. Omura, “Recessed-gate structure approach toward normally off high-Voltage AlGaN/GaN HEMT for power electronics applications”, IEEE Transactions on Electron Devices **53**, 356–362 (2006).

[11] M. F. Schubert, J. Xu, J. K. Kim, E. F. Schubert, M. H. Kim, S. Yoon, S. M. Lee, C. Sone, T. Sakong, and Y. Park, “Polarization-matched GaInN/AlGaInN multi-quantum-well light-emitting diodes with reduced efficiency droop”, Applied Physics Letters **93**, 041102 (2008).

[12] K. J. Chen and C. Zhou, “Enhancement-mode AlGaN/GaN HEMT and MIS-HEMT technology: Enhancement-mode AlGaN/GaN HEMT and MIS-HEMT technology”, Physica Status Solidi (a) **208**, 434–438 (2011).

[13] G. Greco, F. Iucolano, and F. Roccaforte, “Review of technology for normally-off HEMTs with p-GaN gate”, Materials Science in Semiconductor Processing **78**, 96–106 (2018).

[14] M. Monavarian, A. Rashidi, and D. Feezell, “A Decade of Nonpolar and Semipolar III-Nitrides: A Review of Successes and Challenges”, Physica Status Solidi (a) **216**, 1800628 (2019).

[15] T. Hanada, “Basic Properties of ZnO, GaN, and Related Materials”, in *Oxide and Nitride Semiconductors: Processing, Properties, and Applications*, edited by T. Yao and S.-K. Hong (Springer, Berlin, 2009), pp. 1–19.

[16] I. Vurgaftman and J. R. Meyer, “Band parameters for nitrogen-containing semiconductors”, Journal of Applied Physics **94**, 3675–3696 (2003).

[17] C.-H. Kim and B.-H. Han, “Valence subbands and optical gain in wurtzite and zinc-blende strained GaN/AlGaN quantum wells”, Solid State Communications **106**, 127–132 (1998).

[18] C.-Y. Yeh, Z. W. Lu, S. Froyen, and A. Zunger, “Zinc-blende–wurtzite polytypism in semiconductors”, Physical Review B **46**, 10086–10097 (1992).

[19] H. Yang, O. Brandt, and K. Ploog, “MBE growth of cubic GaN on GaAs substrates”, Physica Status Solidi (b) **194**, 109–120 (1996).

[20] J. Wu, H. Yaguchi, H. Nagasawa, Y. Yamaguchi, K. Onabe, Y. Shiraki, and R. I. Ryoichi Ito, “Crystal Structure of GaN Grown on 3C-SiC Substrates by Metalorganic Vapor Phase Epitaxy”, Japanese Journal of Applied Physics **36**, 4241 (1997).

[21] E. Tschumak, M. de Godoy, D. As, and K. Lischka, “Insulating substrates for cubic GaN-based HFETs”, Wide Band Gap Semiconductor Nanostructures for Optoelectronic Applications **40**, 367–369 (2009).

[22] T. Wonglakhon and D. Zahn, “Interaction potentials for modelling GaN precipitation and solid state polymorphism”, Journal of Physics: Condensed Matter **32**, 205401 (2020).

[23] M. A. Zwijnenburg and S. T. Bromley, “Structural richness of ionic binary materials: An exploration of the energy landscape of magnesium oxide”, Physical Review B **83**, 024104 (2011).

[24] M. Kakuda, S. Morikawa, S. Kuboya, R. Katayama, H. Yaguchi, and K. Onabe, “RF-MBE growth of cubic AlN on MgO (001) substrates via 2-step c-GaN buffer layer”, Journal of Crystal Growth **378**, 307–309 (2013).

[25] K. Meyer, M. Buchholz, and D. M. Schaadt, “GaN growth on (0 0 1) and (1 1 0) MgO under different Ga/N ratios by MBE”, Journal of Crystal Growth **589**, 126681 (2022).

[26] T. Schupp, G. Rossbach, P. Schley, R. Goldhahn, K. Lischka, and D. J. As, “Growth of atomically smooth cubic AlN by molecular beam epitaxy”, Physica Status Solidi (c) **7**, 17–20 (2010).

[27] R. M. Kemper, M. Häberlen, T. Schupp, M. Weinl, M. Bürger, M. Ruth, C. Meier, T. Niendorf, H. J. Maier, K. Lischka, D. J. As, and J. K. N. Lindner, “Formation of defects in cubic GaN grown on nano-patterned 3C-SiC (001)”, Physica Status Solidi (c) **9**, 1028–1031 (2012).

[28] M. F. Zscherp, N. Mengel, D. M. Hofmann, V. Lider, B. Ojaghi Dogahe, C. Becker, A. Beyer, K. Volz, J. Schörmann, and S. Chatterjee, “AlN Buffer Enhances the Layer Quality of MBE-Grown Cubic GaN on 3C-SiC”, Crystal Growth & Design **22**, 6786–6791 (2022).

[29] Z. Qin, M. Kobayashi, and A. Yoshikawa, “X-ray diffraction reciprocal space and pole figure characterization of cubic GaN epitaxial layers grown on (0 0 1) GaAs by molecular beam epitaxy”, Journal of Materials Science: Materials in Electronics **10**, 199–202 (1999).

[30] B. Qu, X. Zheng, Y. Wang, Z. Feng, S. Liu, S. Lin, H. Yang, and J. Liang, “X-Ray diffraction determination of the fractions of hexagonal and twinned phases in cubic GaN layers grown on (001)GaAs substrate”, Thin Solid Films **392**, 29–33 (2001).

[31] Y. Casallas-Moreno, S. Gallardo-Hernández, F. Ruiz-Zepeda, B. Monroy, A. Hernández-Hernández, A. Herrera-Gómez, A. Escobosa-Echavarría, G. Santana, A. Ponce, and M. López-López, “As4 overpressure effects on the phase purity of cubic GaN layers grown on GaAs substrates by RF-MBE”, Applied Surface Science **353**, 588–593 (2015).

[32] M. A. Reshchikov, P. Ghimire, and D. O. Demchenko, “Magnesium acceptor in gallium nitride. I. Photoluminescence from Mg-doped GaN”, Physical Review B **97**, 205204 (2018).

[33] M. C. Yoo, M. Park, S. Kang, H. Cho, and J. Lee, “Growth and p-type doping of GaN on c-plane sapphire by nitrogen plasma-assisted molecular beam epitaxy”, Molecular Beam Epitaxy 1996 **175–176**, 100–106 (1997).

[34] A. Bhattacharyya, W. Li, J. Cabalu, T. D. Moustakas, D. J. Smith, and R. L. Hervig, “Efficient p-type doping of GaN films by plasma-assisted molecular beam epitaxy”, Applied Physics Letters **85**, 4956–4958 (2004).

[35] D. J. As, T. Simonsmeier, B. Schöttker, T. Frey, D. Schikora, W. Kriegseis, W. Burkhardt, and B. K. Meyer, "Incorporation and optical properties of magnesium in cubic GaN epilayers grown by molecular beam epitaxy", Applied Physics Letters **73**, 1835–1837 (1998).

[36] R. E. L. Powell, S. V. Novikov, C. T. Foxon, A. V. Akimov, and A. J. Kent, "Photoluminescence of magnesium and silicon doped cubic GaN", Physica Status Solidi (c) **11**, 385–388 (2014).

[37] C. A. Hernández-Gutiérrez, Y. L. Casallas-Moreno, V.-T. Rangel-Kuoppa, D. Cardona, Y. Hu, Y. Kudriatsev, M. A. Zambrano-Serrano, S. Gallardo-Hernandez, and M. Lopez-Lopez, "Study of the heavily p-type doping of cubic GaN with Mg", Scientific Reports **10**, 16858 (2020).

[38] D. Dyer, S. A. Church, M. Jain, M. J. Kappers, M. Frentrup, D. J. Wallis, R. A. Oliver, and D. J. Binks, "The effect of thermal annealing on the optical properties of Mg-doped zincblende GaN epilayers", Journal of Applied Physics **130**, 085705 (2021).

[39] H. Morkoç, "General Properties of Nitrides", in *Handbook of Nitride Semiconductors and Devices: Materials Properties, Physics and Growth*, Vol. 1, edited by H. Morkoç (Wiley, 2008), pp. 1–129.

[40] Y.-N. Xu and W. Y. Ching, "Electronic, optical, and structural properties of some wurtzite crystals", Physical Review B **48**, 4335–4351 (1993).

[41] X. Zheng, Y. Wang, Z. Feng, H. Yang, H. Chen, J. Zhou, and J. Liang, "Method for measurement of lattice parameter of cubic GaN layers on GaAs (001)", Journal of Crystal Growth **250**, 345–348 (2003).

[42] M. Mbarki, R. Alaya, and A. Rebey, "Ab initio investigation of structural and electronic properties of zinc blende $AlN_{1\text{-}x}Bi_x$ alloys", Solid State Communications **155**, 12–15 (2013).

[43] S. Saib and N. Bouarissa, "Structural phase transformations of GaN and InN under high pressure", Physica B: Condensed Matter **387**, 377–382 (2007).

[44] E. D. Gutiérrez-Senior, J. A. Rodríguez M., and J. Sierra-Ortega, "Structural and Electronic Properties of $Zr_xAl_{1\text{-}x}N$ in Cubic Phase Using First Principles", Journal of Superconductivity and Novel Magnetism **26**, 2471–2473 (2013).

[45] K. Momma and F. Izumi, "*VESTA 3* for three-dimensional visualization of crystal, volumetric and morphology data", Journal of Applied Crystallography **44**, 1272–1276 (2011).

[46] Y.-C. Tsai and C. Bayram, "Structural and Electronic Properties of Hexagonal and Cubic Phase AlGaInN Alloys Investigated Using First Principles Calculations", Scientific Reports **9**, 6583 (2019).

[47] I. Vurgaftman, J. R. Meyer, and L. R. Ram-Mohan, "Band parameters for III–V compound semiconductors and their alloys", Journal of Applied Physics **89**, 5815–5875 (2001).

[48] M. Radia, T. Abdelghani, G. ElHouari, S. Asmaa, and B. Ahmed Hafid, “Investigation of the Substituting Effect of Se on the Physical Properties and Performances of CdSe$_x$Te$_{1-x}$ and ZnSe$_x$Te$_{1-x}$ Materials for Semiconductor Radiation Detectors”, Revista Mexicana de Física **67**, `10.31349/RevMexFis.67.041002` (2021).

[49] S. M. Sze and M. K. Lee, *Semiconductor devices, physics and technology*, 3rd ed. (Wiley, Hoboken, N.J, 2012), 578 pp.

[50] I. C. Kizilyalli, A. P. Edwards, H. Nie, D. Disney, and D. Bour, “High Voltage Vertical GaN p-n Diodes With Avalanche Capability”, IEEE Transactions on Electron Devices **60**, 3067–3070 (2013).

[51] Z. An, C. Men, Z. Xu, P. K. Chu, and C. Lin, “Electrical properties of AlN thin films prepared by ion beam enhanced deposition”, Surface and Coatings Technology **196**, 130–134 (2005).

[52] S. C. Shen, “III-Nitride Electronic Devices for Harsh Environments”, in *Semiconductor Devices in Harsh Conditions*, edited by K. Weide-Zaage and M. Chrzanowska-Jeske (CRC Press, Boca Raton, 2016).

[53] N. Ben Hassine, D. Mercier, P. Renaux, G. Parat, S. Basrour, P. Waltz, C. Chappaz, P. Ancey, and S. Blonkowski, “Dielectrical properties of metal-insulator-metal aluminum nitride structures: Measurement and modeling”, Journal of Applied Physics **105**, 044111 (2009).

[54] Y.-C. Tsai and C. Bayram, “Band Alignments of Ternary Wurtzite and Zincblende III-Nitrides Investigated by Hybrid Density Functional Theory”, ACS Omega **5**, 3917–3923 (2020).

[55] D. Fritsch, H. Schmidt, and M. Grundmann, “Band-structure pseudopotential calculation of zinc-blende and wurtzite AlN, GaN, and InN”, Physical Review B **67**, 235205 (2003).

[56] E. Silveira, J. A. Freitas, M. Kneissl, D. W. Treat, N. M. Johnson, G. A. Slack, and L. J. Schowalter, “Near-bandedge cathodoluminescence of an AlN homoepitaxial film”, Applied Physics Letters **84**, 3501–3503 (2004).

[57] M. Suzuki and T. Uenoyama, “Strain effect on electronic and optical properties of GaN/AlGaN quantum-well lasers”, Journal of Applied Physics **80**, 6868–6874 (1996).

[58] V. Bougrov, M. E. Levinshteĭn, S. L. Rumyantsev, and A. Zubrilov, “Gallium Nitride (GaN)”, in *Properties of advanced semiconductor materials: GaN, AlN, InN, BN, SiC, SiGe*, edited by M. E. Levinshteĭn, S. L. Rumyantsev, and M. S. Shur (Wiley, New York, 2001).

[59] W. J. Fan, M. F. Li, T. C. Chong, and J. B. Xia, “Electronic properties of zinc-blende GaN, AlN, and their alloys Ga$_{1-x}$Al$_x$N”, Journal of Applied Physics **79**, 188–194 (1996).

[60] H. Morkoç, "Electronic Band Structure and Polarization Effects", in *Handbook of Nitride Semiconductors and Devices: Materials Properties, Physics and Growth*, Vol. 1, edited by H. Morkoç (Wiley, 2008), pp. 131–321.

[61] J. F. Nye, *Physical properties of crystals: their representation by tensors and matrices* (Oxford University Press, Oxford, 1984).

[62] A. Authier and A. Zarembowitch, "Elastic properties", in *International Tables for Crystallography: Physical properties of crystals*, Vol. D, edited by A. Authier, 2nd ed. (International Union of Crystallography, Chester, 2013), pp. 72–99.

[63] N. Nakamura, H. Ogi, and M. Hirao, "Elastic, anelastic, and piezoelectric coefficients of GaN", Journal of Applied Physics **111**, 013509 (2012).

[64] K. Adachi, H. Ogi, A. Nagakubo, N. Nakamura, M. Hirao, M. Imade, M. Yoshimura, and Y. Mori, "Piezoelectric coefficients of GaN determined by hopping conduction of carriers", Applied Physics Letters **109**, 182108 (2016).

[65] K. Tsubouchi, K. Sugai, and N. Mikoshiba, "AlN Material Constants Evaluation and SAW Properties on AlN/Al2O3and AlN/Si", in 1981 Ultrasonics Symposium (14–Oct. 16, 1981), pp. 375–380.

[66] G. Bu, D. Ciplys, M. Shur, L. J. Schowalter, S. Schujman, and R. Gaska, "Electromechanical coupling coefficient for surface acoustic waves in single-crystal bulk aluminum nitride", Applied Physics Letters **84**, 4611–4613 (2004).

[67] A. V. Sotnikov, H. Schmidt, M. Weihnacht, E. P. Smirnova, T. Y. Chemekova, and Y. N. Makarov, "Elastic and piezoelectric properties of AlN and $LiAlO_2$ single crystals", IEEE Transactions on Ultrasonics, Ferroelectrics, and Frequency Control **57**, 808–811 (2010).

[68] F. Peng, Y. Han, H. Fu, and X. Yang, "First-principles calculations on structure and elasticity of wurtzite-type indium nitride under pressure", Journal of Alloys and Compounds **475**, 885–888 (2009).

[69] F. Bernardini, V. Fiorentini, and D. Vanderbilt, "Accurate calculation of polarization-related quantities in semiconductors", Physical Review B **63**, 193201 (2001).

[70] M. E. Levinshtein and S. L. Rumyantsev, "GALLIUM ARSENIDE (GaAs)", in *Handbook Series on Semiconductor Parameters: Si, Ge, C (Diamond), GaAs, GaP, GaSb, InAs, InP, InSb*, Vol. 1, edited by M. E. Levinshtein, S. L. Rumyantsev, and M. Shur (World Scientific Publishing, Danvers, 1996), pp. 77–103.

[71] M. A. Caro, S. Zhang, T. Riekkinen, M. Ylilammi, M. A. Moram, O. Lopez-Acevedo, J. Molarius, and T. Laurila, "Piezoelectric coefficients and spontaneous polarization of ScAlN", Journal of Physics: Condensed Matter **27**, 245901 (2015).

[72] S. Manna, K. R. Talley, P. Gorai, J. Mangum, A. Zakutayev, G. L. Brennecka, V. Stevanović, and C. V. Ciobanu, "Enhanced Piezoelectric Response of AlN via CrN Alloying", Physical Review Applied **9**, 034026 (2018).

[73] K. Hirata, Y. Mori, H. Yamada, M. Uehara, S. A. Anggraini, and M. Akiyama, "Significant Enhancement of Piezoelectric Response in AlN by Yb Addition.", Materials (Basel, Switzerland) **14**, `10.3390/ma14020309` (2021).

[74] "Transistors and Technologies", in *Radio Frequency Integrated Circuits and Technologies*, edited by F. Ellinger (Springer Berlin Heidelberg, Berlin, Heidelberg, 2007), pp. 109–190.

[75] Y. R. Wu, "Electronic and Transport Properties of III-Nitride Semiconductors", in *Handbook of GaN Semiconductor Materials and Devices*, edited by W. Bi, H. C. Kuo, P. C. Ku, and B. Shen (CRC Press, Boca Raton, 2017).

[76] O. Ambacher, J. Smart, J. R. Shealy, N. G. Weimann, K. Chu, M. Murphy, W. J. Schaff, L. F. Eastman, R. Dimitrov, L. Wittmer, M. Stutzmann, W. Rieger, and J. Hilsenbeck, "Two-dimensional electron gases induced by spontaneous and piezoelectric polarization charges in N- and Ga-face AlGaN/GaN heterostructures", Journal of Applied Physics **85**, 3222–3233 (1999).

[77] G. Li, Y. Cao, H. G. Xing, and D. Jena, "High mobility two-dimensional electron gases in nitride heterostructures with high Al composition AlGaN alloy barriers", Applied Physics Letters **97**, 222110 (2010).

[78] S. Ganguly, J. Verma, H. (Xing, and D. Jena, "Plasma MBE growth conditions of AlGaN/GaN high-electron-mobility transistors on silicon and their device characteristics with epitaxially regrown ohmic contacts", Applied Physics Express **7**, 105501 (2014).

[79] Y. Cho, Y. Ren, H. G. Xing, and D. Jena, "High-mobility two-dimensional electron gases at AlGaN/GaN heterostructures grown on GaN bulk wafers and GaN template substrates", Applied Physics Express **12**, 121003 (2019).

[80] U. Mishra, P. Parikh, and Yi-Feng Wu, "AlGaN/GaN HEMTs-an overview of device operation and applications", Proceedings of the IEEE **90**, 1022–1031 (2002).

[81] S. M. Sze and K. K. Ng, *Physics of semiconductor devices*, 3rd ed. (Wiley-Interscience, Hoboken, 2007), 815 pp.

[82] J. Verma, S. Islam, A. Verma, V. Protasenko, and D. Jena, "Nitride LEDs based on quantum wells and quantum dots", in *Nitride Semiconductor Light-Emitting Diodes (LEDs) Materials, Technologies, and Applications*, edited by J. J. Huang, H. C. Kuo, and S. C. Shen, 2nd ed. (Elsevier, 2018), pp. 377–413.

[83] J. H. Davies, *The physics of low-dimensional semiconductors: an introduction* (Cambridge University Press, Cambridge, 1998), 438 pp.

[84] N. Hasanov, “Quantum Dot–Incorporated Hybrid Light-Emitting Diode”, in *Quantum-dot Based Light-emitting Diodes*, edited by M. S. Ghamsari (InTech, 2017).

[85] C. Liu, B. Melanson, and J. Zhang, “AlGaN-Delta-GaN Quantum Well for DUV LEDs”, Photonics **7**, 87 (2020).

[86] M. Kane and N. Arefin, “Gallium nitride (GaN) on silicon substrates for LEDs”, in *Nitride Semiconductor Light-Emitting Diodes (LEDs) Materials, Technologies, and Applications*, edited by J. J. Huang, H. C. Kuo, and S. C. Shen, 2nd ed. (Elsevier, 2014), pp. 99–143.

[87] R. Butté and N. Grandjean, “Effects of Polarization in Optoelectronic Quantum Structures”, in *Polarization Effects in Semiconductors: From Ab InitioTheory to Device Applications*, edited by C. Wood and D. Jena (Springer US, Boston, MA, 2008), pp. 467–511.

[88] U. W. Pohl, “Introduction”, in *Epitaxy of Semiconductors: Physics and Fabrication of Heterostructures*, edited by U. W. Pohl (Springer International Publishing, Cham, 2020), pp. 1–11.

[89] T. Kuech, “Integration of Dissimilar Materials”, in *Comprehensive Semiconductor Science and Technology*, Vol. 4, edited by P. Bhattacharya, R. Fornari, and H. Kamimura (Elsevier, Amsterdam, 2011), pp. 1–24.

[90] K. Tomioka, T. Fukui, and T. Nishinga, “Growth of Semiconductor Nanocrystals”, in *Handbook of Crystal Growth Fundamentals: Transport and Stability*, Vol. IB, 2nd ed. (Elsevier, Amsterdam, 2015), pp. 749–793.

[91] L. Zhang, J. Dong, and F. Ding, “Strategies, Status, and Challenges in Wafer Scale Single Crystalline Two-Dimensional Materials Synthesis”, Chemical Reviews **121**, 6321–6372 (2021).

[92] Z. Yang, Y. Shi, J. Liu, B. Yan, R. Zhang, Y. Zheng, and K. Wang, “Optical properties of Ge/Si quantum dot superlattices”, Materials Letters **58**, 3765–3768 (2004).

[93] H. Kim, M. H. Park, S. J. Park, H.-S. Kim, J. D. Song, S.-H. Kim, H. Kim, W. J. Choi, and D.-W. Kim, “Influence of InAs quantum dots on the transport properties of GaAs-based solar cell devices”, Current Applied Physics **14**, 192–195 (2014).

[94] K. A. Lozovoy, A. G. Korotaev, A. P. Kokhanenko, V. V. Dirko, and A. V. Voitsekhovskii, “Kinetics of epitaxial formation of nanostructures by Frank–van der Merwe, Volmer–Weber and Stranski–Krastanow growth modes”, Surface and Coatings Technology **384**, 125289 (2020).

[95] O. Landré, V. Fellmann, P. Jaffrennou, C. Bougerol, H. Renevier, A. Cros, and B. Daudin, “Molecular beam epitaxy growth and optical properties of AlN nanowires”, Applied Physics Letters **96**, 061912 (2010).

[96] T. Foxon, “History of MBE”, in *Molecular beam epitaxy: materials and applications for electronics and optoelectronics*, edited by H. Asahi and Y. Horikoshi (Wiley, Hoboken, 2019), pp. 3–22.

[97] S. Franchi, “Molecular beam epitaxy: fundamentals, historical background and future prospects”, in *Molecular beam epitaxy: from research to mass production* (Elsevier, Amsterdam, 2013), pp. 1–46.

[98] U. W. Pohl, “Methods of Epitaxy”, in *Epitaxy of Semiconductors: Physics and Fabrication of Heterostructures*, 2nd ed. (Springer International Publishing, Cham, 2020), pp. 427–467.

[99] G. Koblmüller, J. Lang, E. Young, and J. Speck, “Molecular Beam Epitaxy of Nitrides for Advanced Electronic Materials”, in *Handbook of Crystal Growth: Thin Films and Epitaxy*, Vol. IIIA, edited by T. F. Kuech, 2nd ed. (North-Holland, Boston, 2015), pp. 705–754.

[100] Y. Horikoshi, “General Description of MBE”, in *Molecular Beam Epitaxy: Materials and Applications for Electronics and Optoelectronics* (2019), pp. 23–39.

[101] W. Nunn, T. K. Truttmann, and B. Jalan, “A review of molecular-beam epitaxy of wide bandgap complex oxide semiconductors”, Journal of Materials Research **36**, 4846–4864 (2021).

[102] H. Morkoç, “Growth and Growth Methods for Nitride Semiconductors”, in *Handbook of Nitride Semiconductors and Devices: Materials Properties, Physics and Growth*, Vol. 1, edited by H. Morkoç (Wiley, 2008), pp. 323–816.

[103] A. J. Ptak, “Principles of Molecular Beam Epitaxy”, in *Handbook of Crystal Growth: Thin Films and Epitaxy*, Vol. IIIA, edited by T. F. Kuech, 2nd ed. (North-Holland, Boston, 2015), pp. 161–192.

[104] M. A. Hafez, M. K. Zayed, and H. E. Elsayed-Ali, “Review: Geometric interpretation of reflection and transmission RHEED patterns”, Micron **159**, 103286 (2022).

[105] T. H. Yang, J. T. Ku, J.-R. Chang, S.-G. Shen, Y.-C. Chen, Y. Y. Wong, W. C. Chou, C.-Y. Chen, and C.-Y. Chang, “Growth of free-standing GaN layer on Si(111) substrate”, Journal of Crystal Growth **311**, 1997–2001 (2009).

[106] C. B. Duke, “Semiconductor Surface Reconstruction: The Structural Chemistry of Two-Dimensional Surface Compounds”, Chemical Reviews **96**, 1237–1260 (1996).

[107] M. D. Pashley and K. W. Haberern, “The Role of Surface Reconstructions in MBE Growth of GaAs”, in *Semiconductor Interfaces at the Sub-Nanometer Scale*, edited by H. W. M. Salemink and M. D. Pashley (Springer Netherlands, Dordrecht, 1993), pp. 63–73.

[108] S. Dasgupta, F. Wu, J. S. Speck, and U. K. Mishra, “Growth of high quality N-polar AlN(000-1) on Si(111) by plasma assisted molecular beam epitaxy”, Applied Physics Letters **94**, 151906 (2009).

[109] T. Kikuchi, A. Somintac, O. Ariyada, M. Wada, and T. Ohachi, “Role of excited nitrogen species in the growth of GaN by RF–MBE”, The third Asian Conference on Crystal Growth and Crystal Technology **292**, 221–226 (2006).

[110] G. Koblmüller, S. Fernández-Garrido, E. Calleja, and J. S. Speck, “In situ investigation of growth modes during plasma-assisted molecular beam epitaxy of (0001) GaN”, Applied Physics Letters **91**, 161904 (2007).

[111] B. Heying, R. Averbeck, L. F. Chen, E. Haus, H. Riechert, and J. S. Speck, “Control of GaN surface morphologies using plasma-assisted molecular beam epitaxy”, Journal of Applied Physics **88**, 1855–1860 (2000).

[112] C. Adelmann, J. Brault, G. Mula, B. Daudin, L. Lymperakis, and J. Neugebauer, “Gallium adsorption on (0001) GaN surfaces”, Physical Review B **67**, 165419 (2003).

[113] K. Liu, T. Tezuka, S. Sugita, Y. Watari, Y. Horikoshi, Y. Su, and S. Chang, “Modulated beam growth method for MBE grown GaN layers”, Journal of Crystal Growth **263**, 400–405 (2004).

[114] R. Aidam, P. Waltereit, L. Kirste, M. Dammann, and R. Quay, “Reproducible and uniform growth of GaN based HEMTs on 4 inch SiC by plasma assisted molecular beam epitaxy suitable for production: Reproducible and uniform growth of GaN based HEMTs on 4 inch SiC”, Physica Status Solidi (a) **207**, 1450–1454 (2010).

[115] J. Schörmann, S. Potthast, D. J. As, and K. Lischka, “*In Situ* growth regime characterization of cubic GaN using reflection high energy electron diffraction”, Applied Physics Letters **90**, 041918 (2007).

[116] M. Kakuda, S. Kuboya, and K. Onabe, “RF-MBE growth of Si doped cubic GaN and hexagonal phase incorporated c-AlGaN films on MgO(001) substrates”, Proceedings of the 16th International Conference on Molecular Beam Epitaxy (ICMBE) **323**, 91–94 (2011).

[117] D. J. Binks, P. Dawson, R. A. Oliver, and D. J. Wallis, “Cubic GaN and InGaN/GaN quantum wells”, Applied Physics Reviews **9**, 041309 (2022).

[118] L. Kubin, “Dislocations and stress relaxation in heteroepitaxial films”, in *Stress and Strain in Epitaxy: Theoretical concepts, measurements and applications*, edited by M. Hanbücken and J.-P. Deville (Elsevier, Amsterdam, 2001), pp. 99–118.

[119] X. Zhang, S. Quan, C. Ying, and Z. Li, “Theoretical investigations on the structural, lattice dynamical and thermodynamic properties of XC (X=Si, Ge, Sn)”, Solid State Communications **151**, 1545–1549 (2011).

[120] W. C. Röntgen, “Ueber eine neue Art von Strahlen”, Annalen der Physik **300**, 1–11 (1898).

[121] *The Nobel Prize in Physics 1901*, NobelPrize.org, `www.nobelprize.org/prizes/physics/1901` (visited on 01/23/2023).

[122] T. M. G. Selva, J. S. G. Selva, and R. B. Prata, "Sensing Materials: Diamond-Based Materials", in *Encyclopedia of Sensors and Biosensors* (Elsevier, 2023), pp. 45–72.

[123] M. A. Moram and M. E. Vickers, "X-ray diffraction of III-nitrides", Reports on Progress in Physics **72**, 036502 (2009).

[124] B. E. Warren, *X-ray diffraction* (Dover Publications, New York, 1990), 381 pp.

[125] W. Friedrich, P. Knipping, and M. Laue, "Interferenzerscheinungen bei Röntgenstrahlen", Annalen der Physik **346**, 971–988 (1913).

[126] M. Laue, "Eine quantitative Prüfung der Theorie für die Interferenzerscheinungen bei Röntgenstrahlen", Annalen der Physik **346**, 989–1002 (1913).

[127] *The Nobel Prize in Physics 1914*, NobelPrize.org, `www.nobelprize.org/prizes/physics/1914` (visited on 01/23/2023).

[128] C. Hammond, "X-ray diffraction: the contributions of Max von Laue, W. H. and W. L. Bragg and P. P. Ewald", in *The Basics of Crystallography and Diffraction*, edited by C. Hammond, 4th ed. (Oxford University Press, Oxford, 2015), pp. 198–209.

[129] *The Nobel Prize in Physics 1915*, NobelPrize.org, `www.nobelprize.org/prizes/physics/1915` (visited on 01/23/2023).

[130] B. D. Cullity and S. R. Stock, "Diffraction I: Geometry", in *cullityElementsXrayDiffraction2014*, edited by B. D. Cullity and S. R. Stock, 3rd ed. (Pearson Education, Harlow, 2014), pp. 91–124.

[131] C. Hammond, "The diffraction of X-rays", in *The Basics of Crystallography and Diffraction*, edited by C. Hammond, 4th ed. (Oxford University Press, Oxford, 2015), pp. 210–251.

[132] C. Hammond, "Describing lattice planes and directions in crystals: Miller indices and zone axis symbols", in *The Basics of Crystallography and Diffraction*, edited by C. Hammond, 4th ed. (Oxford University Press, Oxford, 2015), pp. 135–154.

[133] B. D. Cullity and S. R. Stock, "Properties of X-Rays", in *Elements of X-ray diffraction*, edited by B. D. Cullity and S. R. Stock, 3rd ed. (Pearson Education, Harlow, 2014), pp. 1–30.

[134] M. Sardela, "X-Ray Diffraction and Reflectivity", in *Practical Materials Characterization*, edited by M. Sardela (Springer New York, New York, NY, 2014), pp. 1–41.

[135] M. Frentrup, L. Y. Lee, S.-L. Sahonta, M. J. Kappers, F. Massabuau, P. Gupta, R. A. Oliver, C. J. Humphreys, and D. J. Wallis, "X-ray diffraction analysis of cubic zincblende III-nitrides", Journal of Physics D: Applied Physics **50**, 433002 (2017).

[136] O. Engler and V. Randle, "Macrotexture Measurements", in *Introduction to texture analysis: macrotexture, microtexture, and orientation mapping*, edited by O. Engler and V. Randle, 2nd ed. (CRC Press, Boca Raton, 2009), pp. 75–122.

[137] O. Engler and V. Randle, “Descriptors of Orientation”, in *Introduction to texture analysis: macrotexture, microtexture, and orientation mapping*, edited by O. Engler and V. Randle, 2nd ed. (CRC Press, Boca Raton, 2009), pp. 15–50.

[138] S. Santra, S. Suwas, and A. Paul, “Effect of Nb orientation and deformation on the growth of Nb $_3$ Sn intermetallic superconductor by bronze technique”, Philosophical Magazine Letters **95**, 504–510 (2015).

[139] I. Katsuhiko and K. Shintaro, “Various pole figure measurement techniques with SmartLab, assisting thin film characterization”, Rigaku Journal **34**, 10–16 (2018).

[140] B. D. Cullity and S. R. Stock, “Quantitative Phase Analysis”, in *Elements of X-ray diffraction*, edited by B. D. Cullity and S. R. Stock, 3rd ed. (Pearson Education, Harlow, 2014), pp. 359–374.

[141] R. C. Reynolds, “The Lorentz-Polarization Factor and Preferred Orientation in Oriented Clay Aggregates”, Clays and Clay Minerals **34**, 359–367 (1986).

[142] M.-X. Zhang, P. Kelly, L. Bekessy, and J. Gates, “Determination of retained austenite using an X-ray texture goniometer”, Materials Characterization **45**, 39–49 (2000).

[143] N. Herres, H. Obloh, K. Bachem, and K. Helming, “X-ray analysis of the texture of heteroepitaxial gallium nitride films”, Materials Science and Engineering: B **59**, 202–206 (1999).

[144] L. Y. Lee, M. Frentrup, M. J. Kappers, R. A. Oliver, C. J. Humphreys, and D. J. Wallis, “Effect of growth temperature and V/III-ratio on the surface morphology of MOVPE-grown cubic zincblende GaN”, Journal of Applied Physics **124**, 105302 (2018).

[145] A. Gundimeda, M. Rostami, M. Frentrup, A. Hinz, M. J. Kappers, D. J. Wallis, and R. A. Oliver, “Influence of AlxGa1-xN nucleation layers on MOVPE-grown zincblende GaN epilayers on 3C-SiC/Si(001)”, Journal of Physics D: Applied Physics **55**, 175110 (2022).

[146] T. Wade, A. Gundimeda, M. Kappers, M. Frentrup, S. Fairclough, D. Wallis, and R. Oliver, “MOVPE studies of zincblende GaN on 3C-SiC/Si(001)”, Journal of Crystal Growth, 127182 (2023).

[147] M. Benke, A. Hlavacs, F. Kristaly, M. Sepsi, and V. Mertinger, “Estimation of Phase Ratio in Bulk, Textured TWIP/TRIP Steels from Pole Figures”, Materials **14**, 4132 (2021).

[148] J. B. Kuipers, “Quaternion Algebra”, in *Quaternions and Rotation Sequences: A Primer with Applications to Orbits, Aerospace, and Virtual Reality*, edited by J. B. Kuipers (Princeton University Press, Princeton, 1999), pp. 103–140.

[149] L. Tong, M. G. Rossmann, and E. Arnold, “Patterson and molecular replacement techniques, and the use of noncrystallographic symmetry in phasing”, in *International Tables*

for Crystallography: Reciprocal space, Vol. B, 3rd ed. (International Union of Crystallography, Chester, 2010), pp. 244–281.

[150] R. Trejo-Hernández, *Github repository: Pole_figure_simulation*, github.com, `https://github.com/Rautreh/Pole_figure_simulation`.

[151] D. Nečas and P. Klapetek, "Gwyddion: an open-source software for SPM data analysis", Open Physics **10**, `10.2478/s11534-011-0096-2` (2012).

[152] A. A. Saleh, V. Q. Vu, and A. A. Gazder, "Correcting intensity loss errors in the absence of texture-free reference samples during pole figure measurement", Materials Characterization **118**, 425–430 (2016).

[153] H. Shinotsuka, S. Tanuma, C. J. Powell, and D. R. Penn, "Calculations of electron inelastic mean free paths. X. Data for 41 elemental solids over the 50 eV to 200 keV range with the relativistic full Penn algorithm: Calculations of electron inelastic mean free paths. X", Surface and Interface Analysis **47**, 871–888 (2015).

[154] W. Wisniewski, S. Saager, A. Böbenroth, and C. Rüssel, "Experimental evidence concerning the significant information depth of electron backscatter diffraction (EBSD)", Ultramicroscopy **173**, 1–9 (2017).

[155] F. Bachmann, R. Hielscher, and H. Schaeben, "Texture Analysis with MTEX – Free and Open Source Software Toolbox", Solid State Phenomena **160**, 63–68 (2010).

[156] R. Trejo-Hernández, Y. L. Casallas-Moreno, S. Gallardo-Hernández, and M. López-López, "Crystalline phase purity and twinning of Mg-doped zincblende GaN thin films", Applied Surface Science **636**, 157667 (2023).

[157] G. Nolze and R. Hielscher, "Orientations – perfectly colored", Journal of Applied Crystallography **49**, 1786–1802 (2016).

[158] U. Shmueli, "Reciprocal space in crystallography", in *International Tables for Crystallography: Reciprocal space*, Vol. B, edited by U. Shmueli, 3rd ed. (International Union of Crystallography, Chester, 2010), pp. 2–9.

[159] C. Hammond, "The reciprocal lattice", in *The Basics of Crystallography and Diffraction*, 4th ed. (Oxford University Press, Oxford, 2015), pp. 155–169.

[160] A. Kelly, "Appendix 3: Interplanar Spacings and Interplanar Angles", in *Crystallography and Crystal Defects* (2012), pp. 469–472.

Appendix A: Reciprocal space

A.1 In terms of real-lattice planes

The reciprocal lattice can be defined in multiple ways and has numerous uses [158, 159]. For instance, the reciprocal lattice provides a geometrical basis for understanding diffraction patterns from x-rays, electrons, or neutrons. There are as well multiple ways of defining the reciprocal lattice. Of special importance for this work, the reciprocal lattice can be constructed in terms of the direct lattice vectors $\boldsymbol{a}$, $\boldsymbol{b}$, and $\boldsymbol{c}$ or with the normal vectors to the lattice planes. Since the subject of this section, XRD, studies the lattice planes, the second definition is first treated here.

Consider the representation of three different families of planes in **Fig. A.1(a)** whose interplanar distances d the angles between are not conditioned, i.e., the most general case. For each family, a vector whose direction is the normal to the planes in that family is defined. The magnitude of such vectors is defined inversely proportional to the interplanar spacing, or K/d, with a proportionality constant K (usually 1). The resulting vectors from the three families of planes are shown in **Fig. A.1(b)**. These vectors are called *reciprocal vectors*, represented by $\boldsymbol{H}_{hkl}$, and, if the planes have common intersections, such as the ones in this example, their heads, or *reciprocal points* (green squares in the figure), form a *reciprocal lattice*.

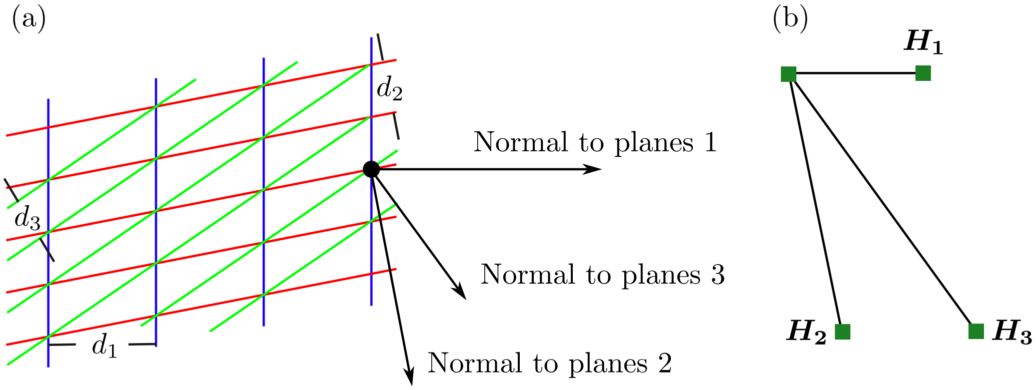

Fig. A.1. Reciprocal vector defined in terms of the lattice planes.

Furthermore, with the help of the most general case, the triclinic system in **Fig. A.2**, three basis reciprocal lattice unit cell vectors $\boldsymbol{a}^*$, $\boldsymbol{b}^*$, and $\boldsymbol{c}^*$ can be defined, equivalent to the three real lattice vectors $\boldsymbol{a}$, $\boldsymbol{b}$, and $\boldsymbol{c}$. Starting with the representation of a few real lattice planes, indicated in **Fig. A.2(a)** with miller indices (hkl), their reciprocal vectors are calculated—**Fig. A.2(b)**—so a new lattice is formed. The reciprocal lattice vectors are then defined as

$$\begin{aligned} \boldsymbol{a}^* &= \boldsymbol{H}_{100}, \\ \boldsymbol{b}^* &= \boldsymbol{H}_{010}, \\ \boldsymbol{c}^* &= \boldsymbol{H}_{001}. \end{aligned} \tag{A.1}$$

Similarly, the reciprocal angles can now be defined: α^* the angle between $\boldsymbol{b}^*$ and $\boldsymbol{c}^*$; β^* the angle between $\boldsymbol{a}^*$ and $\boldsymbol{c}^*$; and γ^* the angle between $\boldsymbol{a}^*$ and $\boldsymbol{b}^*$. In **Fig. A.2(c)** vectors $\boldsymbol{a}^*$ and $\boldsymbol{c}^*$ are schematically shown defined by the reciprocal vectors from planes (100) and (001), respectively. Vector $\boldsymbol{b}^*$ then lies outward from the page. Notice that, for example $\boldsymbol{a}^*$ is not necessarily parallel to $\boldsymbol{a}$, since, in some cases such as for the triclinic system, $\boldsymbol{a}$ is not normal to the (h00) planes. The same applies for the other two pairs of vectors.

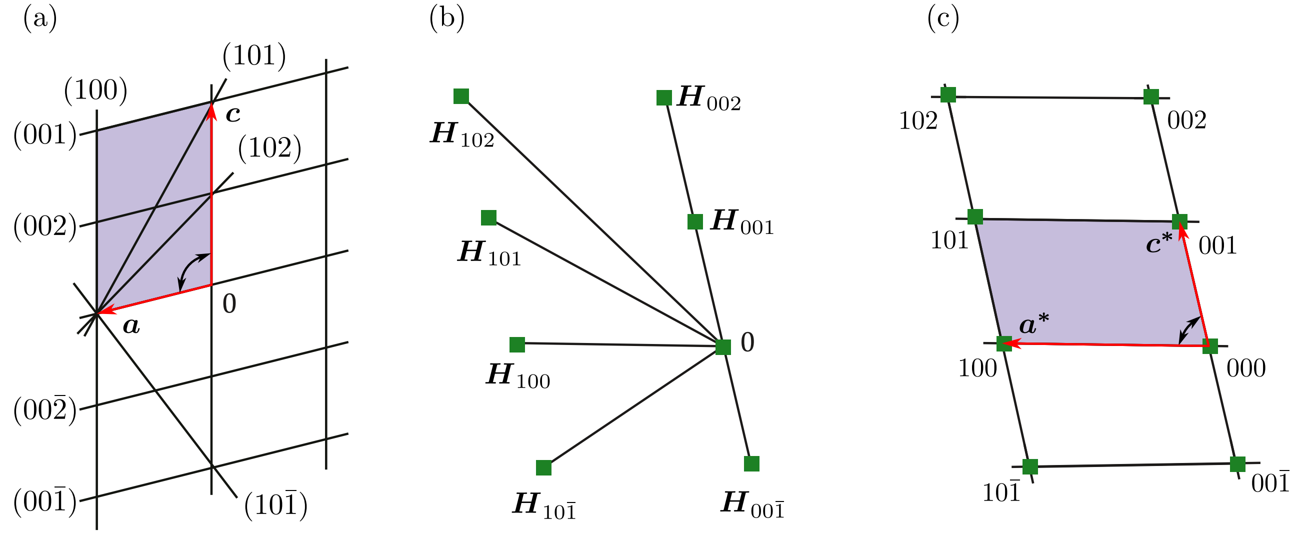

Fig. A.2. (a) real lattice of the triclinic system from where the reciprocal space (b) and (c) reciprocal-lattice vectors are defined. Indices in (a) are Miller indices while in (c) are Laue indices.

With the definitions of **Eq. (A.1)** or **Eq. (A.14)**, any reflecting plane with Laue indices hkl has a corresponding vector [160]

$$\boldsymbol{H}_{hkl} = h\boldsymbol{a}^* + k\boldsymbol{b}^* + l\boldsymbol{c}^*, \tag{A.2}$$

whose direction is normal to the planes and magnitude

$$|\boldsymbol{H}_{hkl}|^2 = \boldsymbol{H}_{hkl} \cdot \boldsymbol{H}_{hkl} = H_{hkl} = \left(\frac{1}{d_{hkl}}\right)^2 \tag{A.3}$$

with proportionality constant $K = 1$. Expanding the dot product

$$\left(\frac{1}{d_{hkl}}\right)^2 = (ha^*)^2 + (kb^*)^2 + (lc^*)^2 + 2klb^*c^*\cos\alpha^* + 2hla^*c^*\cos\beta^* + 2hka^*b^*\cos\gamma^*. \tag{A.4}$$

The vector described by **Eq. (A.2)** entails the two most important features of a lattice plane, i.e., orientation and interplanar distance, and is one of the most important equations for the interpretation of XRD results. If the reciprocal-lattice vectors are defined terms of an orthonormal basis $\hat{\boldsymbol{x}}$, $\hat{\boldsymbol{y}}$, and $\hat{\boldsymbol{z}}$ (e.g. $\boldsymbol{a^*} = a^*_x\hat{\boldsymbol{x}} + a^*_y\hat{\boldsymbol{y}} + a^*_z\hat{\boldsymbol{z}}$), **Eq. (A.2)** can be expanded to

$$\boldsymbol{H}_{hkl} = (ha^*_x + kb^*_x + lc^*_x)\,\hat{\boldsymbol{x}} + \left(ha^*_y + kb^*_y + lc^*_y\right)\hat{\boldsymbol{y}} + (ha^*_z + kb^*_z + lc^*_z)\,\hat{\boldsymbol{z}}, \tag{A.5}$$

which can be rewritten in matrix form for computational purposes

$$\boldsymbol{H}_{hkl} = \begin{bmatrix} h & k & l \end{bmatrix} \begin{bmatrix} a^*_x & a^*_y & a^*_z \\ b^*_x & b^*_y & b^*_z \\ c^*_x & c^*_y & c^*_z \end{bmatrix} \begin{bmatrix} \hat{\boldsymbol{x}} \\ \hat{\boldsymbol{y}} \\ \hat{\boldsymbol{z}} \end{bmatrix}. \tag{A.6}$$

A.2 In terms of real-lattice vectors

As mentioned at the beginning of this section, the reciprocal basis vectors can also be defined in terms of the real lattice vectors. For this, some important relations between the reciprocal and real basis vectors need to be derived first.

Fig. A.3 depicts the unit cell of the triclinic system with vectors $\boldsymbol{b}$ and $\boldsymbol{b^*}$ out from the page (not necessarily parallel). Let ϕ be the angle between $\boldsymbol{a}$ and $\boldsymbol{a^*}$, then

$$\boldsymbol{a^*} \cdot \boldsymbol{a} = |\boldsymbol{a^*}||\boldsymbol{a}|\cos\phi = a^*a\cos\phi. \tag{A.7}$$

With the definition of **Eq. (A.1)** and $d_{100} = a\cos\phi$ (from the figure),

$$\boldsymbol{a^*} \cdot \boldsymbol{a} = \frac{1}{d_{100}}d_{100} = 1 \tag{A.8}$$

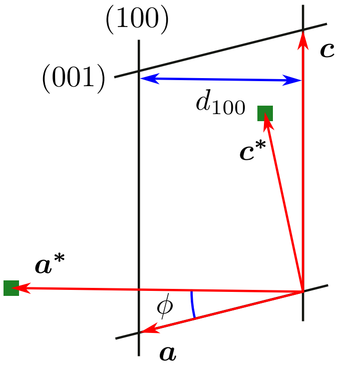

Fig. A.3. Geometrical relations between real- and reciprocal-lattice vectors in the triclinic unit cell.

and, since $\boldsymbol{a}^*$ is perpendicular to the (100) planes $\boldsymbol{b}$ and $\boldsymbol{c}$ lie on the (100) plane passing through the origin,

$$\boldsymbol{a}^* \cdot \boldsymbol{b} = \boldsymbol{a}^* \cdot \boldsymbol{c} = 0. \tag{A.9}$$

A similar analysis can be made for $\boldsymbol{b}^*$ and $\boldsymbol{c}^*$, so that

$$\boldsymbol{a}^* \cdot \boldsymbol{a} = \boldsymbol{b}^* \cdot \boldsymbol{b} = \boldsymbol{c}^* \cdot \boldsymbol{c} = 1 \tag{A.10}$$

and

$$\boldsymbol{a}^* \cdot \boldsymbol{b} = \boldsymbol{a}^* \cdot \boldsymbol{c} = \boldsymbol{b}^* \cdot \boldsymbol{a} = \boldsymbol{b}^* \cdot \boldsymbol{c} = \boldsymbol{c}^* \cdot \boldsymbol{a} = \boldsymbol{c}^* \cdot \boldsymbol{b} = 0. \tag{A.11}$$

With **Eq. (A.11)**, one can conclude that $\boldsymbol{a}^*$ is proportional to the cross product of $\boldsymbol{b}$ and $\boldsymbol{c}$

$$\boldsymbol{a}^* = U(\boldsymbol{b} \times \boldsymbol{c}). \tag{A.12}$$

Taking into account that $\boldsymbol{a}^* \cdot \boldsymbol{a} = 1$ from **Eq. (A.10)**, the proportionality constant must be $U = 1/[\boldsymbol{a} \cdot (\boldsymbol{b} \times \boldsymbol{c})]$. If $\boldsymbol{a}$, $\boldsymbol{b}$, and $\boldsymbol{c}$ are a right-handed set, then the mixed product $\boldsymbol{a} \cdot (\boldsymbol{b} \times \boldsymbol{c})$ represents the volume of the unit cell V. Taking the real-lattice vectors' components in a Cartesian system (e.g. $\boldsymbol{a} = a_x\hat{\boldsymbol{x}} + a_y\hat{\boldsymbol{y}} + a_z\hat{\boldsymbol{z}}$), the volume can be obtained through the determinant

$$V = \begin{vmatrix} a_x & a_y & a_z \\ b_x & b_y & b_z \\ c_x & c_y & c_z \end{vmatrix}. \tag{A.13}$$

With that, and using the same considerations for $\boldsymbol{b}^*$ and $\boldsymbol{c}^*$ as in **Eq. (A.12)**, the three reciprocal basis vectors are defined

$$\begin{aligned}\boldsymbol{a}^* &= \frac{\boldsymbol{b}\times\boldsymbol{c}}{V},\\ \boldsymbol{b}^* &= \frac{\boldsymbol{c}\times\boldsymbol{a}}{V},\\ \boldsymbol{c}^* &= \frac{\boldsymbol{a}\times\boldsymbol{b}}{V},\end{aligned} \tag{A.14}$$

whose magnitudes

$$\begin{aligned}a^* &= \frac{bc\sin\alpha}{V},\\ b^* &= \frac{ca\sin\beta}{V},\\ c^* &= \frac{ab\sin\gamma}{V}.\end{aligned} \tag{A.15}$$

Similarly, for the reciprocal angles

$$\begin{aligned}\cos\alpha^* &= \frac{\cos\beta\cos\gamma-\cos\alpha}{\sin\beta\sin\gamma},\\ \cos\beta^* &= \frac{\cos\gamma\cos\alpha-\cos\beta}{\sin\gamma\sin\alpha},\\ \cos\gamma^* &= \frac{\cos\alpha\cos\beta-\cos\gamma}{\sin\alpha\sin\beta}.\end{aligned} \tag{A.16}$$

Appendix B: Derived work and collaborations

B.1 Published journal articles

H. I. Solís-Cisneros, H. Vilchis, R. Trejo-Hernández, A. L. Melchor-Tovilla, A. Guillén-Cervantes, and C. A. Hernandez-Gutierrez, "Study and characterization of the nanotextured Ga2O3-GaOOH formations synthesized via thermal oxidation of GaAs in ambient air", Semicond. Sci. Technol., Aug. 2023, doi: 10.1088/1361-6641/acf2be.

R. Trejo-Hernández, Y. L. Casallas-Moreno, S. Gallardo-Hernández, and M. López-López, "Crystalline phase purity and twinning of Mg-doped zincblende GaN thin films", Applied Surface Science, vol. 636, p. 157667, Nov. 2023, doi: 10.1016/j.apsusc.2023.157667.

H. Solís-Cisneros, C.A. Hernández-Gutiérrez, A.-R. Anwar, P.Y. Sevilla-Camacho, J.L. Camas-Anzueto, R. Grajales-Coutiño, R. Trejo-Hernández, Y.L. Casallas-Moreno, M. López-López, "Physical and technological analysis of the AlGaN-based UVC-LED: an extended discussion focused on cubic phase as an alternative for surface disinfection", Rev. Mex. Fís., vol. 68, no. 2 Mar-Apr, Feb. 2022, doi: 10.31349/RevMexFis.68.020301.

B.2 Submitted journal articles

José de Jesús Cruz Bueno, Manolo Ramirez López, Daniel Flores Ramirez, Gerardo Villa Martinez, Raul Trejo Hernández, Luis Reséndiz Mendoza, Patricia Rodríguez Fragoso, Yenny Lucero Casallas Moreno, "Physical mechanism of Zn and Te doping process of $In_{0.145}Ga_{0.855}$ $As_{0.108}Sb_{0.892}$ quaternary alloys", submitted to the Journal of Alloys and Compounds"

B.3 Journal articles being written

Raúl Trejo-Hernández, Yenny-Lucero Casallas-Moreno, Máximo López-López, "A software for Pole-Figure simulation and Analysis"

Raúl Trejo-Hernández, Yenny-Lucero Casallas-Moreno, Mario-Alberto Zambrano-Serrano, Salvador Gallardo-Hernández, Máximo López-López, "Effect of Nucleation Temperature on Crystalline Purity of PAMBE-grown Zincblende GaN/GaAs Structures”

Ángel Leonardo Martínez López, José de Jesús Cruz Bueno, Raúl Trejo Hernández, Andrés de Luna Bugallo, Yenny Lucero Casallas Moreno, Julio Gregorio Mendoza Álvarez, ”Growth Mechanism of GaAs on Greohene Deposited by CSVT”

B.4 International conferences

Raúl Trejo-Hernández, Yenny-Lucero Casallas-Moreno, Salvador Gallardo-Hernández, Máximo López-López, “Analysis of Twinning in Zincblende GaN Thin Films Grown on GaAs By plasma-assisted MBE”, XV International Conference on Surfaces, Materials and Vacuum, Sep. 2023.

Angel Leonardo Martinez-Lopez, Raul Trejo-Hernandez, Jesus Fernando Fabian-Jocobi, Marlene Camacho-Reynoso, Patricia Rodriguez-Fragoso, Maximo Lopez-Lopez, Julio Gregorio Mendoza-Alvarez, “Quasi-Van der Waals Epitaxy of Aluminum Arsenide (AlAs) on Graphene/-GaAs Substrates: Temperature-Dependent Morphology”, XV International Conference on Surfaces, Materials and Vacuum, Sep. 2023.

M.A. Ramírez-Orozco, A. L. Martínez-López, R. Trejo-Hernández, L. I. Olvera-Cano, A. Cruz-Orea, P. Rodríguez-Fragoso, J. G. Mendoza-Álvarez, M. López-López, Y. L. Casallas-Moreno, “Thermal, Structural, and Optical Characterization of GaAs Surface Passivation”, XV International Conference on Surfaces, Materials and Vacuum, Sep. 2023.

Jesús Fernando Fabian Jocobi, Raúl Trejo Hernández, Ángel Leonardo Martínez López, Yenny Lucero Casallas Moreno, Iouri Koudriavysev, Daniel Olguin Melo, Salvador Gallardo Hernaández, Máximo López López, “Surfactant Effect of Mn on AlN MBE Growth”, 37th North American Conference on Molecular Beam Epiaxy, Sep. 2023.

Raúl Trejo Hernández, Yenny Lucero Casallas Moreno, Salvador Gallardo Hernández, Máximo López López, ”Crystalline phase purity of zincblende GaN by X-ray diffraction pole figures”, RD20 Summer School, Jul. 2023.

Jesús Fernando Fabian-Jocobi, Raúl Trejo Hernández, Jorge Iván Hernández Martínez, Angel Leonardo Martínez López, Yenny Lucero Casallas Moreno, Salvador Gallardo Hernández, Daniel Olguín Melo, Máximo López López, ”Incorporation of Mn into w-AlN nanostructures by MBE”, XXIV Latin American Symposium of Solid State Physics, Nov. 2022.

Raúl Trejo Hernández, Mario Alberto Zambrano Serrano, Marlene Camacho Reynoso, Marcos Macias Mier, Salvador Gallardo Hernández, Yenny Lucero Casallas Moreno, Máximo López López, ”Quantification of wz-inclusions in zb-GaN grown by PAMBE on GaAs by x-ray pole figures", XV International Conference on Surfaces, Materials and Vacuum, Sep. 2022.

Jorge Iván Hernández Martínez, Raúl Trejo Hernández, Yenny Lucero Casallas Moreno, Salvador Gallardo Hernández, Máximo López López, "Growth of InGaN and InAlN nanostructures on Si(111) substrates, XV International Conference on Surfaces, Materials and Vacuum, Sep. 2022.

H. Solis-Cisneros, C. A. Hernández-Gutiérrez, J.L. Camas-Anzueto, R. Grajales-Coutiño, R. Trejo-Hernández, Y. L. Casallas-Moreno, M. López-López, "Alternative for ultraviolet disinfection. Cubic and hexagonal AlGaN-based UVC-LED challenges", 21st International Conference on Molecular Beam Epitaxy, Sep. 2020.